EXPERIMENTAL STUDIES OF FUNDAMENTAL ASPECTS OF AUGER EMISSION PROCESS IN Cu(100) AND Ag(100)

by

PRASAD VIVEK JOGLEKAR

Presented to the Faculty of the Graduate School of
The University of Texas at Arlington in Partial Fulfillment
of the Requirements
for the Degree of

DOCTOR OF PHILOSOPHY

THE UNIVERSITY OF TEXAS AT ARLINGTON
August 2014

Acknowledgements

I would like to extend my gratitude to all those who were part of my PhD journey. First and foremost I would like to thank Dr Alex Weiss, my dissertation supervisor, for mentoring me in this research. He has introduced me to the study of surface science, PAES, APECS and materials analysis. I am fortunate to have Dr Steven Hulbert as my co advisor. Their knowledge, enthusiasm, passion for science and encouragement to us was exemplary. Despite both being swamped by administrative work and responsibilities, we managed to have good discussions (and meetings over Skype). Both are different personalities and have different styles of working. It was a good experience working with these two inspiring people. I admire them and wish to become like them.

I further extend my thanks to my dissertation committee, Dr. Koymen, Dr. Lopez, Dr Zhang, Dr.Sharma, Dr Ngai, and (Late) Dr Fazleev, their valuable suggestions helped my understanding of the research work and gave me food for thought to think along different directions.

The learning experiences in the lab and the research work I have done was made enjoyable solely due to my lab mates. Their motivation, cheerfulness and jolly nature was helpful in the stressful times. It was fun going to conferences and preparing presentation with them. I sincerely thank Sushant Kalaskar, Suman Satyal and Karthik Shastry along with L Lim, Z Lim, Thomas Bates, Codey Mishler, and Randall Gladen. I also thank Mr Q Dong at BNL for his technical help at beamline U1A and helping with data acquisition. I thank Valay Shah, for introducing me to MATLAB and helping me to write code for my data extraction.

My foundations of physics were reinstated by the graduate physics courses I took and discussions with the Physics Dept professors, especially Prof Z Musielak, Prof Fry, (Late) Prof Ray, Prof Liu. I was fortunate to have my batch mates, Kapil, Shree, Billy, Smita and Harsha. Studying was fun with you guys. I further thank the Physics Department graduate students- friends for their support and encouragement during my research (special mention: Ian, Kunal Tiwari, Rakesh, Kinjal, Pranab). I also take this opportunity to thank the Physics office staff for their help in our appointments and other administrative work. Thanks to-Margie, Stacey, Bethany, Angel, and Brian. For technical help many thanks to Dough Coyne, Victor Reece.

My special thanks to Dr Nilakshi Veerbhatina who encouraged me to get involved on campus and in cultural activities. The activities and friends-people associated with Indian Cultural Council (ICC/HSC) (2009-2014) added ‘life’ in my research life (there are so many people I could not mention all of them due to space limitations).

While working in Indian Institute of Technology Bombay (IITB), I was encouraged by faculty and staff of Physics, Mat Sci., EE, SAIF, for pursuing higher studies. I thank my friends and family at IITB very much.

I could not have imagined my stay at UTA without these guys, many thanks to Subhash, Rachit, Swanand, Saket, Tejas, Chetan, Piyush, Amit, Prashant, Akash, Darshan, Sapan, Kirti, Krishna, Soumyava, Megha, Mrunamayi, Vallari, Shantanu, Pooja, Amruta, Neha, Shalini, Vidula ,Swathi N, Santosh, Manjeera. Appu, Prudhvi, Nitesh, Shruthi, Radha and Swathi R. I extend my special thanks to Megha Rao, Amruta, Atulya, Neethu, and Veena for proofreading my dissertation.

I also would like to thank Shri Vishvesh Joshi and Agte family for encouraging me to apply abroad for further studies and supporting me in everything I do. Finally I express my deep gratitude to my parents Mr Vivek J Joglekar, Mrs Kumud Joglekar and to my younger brother Mr Ashish Joglekar, for their faith in me, and their encouragement, unconditional love and support.

June 26, 2014

Abstract

EXPERIMENTAL STUDIES OF FUNDAMENTAL ASPECTS OF AUGER EMISSION PROCESS IN Cu(100) AND Ag(100)

Prasad Vivek Joglekar, PhD

The University of Texas at Arlington, 2014

Supervising Professor: Alexander Herman Weiss

Auger spectra at low energies are accompanied by large contributions unrelated to the Auger transition. The Auger unrelated contributions can obscure the Auger peak and affect the quantitative analysis of the materials under investigation. In this dissertation we present a methodology to measure experimentally the Auger unrelated contributions and eliminate it from the Auger spectrum for obtaining an Auger spectrum inherent to the Auger transition. We used Auger Photoelectron Coincidence Spectroscopy (APECS) to obtain the Auger spectrum. APECS measures the Auger spectrum in coincidence with the core energy level and thus discriminating the contributions arising from secondary electrons and electrons arising from the non-Auger transition. Although APECS removes most of the Auger unrelated contributions, it cannot distinguish the contribution which is measured in coincidence with the inelastically scattered valence band electrons emitted at the core energy. To measure this inelastically scattered valence band contribution we did a series of measurements on Ag(100) to study NVV Auger spectrum in coincidence with 4p energy level and Cu(100) to study MVV Auger spectrum in coincidence with 3p energy level. The coincidence detection of the core and Auger-valence electrons was achieved by the two cylindrical

mirror analyzers (CMAs). One CMA was fixed over a range of energies in between VB and core energy level while other CMA scanned corresponding low energy electrons from 0 to70eV. The spectrums measured were fit to a parameterized function which was extrapolated to get an estimate of inelastically scattered valence band electrons. The estimated contribution was subtracted for the Ag and Cu APECS spectrum to obtain a spectrum solely due to Auger transition with inelastically scattered Auger electron and multi Auger decay contributions associated with the transition. In the latter part of this dissertation, we propose a theoretical model based on the spectral intensity contributions arising from elastically scattered electrons from the atomic layers and relate it with the data obtained from our experiments to estimate the Auger related contribution.

Table of Contents

List of Illustrations

List of Tables

Chapter 1

Introduction

1.1 Overview

In recent years the study and understanding of surfaces has gained a lot of attention and importance due to its industrial applications such as in electronics, nanotechnology and energy related fields. To cite a few examples, in a solar cell device the energy conversion happens at the surface, in a fuel cell- catalytic reaction, the catalyst reacts at its surface and enhances the chemical reaction. Hence knowing the surface and energy sharing by the electrons at the surface can help us engineer materials for industrial as well as domestic applications.

Electron spectroscopies are important tool for the study of surfaces. We studied Copper and Silver surfaces using a spectroscopic technique known as Auger photoelectron coincidence spectroscopy (APECS). In this technique, a photon beam is incident on a sample surface knocking out inner shell electrons of surface atoms; these electrons are termed as photoelectrons. The creation of a photoelectron causes a vacancy in the inner shell thereby leaving the atom in an excited state. This excited atom relaxes by filling the inner shell vacancy with electrons in the valence (outer) shell, this result in a vacancy and excess energy in the outer shell. The excess energy is then transferred to the neighboring valence electrons, knocking them out of the atom. These outgoing electrons are known as Auger electrons and this mechanism when the valence electron drops down to fill the inner shell vacancy is called Auger transition. The sample surface properties and behavior can be understood by detecting the Auger electrons (and spectrum). In APECS, the Auger electrons were detected in coincidence with the causal core photoelectron by two detectors, cylindrical mirror analyzers (CMAs), giving us the

APECS spectrum. This spectrum is important in qualitative and quantitative analysis of the sample surface.

This dissertation presents our work where we studied the fundamental aspects of the electrons emitted due to filling of the core hole. These Auger (transition) related electrons along with Auger unrelated electrons contributes to the Auger spectrum. The Auger unrelated electrons are the electrons emitted due to scattering of the photoelectrons with the electrons at energy levels other than the core. Our experimental measurements were the first of their kind to measure the spectral intensity contribution coming from the Auger unrelated electrons and the only one to attempt to remove all of the secondary electron background. The experimental measured contribution was subtracted from the APECS spectrum to obtain a spectrum solely related to the Auger.

To further improve our understanding of the physics behind the spectral intensity at the low energies part of the spectrum we did some theoretical calculations to model the electron intensity arising from the top layers of a solid. We modeled the intensity ratio of the elastically scattered electrons with the inelastically scattered electrons coming from top atomic layers. This ratio was compared with our experiments.

1.2 Motivation

The motivation behind the proposed experiments were the earlier APECS studies done on Aluminum Al(100) single crystal by Jensen et al, where they had measured the Auger spectrum down till 40eV [1] (Fig 1). Their studies predicted the increase in spectral intensity at the lower energy side of the spectrum; this was experimentally confirmed by Shastry et al., by measuring the Auger spectrum of Copper Cu (100) and Silver Ag (100) down till 0ev.

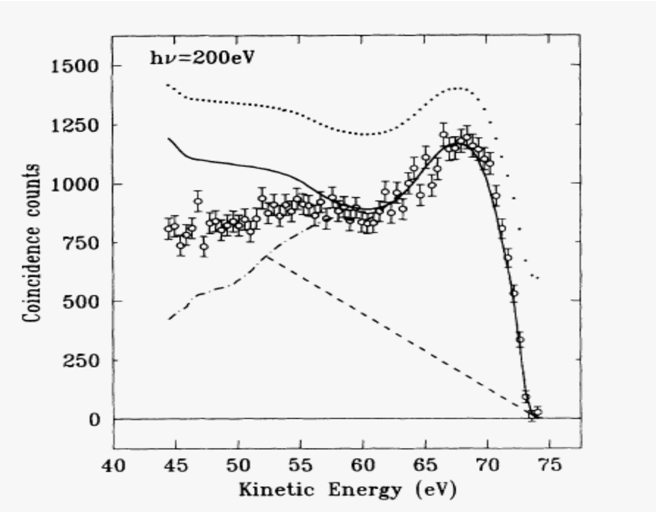

Figure 1-1 Al APECS spectrum till 40eV from Jensen et al [1]

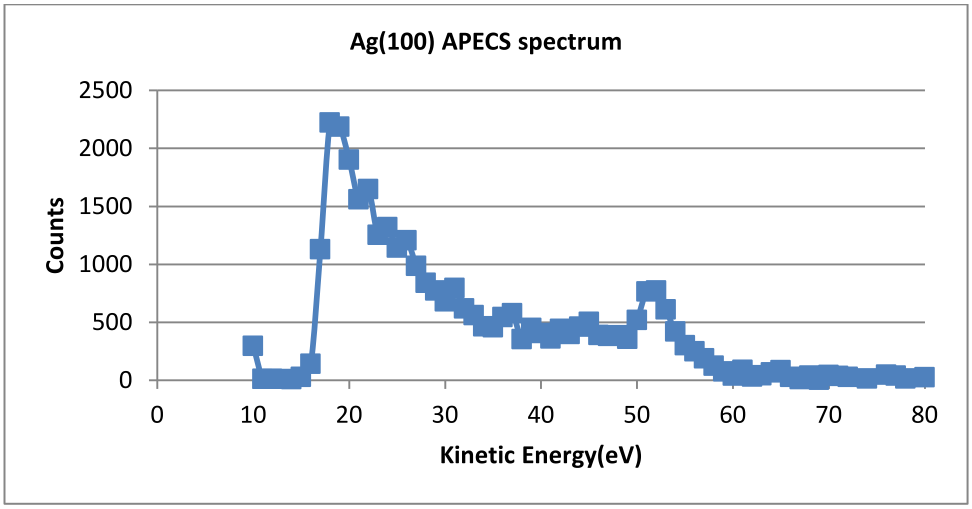

Figure 1-2 Ag(100) APECS spectrum

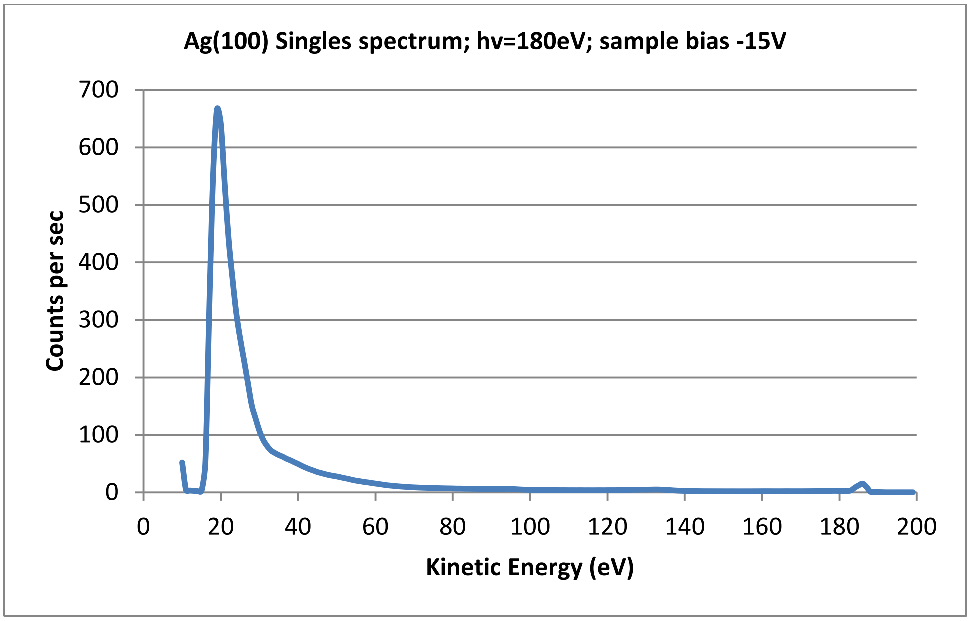

Figure 1-3 Photoelectron spectrum of Ag(100)

The low energy part of the spectrum that is the region below the auger peak down till 0eV is called low energy tail (LET); it contains a major portion of the spectral weight. We want to understand why the intensity is higher at the low energies and what all contributes to the low energy part of the spectrum. Is the low energy tail intrinsic to the Auger process is to be answered? To understand the physics behind the fundamental aspects of Auger transition contributing to the low energy tail motivated us to perform series of APECS experiments [2].

1.3 Introduction

The information of the surface regarding the local density of the states, chemical bonding, atomic charge, post collision interactions, charge transfer effects have been widely studied by the popular techniques of Auger electron spectroscopy and X-ray photoelectron spectroscopy. The spectral analysis of AES/XPS spectrum often is complicated due to the high spectral intensity at the low energy part of the spectrum obscuring important peaks under it. There have been many numerical, semi empirical techniques to subtract off the background from the spectrum but there have not been any experimental measurements in metals. We used a coincidence technique which is capable of extracting data by ignoring the large background for our experimental determination of the extrinsic background contribution. The coincidence technique can also be used to study the correlation energy, correlation effects, various pairs of excitation events such as photoelectron- Auger electron, electron- electron, electron- ion pair, and photo electron- fluorescence pair and can be used to study material's electronic properties. We studied the photoelectron and Auger electron coincidence using Auger Photoelectron coincidence spectroscopy (APECS).

The first Auger photoelectron coincidence spectroscopy (APECS) experiments were done by Haak, Sawatzky and Thomas in 1978 [3]. They developed this technique using a conventional x-ray source. Initial core level coincidence spectroscopy measurement used conventional x-ray sources; these sources were good for a high incident flux in the hard x-ray (2-100KeV) region but were less efficient in the soft x-ray region (0.5-2keV). The technological advancements in the synchrotron radiation sources provided a good (high flux) alternative for conventional sources in VUV-soft x- ray region and the high flux beam obtained from the synchrotron radiation reduces the data acquisition time as well as improving the signal to noise ratio of the spectrometer. The APECS technique was later adapted by Jensen et al on the vacuum ultra violet (VUV) storage ring at the national synchrotron light source (NSLS), Brookhaven national lab. Also, Bartynski et al, [4] continued and performed a number of experiments to reduce core level lifetime broadening in photoemission, isolate individual sites in a solid and probe their local electronic structure, distinguish between Auger related and unrelated secondary electron emission, explore correlated photo-excitation/Auger relaxation events, separate overlapping spectral features, probe electronic structure with improved depth resolution and eliminate uncorrelated secondary background.

In APECS, a core photoelectron and its associated Auger electron are detected in time coincidence with each other. Since both of these electrons originate from the same photo excitation event, APECS has the unique capability of probing the local electronic structure. Haak [3] successfully distinguished features in the L3VV Auger line originating either from the ionization of the 2p1/2 or the 2p3/2 shells in Cu. The APECS technique has always been helpful in discovering the new material properties, displaying unexpected physical phenomena, or exhibiting both [5, and references there in]. The APECS technique has also been used to study the Auger emission line shapes in alloy systems such as Ni/Fe [6]. Although the coincidence count rate is much lower from an alloy compared to a pure element, Thurgate [6] was successful in showing a possible shake up, shake off in the final state with some high probability.

1.4 Direct Auger Transition

When a photon beam of energy hv is incident on the sample, it knocks out a photoelectron from a core level. The core photoelectron comes out of the sample in continuum with a core binding energy (E_c), creating a vacancy at the core. The core binding energy is less than the incident photon beam energy hv. The core vacancy excites the atom and it relaxes by the electron in the valence band with a higher energy than core jumping down and filling the core. As the core vacancy is filled by the valence electron, the excess energy of the valence electron is transferred to the neighboring valence electrons, resulting in their emission from the sample. The electron coming out is known as Auger electron and this type of transition is known as Auger transition. Auger transition involves core and valence shells of the atom. Hence it’s also called as CVV transition, initial core level and final valence level. The Auger electron comes out with energy difference of core, valence band and the work function of the analyzer.

$$E_{Auger}= E_c-E_{v1}-E_{v2}-\phi_A , \qquad (1.1)$$

The above equation also takes in to account work function of the analyzer, as the analyzer is made up of metal and thus for electron to be detected must have energy greater than the difference of work function of sample (ϕ_S) and analyzer (ϕ_A) to reach the analyzer.

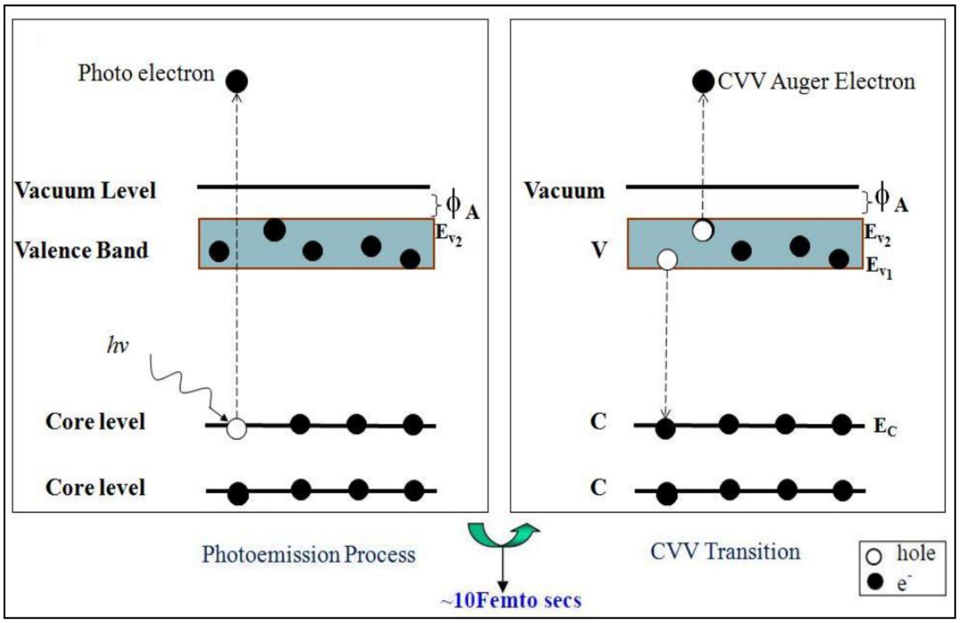

Figure 1-4 Direct Auger transition

The figure 1.4 describes the direct Auger transition where the final state has two holes in the valence band. The Auger transition is predominant when the core binding energy is less than 2KeV. For binding energy higher than 2KeV, X-ray emission is observed.

When a photon beam is incident on the sample it generates photoelectrons, Auger electrons, and secondary electrons. The secondary electrons consist of all the electrons which are not a result of primary process and contain inelastically scattered photoelectrons, inelastically scattered Auger electrons, inelastically valence band electrons, etc. A photoelectron spectrum is shown in the figure below:

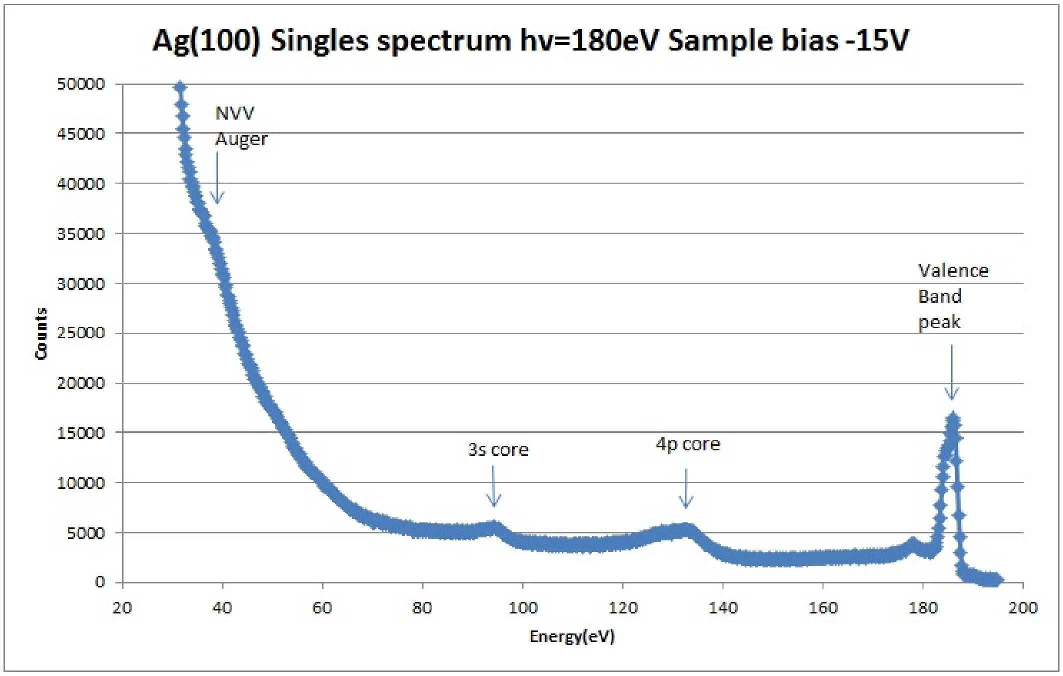

Figure 1-5 Ag(100) Photoelectron spectrum

The above photoelectron spectrum shows Core, Auger and valence band peaks; here we have assumed the work function of the sample is greater than that of the analyzer. The maximum energy of the electrons entering the analyzer will be hv-ɸA and the minimum energy can be of the electrons having energy ɸS-ɸA. The end of valence band peak is the Fermi level of the atom (as Fermi level is filled in the energies below).

The maximum KE of the Auger to be detected is the electron coming from the top of the valence band.

$$KE_{Auger}(Max) = E_c - \phi_{A,} \qquad (1.2)$$

Where Ec is the binding energy of the core referenced to top of the valence band.

If the electron comes from the bottom of the valence band, letting the width of the valence band be W, then the minimum kinetic energy of the Auger electrons will be

$$KE_{Auger}(Min)= E_c-2W-\phi_{A,} \qquad (1.3)$$

The width (full width at half maximum) of the CVV Auger transition will reflect twice the width of the valence band

$$KE_{Auger}(Max)- KE_{Auger}(Min)= E_c-\phi_A - E_c-2W-\phi_A = 2W, \qquad (1.4)$$

In the above relation we have not included the hole-hole correlation energy (U). When the width is larger than the correlation energy, we can assume U~0. The theoretical models and estimates for the CVV Auger peaks (line shapes) are often based on this assumption and are the self-convolution of density of the states for two holes in the final states. When there are more than two hole final states the Auger spectra is complicated and depending on the shell of the atom is excited and the final state of the transition can end up with 3 or multiple holes. This gives us the opportunity to study the valence levels near core holes [7-10].

1.5 Auger Related and Unrelated Contributions

The Auger transition (CVV) is a complex process and there are various other transitions that can occur along with it for example Coster Kronig C_1C_2V or multi Auger decay (CVVV). These transitions contribute to the intensities (especially low energy part) of the spectrum. The contributions also affect the Auger peak shape, intensity and cause a shift in the energy. The contributions can be classified as Auger related contributions and Auger unrelated contributions. The Auger related contributions are related to the filling of the core hole and the Auger unrelated contributions take into account contributions arising from scattering of the photoelectrons [11, 12].

1.5.1 Auger Related Contributions

1.5.1.1 Initial States Shake Up and Shake Off

When a photon is incident on the sample, it leaves the atom in an excited state. In the shakeup process no electron is emitted from the sample although the atom is in the excited state, the electron in the ground states are shaken up in the higher energy states. The shakeup processes can cause well defined peaks in the spectrum. In the shake off process the electron besides the emitted photoelectron is shaken off and emitted out of the sample into the energy continuum. The shake off processes can cause ill-defined broad peaks in the spectrum.

1.5.1.2 Final States Shake Up and Shake Off

At times when the Auger electron leaves the sample instead of the atom relaxing to the ground state and it remains in the excited state, this causes the electrons in the solid to shake up in the energy levels or its shaken off in the energy continuum leaving additional vacancy in atom.

1.5.1.3 Coster-Kronig Transitions

These are special kind of Auger transitions where the deeper core (C1) hole caused by the incident beam is filled by a shallow core (C2) which is then filled by a valence band electron, emitting an Auger electron out of the sample. This is a C1C2V (CCV) transition instead of CVV as in the Auger transition. These transitions are prominent in transition metals as well as heavier atoms and occur when the difference in the binding energy of the deeper and shallow core electrons is greater than the binding energy of the valence band electron. As there is an overlap of the two orbitals the transition probabilities are high.

1.5.1.4 Auger Cascade

A cascade of electrons from the valence band are emitted out when electrons from higher energy level fill up a core hole which is created deeper (energy level) in the solid. When this process occurs via Auger transition, additional holes at the core are created. These holes stay constant and act as spectators in the transition and affect (reduce) the Auger electrons energy due to the electrons and holes correlation. These electrons contribute to the low energy part of the spectrum.

1.5.1.5 Intrinsic Plasmons

When electrons at the surface or in the bulk get some energy (less than their binding energy), they oscillate. The collective oscillation of electrons at the surface is called surface plasmon and when in bulk is known as bulk plasmon. Both types of plasmons have well defined energy. Plasmons get created when a core hole is formed or when the photoelectron or the Auger electrons leave the atom/solid. When the electrons leave the atom, the atom is ionized and the overall charge of the system gets affected. If plasmons are formed as a result of as a result of the change in the atomic charge then it's defined as an intrinsic plasmon. The plasmon peaks are typically lower in energy than the Auger peaks.

1.5.1.6 Plasmon Gain Peaks

These are also known as shake down peaks and they end up at the higher energy side of the Auger peak. The two step model does not predict the Plasmon gain peaks. When a core hole state creates intrinsic Plasmon, and if this Plasmon is localized near the Auger transition, then the outgoing Auger electron gains the energy from the localized Plasmon and ends up at a higher kinetic energy in the spectrum. The Plasmon gain peak are causal of the time overlap of relaxation of intrinsic Plasmon (electron gas) caused due to core hole creation and the Auger transition.

1.5.2 Auger Unrelated Contributions

1.5.2.1 Extrinsic Plasmons

These processes are the side-effects of the Auger transitions but contribute to the spectrum. When the core photoelectron or energetic Auger electrons while leaving the solid interact with electron gas they can induce surface and bulk plasmons thus giving rise to peaks at low kinetic energy. The plasmons can also be created due to the incident photon beam.

1.5.2.2 Electron Hole Production

An electron hole pair is created when an energetic electron moves out of the solid. The energetic electrons, while traversing out of the solid, can create additional vacancies resulting in an electron hole pair. This causes a smooth contribution in the low energy side of the spectrum.

1.5.2.3 Core Hole Excitations

As the core photoelectron travels out of the solid it may excite other core electrons which can end up contributing to the intensity in the low energy side of the spectrum.

1.5.2.4 Inelastically Scattered Valence Band, Core and the Auger Electrons

The inelastically scattered valence band can have energies from the valance band down to zero eV. Similarly, Core and Auger electrons, when scattered inelastically, can end up in the low energy part of the spectrum. As the electrons are fermions they are indistinguishable, making it challenging to measure the individual contributions experimentally. Besides the above mentioned electron loss contributions, other factors that affect the CVV Auger spectrum are Auger matrix element effects, Initial Core hole screening, Final-state hole-hole interaction, non orthogonality effects, and effective collective excitations.

1.6 Inelastic Scattering of the Valence Band Photoelectrons

An atom is ionized as the electrons are excited and knocked out by the incident photon beam. The excitation of an electron can happen at the valence band as well as at the core level by the incident photon beam. These different energy level excited electrons contribute predominantly towards the low energy spectral weight, thus the low energy tail region is comprised of extrinsic contributions consisting of inelastically scattered valence, core, Auger electrons and other multiple inelastically scattering events.

In an inelastic scattering event of a Valance electron, a hole is created in the valence band after the creation of valence band photoelectron by the incident photon beam of energy hv. The kinetic energy of the outgoing valence band is given by the equation

$$\mathrm{KEvalence} = hv - Ev1 - \phi, \tag{1.5}$$

When the valence photo electron coming out of the sample gets inelastically scattered, it transfers an energy $\mathbf{\Delta}$ to the neighboring valence band electrons, in this case the energy of outgoing valence band photoelectrons will be

$$\mathrm{KEvalence1} = hv - Ev1 - \mathbf{\Delta} - \phi, \tag{1.6}$$

After the $\mathbf{\Delta}$ eV energy is transferred by the valence photoelectrons to the other valence electrons they may be excited and leave the atom with kinetic energy following the conservation of the energy.

$$\mathrm{KEInelasticValence2} \leq \mathbf{\Delta} - EV1 - \phi, \tag{1.7}$$

The inelastically scattered valence band electron can lose some of its own energy via further inelastic scattering processes, hence the above equation has the less-than or equal-to inequality. These inelastically scattered valence band photo electrons contribute majorly towards the low energy spectral weight (LET) of the spectrum. Figure 3 shows the non-coincidence singles spectra of Ag(100); the shaded region is the approximate inelastic scattering contribution from the valence band photoelectrons. Further, there can be elastic scattering from the Core electrons as well. Both the inelastic contributions show up in the low energy tail of the coincidence auger spectrum. The shaded region in figure 4 is an estimate of the inelastically scattered valence band electrons.

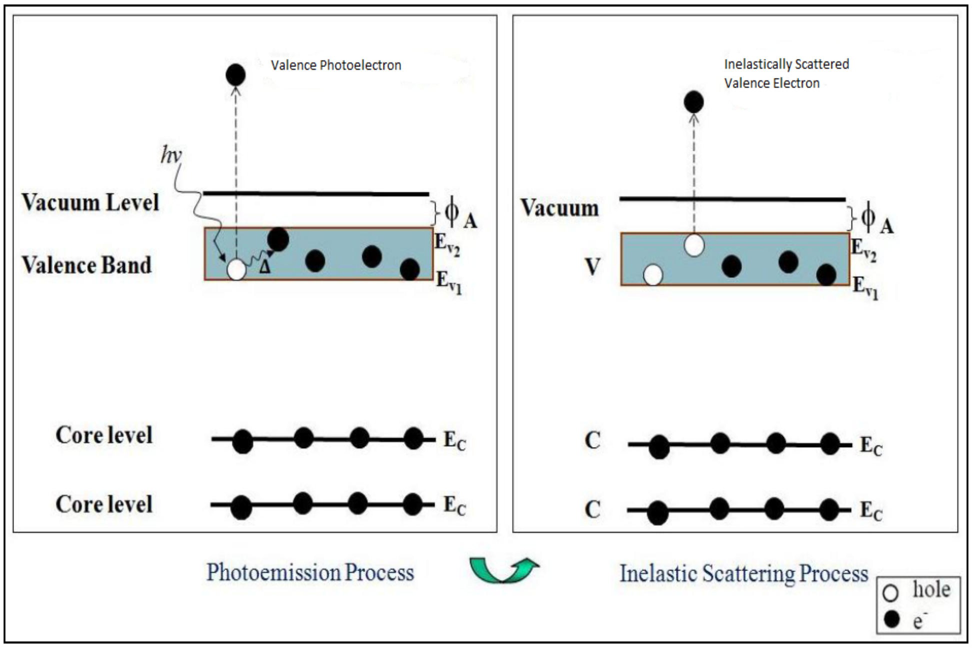

Figure 1-6 Inelastic scattering of the valence band electrons

Inelastic scattering event of photo-emitted valance band electrons is as seen in the Figure 1.6.

1.7 Qualitative and Quantitative Analysis Using APECS Spectrum

APECS characterization technique helps us in qualitative and quantitative analysis of the materials. We can extract the information about the chemical composition of the atoms of the solid surface by identifying the characteristic Auger peaks. For an analyst it is very important to remove the noise and background before interpreting any Auger line shape. This increases the accuracy and improves quantification. In AES and

XPS many quantification techniques have been developed to extract the Auger line shape from the background ever since AES and XPS have been used.

To quantify we used a linear equation given by M.P Seah [13], where the intensity from an element A of the solid I_A can be obtained from the spectrum and is proportional to the molar fraction content, X_A, in depth to which the sample is being analyzed

$$I_A = X_A * I_A^{\infty}, \tag{1.8}$$

Rearranging,

$$X_A = I_A / I_A^{\infty} \quad , \tag{1.9}$$

Here I_A^{∞} is the sensitivity factor measured from intensity of a pure element. The sensitive factor can be calculated by comparing with other pure elements. If the ratio of the sensitivity factors of the two elements ($IA\infty/IB\infty$) is known, then from it we can calculate

$$XA = \frac{I_A/I_A^{\infty}}{\sum_{i=A,B} Ii/I_i^{\infty}} \quad ,$$

Here the sum is all over the constituents in the solids. Measuring respective intensities of the elements we can calculate molar fraction of the element and compute how much element is present in the sample.

In the measured APECS spectrum for Ag 4p NVV, the LET contains a significant fraction of electron emission coincident with the background emission at the Ag 4p core level photoelectron kinetic energy, which is unrelated to the Ag NVV, 4p excitation event. These false coincidences include emission due to inelastic scattering of the Auger and valence electrons along with multiple electron Auger emitted by sharing the Auger energy. To generalize we can say the LET comprises of Auger related and unrelated contributions.

$$I_{LET}(E) = I_{LET\ Auger\ related}(E) + I_{LET\ Auger\ unrelated}(E), \tag{1.10}$$

The extrinsic contributions can be further classified as inelastically scattered electrons from the core and valence band.

$$I_{\text{LET Auger unrelated}}(E)=I_{\text{photoelectron}}\text{Inelastic}(E)+I_{\text{Auger}}\text{Inelastic}(E), \qquad (1.11)$$

Our goal is to separate the Ag 4pNVV APECS LET from inelastically scattered electron background that is the Auger unrelated contributions, leaving only the “pure” Ag LET spectrum created by the excitation of Ag 4p photoelectrons only. This would help in determining the I_A value which is characteristic only to the Auger transitions and thus result in a better quantification of the acquired data.

1.8 Sample Description

The Cu (100) and Ag (100) single crystal surface (with 100 plane) were studied using APECS. These transition metals, elements of the Group 11 of the periodic table were chosen. Although the Auger spectra (Auger region) from both of the samples are well established, the high spectral intensities at the low energy part of the spectrum have not been studied experimentally earlier. The sample electronic configuration is described below [14].

Copper (Cu)

Atomic number: 29

Electronic Configuration: $1s^2$, $2s^2$, $2p^6$, $3s^2$, $3p^6$,$3d^{10}$,$4s^1$

Table 1-1 Binding energies of copper

Shell		Sub shell				Binding Energies (eV)
		n	l	j=l + s		
K	K	1	0	1/2	1s	8979
L	L_{I}	2	0	1/2	2s	1096.7
	L_{II}	2	1	1/2	$2p_{1/2}$	952.3
	L_{III}	2	1	3/2	$2p_{3/2}$	932.7
M	M_{I}	3	0	1/2	3s	122.5
	M_{II}	3	1	1/2	$3p_{1/2}$	77.3
	M_{III}	3	1	3/2	$3p_{3/2}$	75.1

Silver (Ag)

Atomic number: 47

Electronic Configuration: $1s^2$, $2s^2$, $2p^6$, $3s^2$, $3p^6$,$3d^{10}$,$4s^2$, $4p^6$, $5s^1$, $4d^{10}$

Table 1-2 Binding energies of silver

Shell		Sub shell				Binding Energies (eV)
		n	l	j=l + s		
K	K	1	0	1/2	1s	25514
L	L_{I}	2	0	1/2	2s	3806
	L_{II}	2	1	1/2	$2p_{1/2}$	3524
	L_{III}	2	1	3/2	$2p_{3/2}$	3351
M	M_{I}	3	0	1/2	3s	719
	M_{II}	3	1	1/2	$3p_{1/2}$	603.8
	M_{III}	3	1	3/2	$3p_{3/2}$	573
	M_{IV}	3	2	3/2	$3d_{3/2}$	374
	M_{V}	3	2	5/2	$3d_{5/2}$	368.3
N	N_{I}	4	1	1/2	4s	97
	N_{II}	4	1	1/2	$4p_{1/2}$	63
	N_{III}	4	2	3/2	$4p_{3/2}$	58

As we conclude our introduction here, the further part of this dissertation describes the experimental apparatus, NSLS beamline configurations and its components in chapter 2. Chapter 3 describes experimental considerations and procedures. The APECS experimental data for low (180eV) and high energy (465eV) photon beam is presented in chapter 4. The VB coincidence measurement and the subtraction of Auger unrelated contributions after extrapolation method is described in detail. Chapter 5 presents the theoretical data along with the comparison of the ratio of LET to the Auger peak. An approximate theoretical model computing the intensity contributing from sample surface layers is done and compared with the experimental data in chapter 5. In the final chapter 6, APECS data is compared with the data obtained from PAES followed by conclusion and future work.

Chapter 2

Experimental Details

2.1 Introduction

The incident beam of photons was produced in a synchrotron in the form of synchrotron radiation. In a synchrotron, using bending magnets a charge particle accelerated in a circular-oval path. As the charged particles (fast electrons in magnetic field with large radius of curvature) are accelerated radially, they emit an electromagnetic radiation at each bend- turn. This electromagnetic radiation is collected, tuned, focused and directed towards the sample as a beam of photons. The beam of photons from synchrotron is highly polarized, has high intensity, and has a pulsed timing structure with tunability in a broad spectral range [15-20]. These properties of synchrotron radiation make a photon beam a best probe for spectroscopic studies.

The energy of the photon beam is in the wide range of Visible, Ultra Violet, X-ray regime that is from few meVs (10^{-3}eVs) to 10^{5}eV. In solids the electron binding energies are in the same energy range. The core electrons, Valence electrons bounded to the atom are involved in the chemical bonding; by probing them we can know the chemical and physical properties of the solid. The wavelength of the photon beam is in the order of 1000 nm to 1 nm. As the bond length of atoms and molecules is in this range, photons can be utilized to probe atomic and molecular structure of solids [20-22].

The experimental measurements reported in this dissertation were performed at beamline U1A of National Synchrotron Light Source at Brookhaven National Laboratory (New York), a US Department of Energy funded research facility.

2.2 Synchrotron Radiation

Synchrotron Radiation of variable energies is produced from storage rings. At National Synchrotron Light Source (NSLS) –I in Brookhaven National Laboratory, we have two electron storage rings, one for the X-ray and another for the ultra violet (VUV) region. A bunch of electrons is generated using an electron gun and accelerated using a LINAC (Linear Accelerator). The 120MeV linac uses RF systems and accelerating cavities. The accelerated electrons are injected into the storage ring for further acceleration using booster electron energy 750MeV [23].

The Storage Ring consists of six major components, all of which are controlled using a computer system:

1) Vacuum Chamber: This is a very low pressure 10^{-10} to 10^{-11} Torr chamber in which the electrons circulate in a closed trajectory.
2) Dipole Bending Magnets: These magnets are used to direct the electron circulate in a closed orbit inside the vacuum chamber. These also make the beam bend around the corners.
3) Injection: This system generates and accelerates electrons in the storage ring.
4) RF Cavities: At the each bend the electrons lose energy in the form of synchrotron radiation. The radio frequency cavities restore the electrons energy. A high voltage by RF field of 2856MHz accelerates the electrons from 100KeV to 116MeV.
5) Focusing Magnets: These are quadruple magnets and are utilized in horizontal and vertical focusing of the electron beam in the storage ring.
6) Insertion Device: In the straight section of the ring is a periodic array of magnet guides which focuses the electron beam.
7) Computer Controls: The changes in the system, beam functions and its components are monitored and controlled using a computer system.

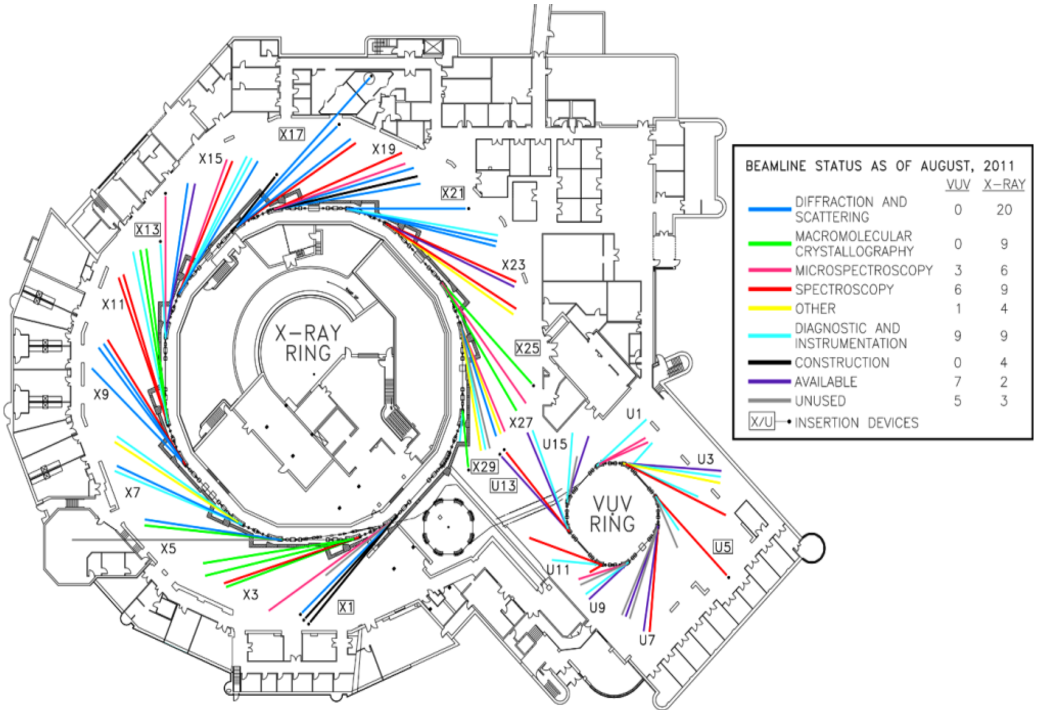

Figure 2-1 The NSLS, X-ray and VUV ring floor plan [23]

The electron beam after accelerating from LINAC and RF cavities, is fed in the form of electron bunches to the VUV ring and X-ray ring. In the ring it is further accelerated to attain its maximum energy. In VUV ring, up to 9 bunches of electrons orbit in the ring at the energy of 800MeV with a maximum beam current 1000mA. The injection system turns off as the desired energy and beam current is achieved. With the dipole and quadruple magnets the beam is focused and circulated in the storage ring. At each bend the electron bunches-beam loses energy in the form of synchrotron radiation. Photon shutters which are present at the bend allow the beam to travel down through beam lines and end stations. The energy of electron bunches is restored using RF cavities (52.89 MHz) [24, 25].

In the VUV ring, of the 9 electron bunches 7 are filled, leaving 2 empty. The orbital period of electrons around the ring is 170nS; this implies the bunch to bunch separation time is ~19.2ns. The VUV ring hosts 16 beamlines.

2.3 Beamline U1A and ERG Monochromator

The beam is directed to the work station (sample) with the help of a series of optical elements and a monochromator. The synchrotron radiation has a range of energy; to select a particular energy a monochromator is employed. The ERG (Extended Range Grasshopper) monochromator designed by F.C Brown and S.L Hulbert is used in beamline U1A [26]. The scan motion is controlled by computer selecting a particular range of photon energy. The beam layout is shown in the figure 2.2. The beamline consists of various collection and focusing mirrors, ERG monochromator and sample chamber [4, 27]. The radiation is focused and dispersed in a vertical plane using the ERG monochromator. The monochromator has the following components: mirror M1, M2 and gratings G1 and G2. Mirror M1 is 30 cm long, elliptical, is gold coated, and is fixed (52 cm) from the entrance slit S1. The slit S1 demagnifies the beam, making it horizontal with a ratio of 7:1. M2S1 is codling mirror/slit combination. The beam is steered into 1200 lines per mm gratings G1,G2, G3 of 2m, 3.7m, 5m radius of curvature. The monochromator resolution can be adjusted by varying the slit width of the entrance (S1) and exit (S2) of the monochromator. The monochromator scans in a Rowland Circle Geometry which is related to Vodar-type geometry for the gratings. The Rowland circle rotates with S2 as axis producing a fixed beam in the exit slit direction. On the arm of S1G grating is mounted, the arrangement of M1S1G rotates around the axis of S1 making it parallel to the incoming beam. A smooth, straight line motion of M1S1G assembly is accomplished with the help of linear air bearing which are aligned with reference to ground granite slab. The Codling mirror/ slit assembly and two grating arms rotate with the help of precession ball bearings.

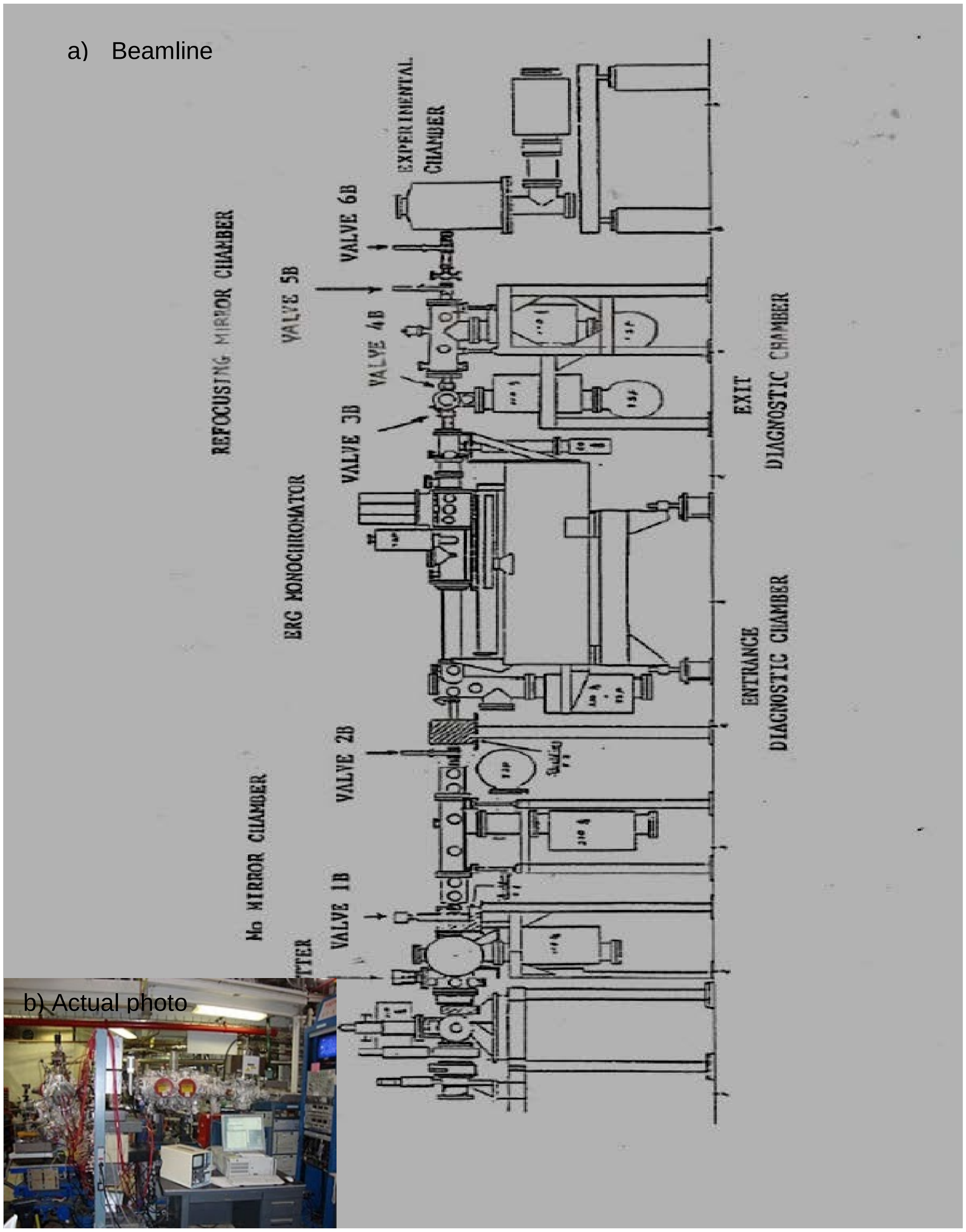

Figure 2-2 a) Beamline U1A components, NSLS [15], b) (inset) actual photograph

The optical alignment and the motion (angular) of the grating arms, optical elements, tilts of mirror, and linear motion of the ball bearings are controlled by four stepping motors with optical shaft encoders along with mechanical limit switches. The stepping motor is controlled by a Universal High-Performance Motion Controller/Driver (Newport ESP700) enabling continuous wavelength scan of the monochromatic beam. In our experiments 2m grating was used for the energy range. The 3.7m grating is used for photon energies between 450eV to 750eV.

2.4 Vacuum Equipment

The beamline and the end station are under ultrahigh vacuum, the vacuum is achieved by various pumps, including rotary, turbo, ion and Ti sublimator in combination. The pressure range of ultrahigh vacuum (UHV) is typically achieved in two steps. First a Turbo pump (Pfeiffer TPU- 050 (50 liters per sec)) backed by a rotary vane pump Varian SD-90 is used to pump the system to a base vacuum of 10^{-6} Torr, and from base pressure an ion pump (Perkin Elmer Model #2070122 (120 liters per sec)) brings the pressure in the UHV range that is in 10^{-11} Torr. The system was baked out to attain UHV. In the bake out process the system is heated externally. The heating causes the chamber-system surface to degas, the contaminants or the gas molecules are desorbed from the inner wall of the chamber-system, which are pumped out by the vacuum pumps. Thus, the bake out process increases desorption and the diffusion rate which significantly reduces the time to attain UHV.

2.5 End Station: UHV Chamber

The end station consists of a cylindrical shaped stainless steel UHV Chamber (figure 2.3) equipped with standard ion and turbo molecular pumps to attain a vacuum of $\sim 10^{-10}$ Torr. The chamber is typically baked overnight for attaining the UHV. The chamber has two eight inch ports to accommodate electron energy analyzers called cylindrical

Mirror Analyzers (CMA). The ports are oriented 145° from each other from a plane 10° below the horizontal. For cleaning the sample with sputtering technique a sputter ion gun is installed in the chamber. The chamber has provisions for Argon gas line and Oxygen gas lines, with Argon lines especially used during sputtering.

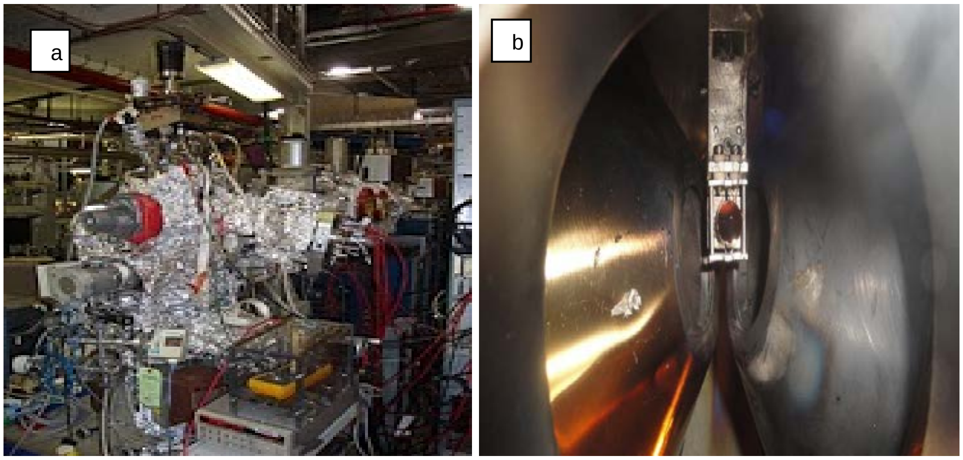

Figure 2-3 (a) Sample chamber and (b) Cu sample in the sputter position

The sample is fixed on the sample manipulator and has four degrees of freedom (up-down, right-left, forward- backward, rotation) x, y, z, θ. The chamber height can be adjusted using adjustable kinematic mounts. With the adjustment of the mounts a better count rate can be achieved due to better alignment of the beam, sample, and the focus of the analyzer.

2.6 Cylindrical Mirror Analyzer

To detect electrons coming out from sample surface we used two cylindrical mirror analyzers (CMA) (PHI Model 15-225G). One of the CMA's is used to detect core level photo electrons and other to detect the Auger and secondary electrons. The two CMAs are in a plane 10° below the horizontal at 145° from each other. This geometry helps in getting the maximum intersection of the focusing area of the CMAs on the sample surface. The double pass configuration of the CMA filters out high and low energy electrons to select the desired energetic electrons. The CMA has two concentric metallic cylinders. The inner cylinder is positive biased with respect to the outer cylinder, creating a radial electric field from inner to outer cylinder. The inner cylinder has an aperture covered with a grid to allow entry of electrons in the region between concentric cylinders. These apertures can be varied from small to large by means of a knob on the back of the flange. The choice of aperture involves a compromise. A larger aperture will allow for higher transmission through the analyzer, but the use of larger aperture results in a decrease in the energy resolution. The large aperture has a resolution of 1.6% of the pass energy and the small aperture setting results in a resolution of 0.6% of the pass energy. The flange to sample distance is approximately 27.94 cm.

Besides the above mentioned: Channeltron, Analyzer, Variable Aperture, retardation grid the other components are internal gun and deflection plates.

2.6.1 Working of the CMA

The electrons come out from the sample in different angles and with different energies. Our CMAs are fixed in position so they can detect electrons emitted at an angle of 48°± 5°. The electrons enter the region of radial electric field from inner cylinder to outer cylinder after passing through a pair of hemispherical grids present at the mouth of the CMA. The difference in voltage between inner and outer cylinder determines the pass energy. The relation between voltage (potential difference) and energy of electrons passing through analyzer in the CMA model PHI 15-225 is $E_{pass} \sim 1.7e(V_{IC}-V_{OC})$; here 'e' is electronic charge, V_{IC} and V_{OC} means inner and outer cylinder voltage respectively and pass energy is measured in eV. The high energy electrons get deflected and hit the outer cylinder, with only the electrons whose energy equals the pass energy succeeding to reach the detector. If the electron energy is below the pass energy it will hit the near edge of the exit slit. If the electron has energy above the pass energy the deflection will overshoot the exit slit opening and hit the far end of the exit slit.

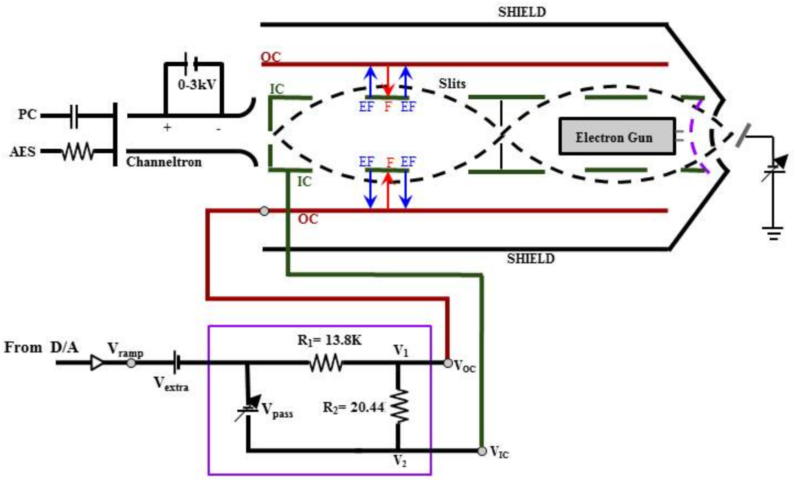

Figure 2-4 CMA schematics and its working

The double pass design efficiently filters out the background due to secondary electrons generated in the analyzer. The inner cylinder is positively biased with respect to outer cylinder. The outer cylinder is negatively biased and this repels the electrons and compels them to pass from the region between inner and outer cylinder to reach the electron multiplier. The higher the applied voltage between cylinders the stronger is the repulsion by the outer cylinder, thus by setting the voltage between inner and outer cylinder we can measure the desired energetic electrons. To make it possible to detect a single electron signal measurable the channeltron electron multiplier amplifies with a gain of ~10^6- 10^7. This signal may be further amplified if needed. The current output of channeltron is always kept below 0.1µA to protect and increase its life.

The CMA can be operated in two modes: retarding and non retarding modes. We use the retarding mode where the electrons entering the double pass CMA are either accelerated or decelerated with fixed pass energy (PE). The energy resolution (ΔE/PE) of our CMA in retarding mode with small aperture is 0.6% and with large aperture is 1.6%.

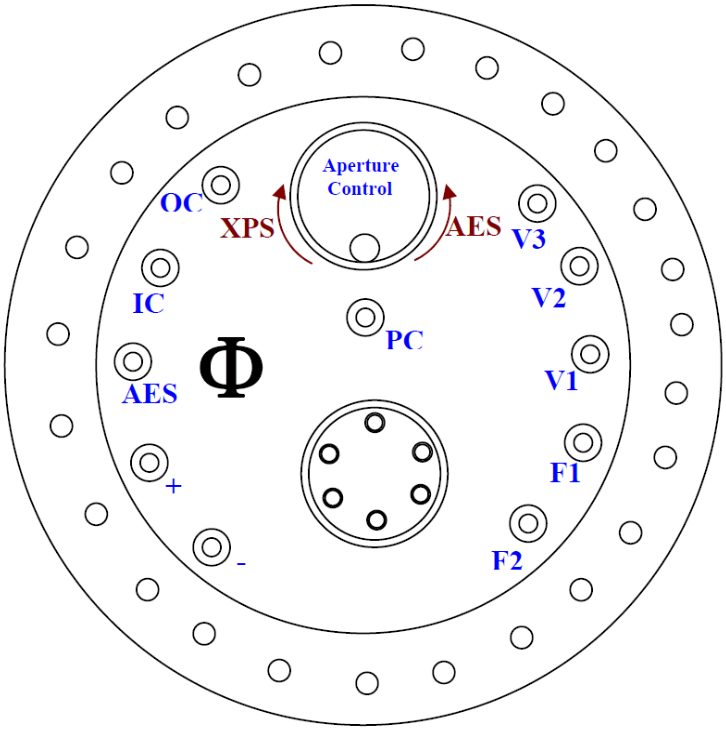

Figure 2-5 The flange and the aperture control of PHI model 15-255G Precision electron energy analyzer

We use two CMAs for the measurement of electrons in coincidence with each other. Once the CMA is fixed on a particular energy, (core shell energy) called fixed CMA and the other CMA called scan CMA, scans a range of energy (10-85 eV, low energy part of the spectrum).

2.7 Coincidence Electronics

The main components of the coincidence electronics are Amplifiers, Constant Fraction Discriminator (CFD), and Time to Amplitude (TAC) converter as shown in the figure. The output signal from the each cylindrical mirror analyzer (CMA) is amplified and discriminated and is fed to the TAC. The output from one CMA acts as a start signal for TAC and the output from other CMA acts as a stop signal. To bring the true coincidence data completely into the positive time difference regime the stop signal is delayed before it is fed to the TAC. The TAC generates an output signal whose amplitude is proportional to the time difference of the start and stop signal. The output signal with particular amplitude (height) is recorded as a histogram of pulses with particular height binned in the corresponding timing channel in the multi-channel analyzer (MCA).

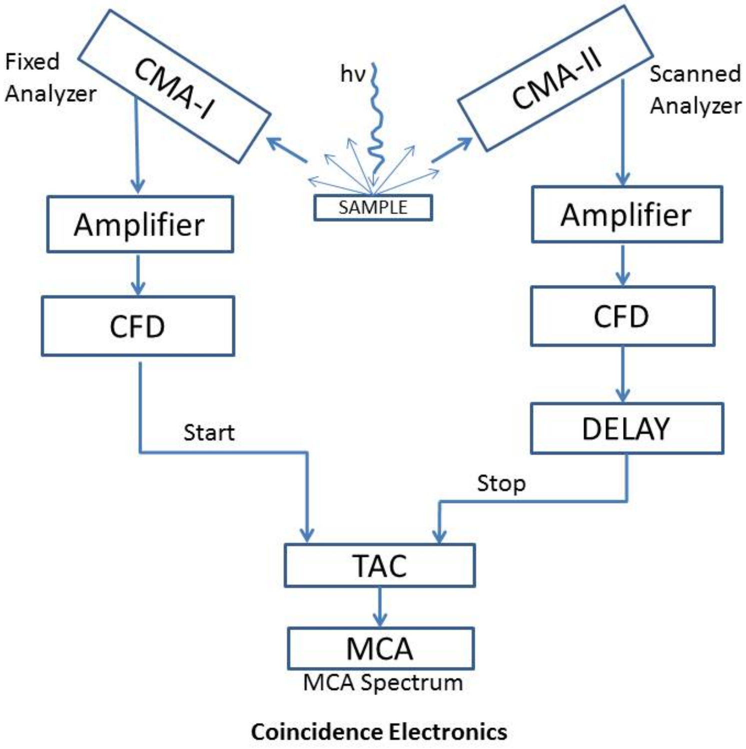

Figure 2-6 Coincidence Electronics

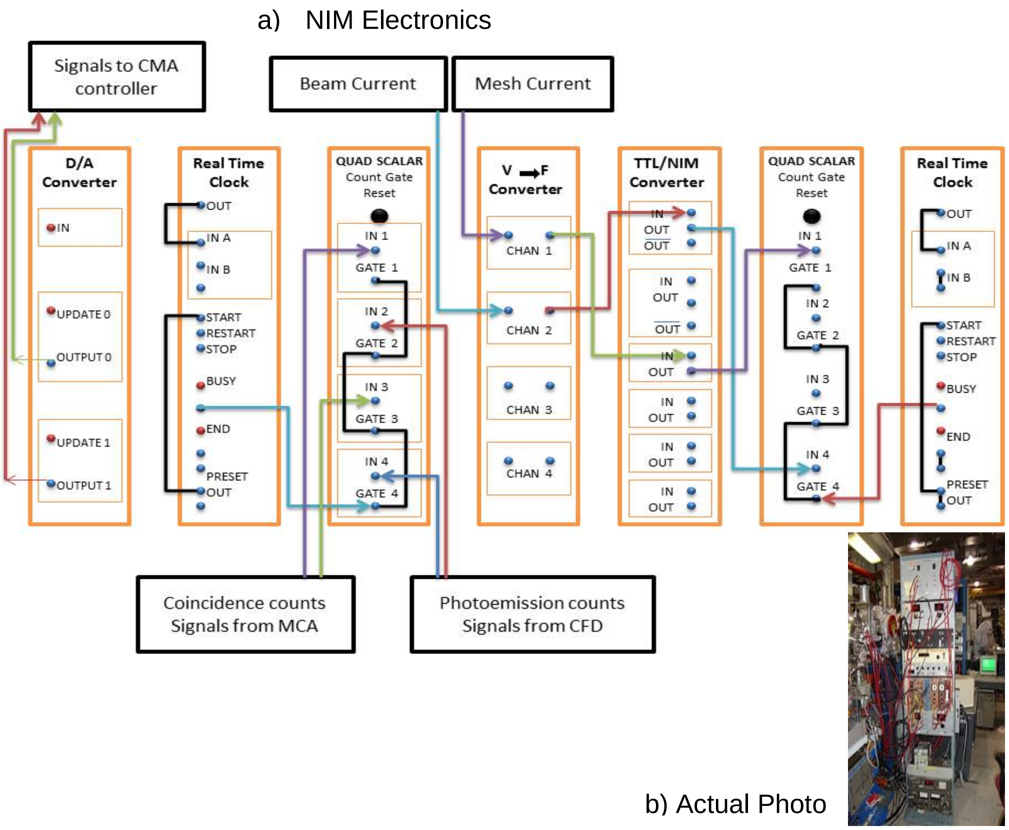

a) NIM Electronics

b) Actual Photo

Figure 2-7 a) NIM electronics above and b) actual experimental floor electronics rack

Amplifier: To amplify the signal from the CMA we used Model 612AM, which is a 6-channel NIM standard module. The signal is amplified 40 times via internal amplifiers for six input channels.

Constant Fraction Discriminator (CFD): CFD is used to discriminate signal from the noise and to generate a clean timing pulse. A lower reference level (constant fraction) is set and only the pulses above the reference level are accepted. The CFD minimizes the random timing caused from the pulse height variation. An important role of CFD is the correction of the timing, that is, the rise time of signals with height variation are corrected and made of the same rise time independent of pulse height by generating a timing pulse at a constant fraction of the maximum pulse height of the input pulse.

Delay: ORTEC model 425A nanosecond delay unit with a range of 0 to 63 ns with increment steps of 1ns provides a calibrated delay to the stop signal. We used two delay units connected sequentially so as to get a delay of 126ns. The unit can operate without a power source. Besides the delay unit the wires also introduce a delay in the signal proportional to wire length, approximately 1ns per foot.

Time to Amplitude converter (TAC): To measure the time interval between the start and stop signals we used the ORTEC Model 566 Time to Amplitude converter (TAC). The TAC generates an analog output where the amplitude is proportional to the time difference of start and stop. This analog output is connected to the multi-channel analyzer via a DC coupled input. The signal from the 'fixed' CMA which in the APECS experiment is used to collect core photoelectrons is used as Stop signal. This is fed to the TAC after a delay of 126ns. The pulse height of 8V corresponds to a 500ns range of the TAC. The signal from the 'scanned' CMA is fed to the TAC as a Start signal. To explain with an example of APECS measurement, let us consider the Auger transition in Ag 4P, NVV. The fixed CMA collects the electrons coming from the 4P core at 133eV and generates a start signal. The detection by the second CMA of the electron emitted as a result of the NVV Auger transition.

Pulse Height Analyzer (PHA): The counts are displayed in the form of a histogram as a function of time. The output of the TAC which is a pulse in the voltage range 0-8V is the input for the PHA. The multichannel analyzer has 1024 channels and these channels are equally divided into 500ns, an input range of TN7200. The TAC pulse input is converted to time ~500ns and further converted into counting pulse of a particular height. Depending on the voltage of the pulse the counts are put in a particular channel.

Region of Interest (ROIs): These are the regions (area under peaks) giving total counts of True and Accidentals. ROI0 gives the sum of counts of Trues and Accidentals and ROI1 gives sum total of Accidental counts. The difference between two ROIs gives total True counts. Typical width of the ROI peak is around 52 to 56 channels.

Ratemeter: The ratemeter is an analog device used to measure the number of counts coming from the channeltron. The ratemeter is used to find an approximate value of the counts and especially to get an idea of the max counts. The ratemeters (one for each CMA) aid in the alignment of the beam, sample, and the detectors. The alignment is of critical importance as the effective count rate is determined by the degree with which two CMAs focus the same sample volume.

2.8 Timing Electronics

The two detectors: CMAs (cylindrical mirror analyzer) are two single channel detectors, one counting the electrons of core photoelectron peak and the other counting the Auger electrons at a characteristic energy. These electrons when detected in coincidence correspond to a coincidence count. Let us consider R as the rate at which core holes are created per unit time per unit volume. The rate R is directly proportional to the incidence flux of the photon beam. Each core hole photoionization event causes two or more Auger electrons and it takes around 10^{-14} seconds for this Auger transition. The Auger electron emitted as a result of the core photoelectron are said to be in true time coincidence. Besides the emission of Auger electrons there is a steady emission of electrons, inelastically scattered photoelectron and Auger electrons, which is proportional to the incident flux and is characterized by signal to signal plus background ratio γ_i corresponding to each channel. The singles count rate ν_i each CMA (i=1,2) detects is given by equation.

$$\nu_{s\,i} = \frac{\alpha_i R V_i}{\gamma_i}, \tag{2.1}$$

Here V_i are the detection volumes, α_i are the detector efficiencies representing the probability of core hole creation in the appropriate region and subsequently an Auger electron is created and detected by the Auger analyzer with photoelectron detected by the photoelectron analyzer, γ_i is the ratio of signal to signal plus background.

The coincidence event is dependent on the maximum time separation, τ, between two independent events. The coincidence can be understood by the analogy of a AND logic gate, where the output depends on the (two) similar inputs. The two singles channels from the detector are the inputs to the gate and the output is the coincidence channel V_c that is the coincidence event that happens in selected time 'τ'.

We measure the accidental rate in the real time. Measuring 'ROI1' provides us an excellent estimate of the accidental rate. The true coincidence rate is directly proportional to the R- rate at which core holes are generated and is given by equation (2.2),

$$\nu_T = \alpha_1\alpha_2 \mathrm{RV}_c\,, \qquad (2.2)$$

V_c is the area intersected by the two detectors.

As there is a finite probability of the two unrelated events occurring in the time interval τ, there is contribution to the coincidence rate ν_c from the unrelated events called accidentals. The accidental count rate ν_A is proportional to R^2 and is given by equation (2.3),

$$\nu_A = \nu_{S1}\nu_{S2}\ \tau = \frac{\alpha_1\alpha_2 \mathrm{R}^2 \mathrm{V}_1\mathrm{V}_2}{\gamma_1\gamma_2}\tau\,, \qquad (2.3)$$

The coincidence count rate ν_c is the sum of ν_A and ν_T,

$$\nu_c = \nu_A + \nu_T\,, \qquad (2.4)$$

From the above equations ν_A and ν_T will be equal when,

$$R = R_c = \frac{V_c\,\gamma_1\gamma_2}{V_1 V_2\,\tau}\,, \qquad (2.5)$$

Here Rc is the core hole creation rate per unit time per unit volume in the coincidence channel. As the accidental count rate grows to the square larger as the R in true count rate exceeds the Rc. Thus it is necessary to control the incident flux, that is, to reduce the incident beam flux to keep the ratio of ν_A to ν_c in the range which optimizes count rate and the signal to noise ratio of the true counts. The incident beam flux is adjusted such that to get optimum statistics in a reasonable period of time [27].

The MCA records the timing spectrum which reflects the timing structure of the synchrotron bunches. As shown in figure 2-8, the two tallest peaks correspond to the coincidence and accidental events. The coincidental ('C') and accidental ('A') peaks show the counts from the coincidence and accidental events. By coincidence event we mean here is photons from the same synchrotron bunch create the photoelectron and Auger electrons, which are detected by the CMAs at the same time ± 15ns. An accidental event is when by the accidental coincidence of photoelectron and auger electron. For example, the CMA detects electrons in correspondence with photons from the other synchrotron bunch the event considered to be an accidental event when one CMA detects a core photo electron from one atom and other CMA detects an Auger electron from different atom. In a true event, one photon comes in, two electrons comes out from the sample detected in coincidence (example: core photoelectron and its corresponding Auger electron detected in APECS measurement) whereas in an accidental event we have coincidence detection of two unrelated electrons which arise from two unrelated photons.

As the initial bunch travels around the ring it takes 170ns, hence the accidental peak appears after 170ns of the coincidence peak. The other short peaks are due to 7 filled buckets out of a total of 9 buckets. The true coincidence and accidental coincidence both contribute towards coincidence peak C. The x-axis of the timing spectra shows the timing between singles events, Δt shows the timing difference of electrons reaching both the CMAs. The width of the peaks is affected by the timing resolution of the detectors (CMAs), and other electronic units. The other contribution to the width is from the width of electrons in the storage ring (~1ns).

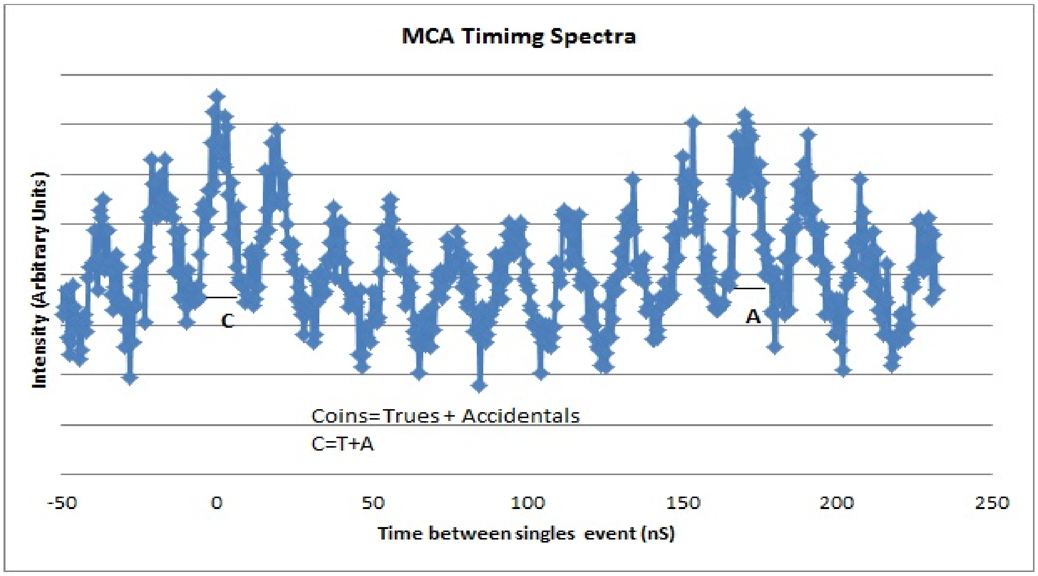

Figure 2-8 MCA timing spectra of synchrotron bunch from the VUV ring

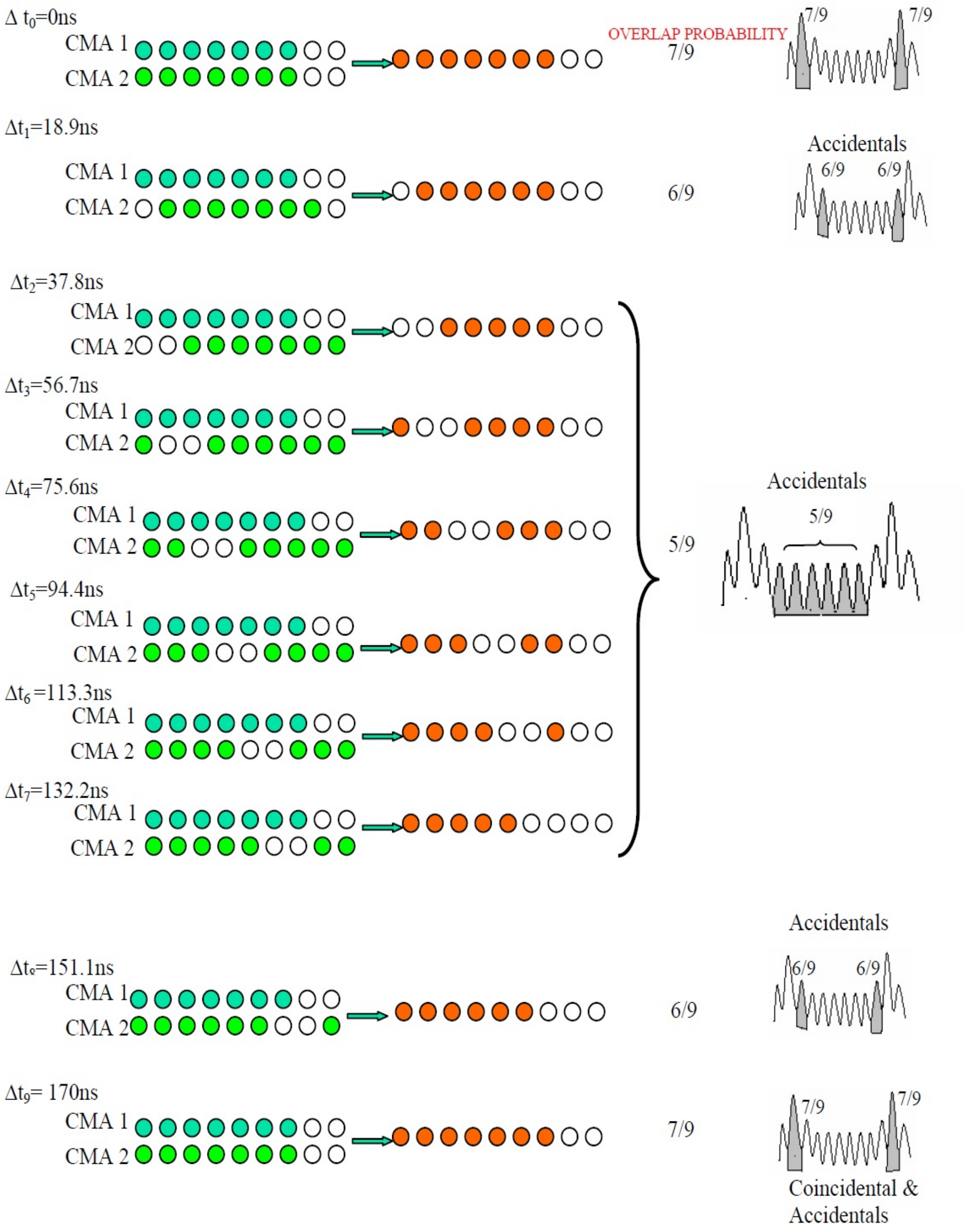

Figure 2-9 Timing overlap of filled and empty electron bunches

The photons from the first bunch are incident on the sample creating photoelectrons and the Auger electrons. Let the fixed CMA detect high energetic core electrons and the scan CMA scans a range of low energetic electrons including Auger electrons. As the first bunch of photon beam of ~1mm diameter excites the sample, it excites many atoms of the sample. For our understanding, let's consider two atoms that are excited by the photon beam. Atom 1 creates a core photoelectron core1 and corresponding Auger electron CVV1, and in the same manner Atom 2 creates a core photoelectron core2 and corresponding Auger electron CVV2. When fixed CMA detects the high energy core1 and scan CMA detects corresponding valence electron CVV1, that is when both the detectors detect electrons from the same atom and from the same bunch, we call this as a true coincidence event. But when the fixed CMA detects high energy core1 of the first atom and the scan CMA measures CVV2 from the second atom and vice versa for core2-CVV1, this event is called an accidental event. Although the electrons have the same pass energy and are caused by the same bunches, they don't arise from the same atom, and hence are accidentals. These events also lie in the same time region of the true coincidence that is in the ROI0; hence the coincidence peak has true as well as accidental counts. The accidental events also occur after the photons caused from the first bunch of electrons hit the sample, approx. 19ns after first one, and photons from second bunch comes in. Then the fixed CMA detects core2 and the scan CMA detects CVV1. Refer to sequence two of the figure. During the empty bucket/bunch, no photons are generated, and the fixed CMA detects core electrons generated by photons from first electron bunch while scan CMA does not detect electron. Since there can be no accidental coincidence when an empty bunch overlaps with a filled bunch we would expect the accidental rates to vary with time delay, Δt, between the detected electrons according to the pattern shown in Figure 2.9. Note that at a time difference of 170 nsec (1 ring cycle) we expect the accidental rate to be the same as at Δt= 0 nsec.

The accidental rates are proportional to the count rate of each detector (CMA) and the average rate is the same for coincident and accidental peaks due to the conservation of the accidental coincidences. The data can be acquired in four formats, two singles spectrum from both of the detectors (CMAs), coincidental and accidental spectrums. A wide range scan by the CMAs results in the singles spectrum, which is a non-coincidence spectrum. The other two kind of coincidental and accidental spectrums are obtained from the MCA timing spectrum with a timing difference of ~170ns. The statistical noise in the spectrum can be minimized after we take data for a long time.

The next chapter (3) we discuss our experimental consideration while acquiring data for Ag (100) and Cu (100) using the APECS experimental setup.

Chapter 3

Experimental Considerations

3.1 Introduction

In this chapter the experimental considerations for acquiring data, MCA timing, true coincidence data corrections are discussed.

The APECS technique employs photons to knock out core electrons which emerge as the core photoelectrons. The vacancy in the core is filled by the electrons from the valence band and further the emission of the Auger electron. The theoretical time difference between core photoelectron and the Auger electron generation is of the order of 10^-15 sec and the timing resolution of the electronics is of the order of 10^-9 sec, hence for experimental measurements the emission of the core and photo excited Auger electron from the same photo excitation event appear to be simultaneous. These correlated electrons emitted from the solid surface are measured in time coincidence by the two cylindrical mirror analyzers (CMA), one CMA detecting the photoelectron and the second CMA scanning the low energy range containing the Auger electrons.

In coincidence experiments, long data taking times are typically needed to obtain adequate statistics. If we increase the flux, it does not significantly reduce the time for acquiring better statistics data. This is because the signal is the difference between the counts in ROI(0) [accidental + trues] and ROI(1) [coincidences]. Also in in flux increases the energy resolution of the spectrum. Thus while acquiring the data we need to optimize the photon beam flux so as to get the best energy resolution and high statistics data in optimal and reasonable time.

3.2 Sample Characterization and Preparation

The dimensions of the single crystal Ag(100) and Cu(100) samples used in our APECS experiment had a thickness of 3mm and the diameter was 10mm. The incident photon beam energy was set to 180eV and at 200eV for the silver and copper samples respectively and a wide range scan spectrum was collected. Figure 3.1 shows the full range scan from 0 to 180eV consisting of peaks of the valence band, core and Auger peak and highly intense low energy range.

To keep the sample surface clean it was sputtered and annealed every alternate day. The commonly observed impurities on the surface of metals are carbon, sulphur, nitrogen and oxygen. Even though the sample is in UHV, over the time it can get oxidized. To remove these impurities the samples were sputtered every alternate day, and the ion beam of Ar+ was bombarded for 20 mins. After sputtering the sample, annealing was done by the radiative heating by the filament present right beneath the sample; a temperature of about 600 °C was achieved. The filament current was set at 5.3 A. The heating rate was accelerated by applying a potential of 1000 kV between the sample and the filament.

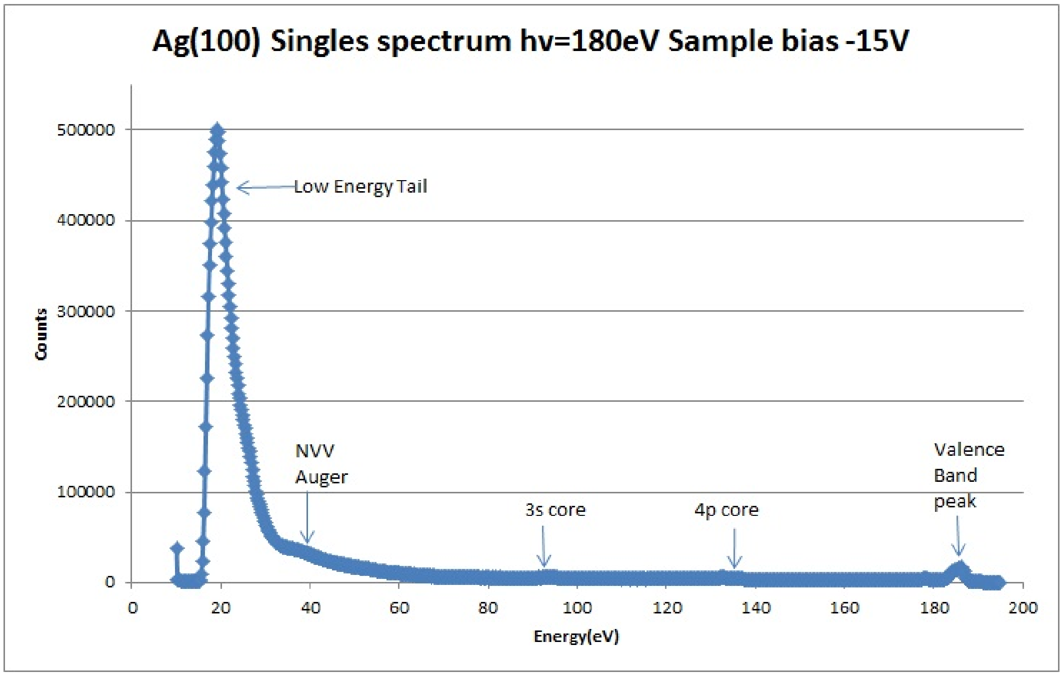

Figure 3-1 Ag(100) Photoelectron singles spectra, incident photon beam of energy 180eV, sample biased at -15V

The annealing helped the sample to remove the bulk impurities and smooth the sample surface after ion bombardment [28]. The temperature was measured using the thermocouple connected with the sample and voltmeter. The thermocouple voltage reading was calibrated to the temperature where 25mV indicated 600 °C.

3.3 MCA Timing Spectra

The electron kinetic energy affects the time interval for electrons to reach the CMA entrance mesh after they are photo excited from the sample. In our measurement, the scan CMA was used in step of 1 eV to allow electrons with energy 0-70eV to be detected. It’s of vital importance to know and understand how differently energetic electrons reach the detector that is to know how the coincidence timing varies with energy, in other words variation of the ROI(0) and ROI(1) with electron energy. This variation also changes with the fixed analyzer energy. Hence throughout the experiment for different fixed energies we measured the timing spectra at each energy point. Figures show the MCA timing spectra for fixed energy 145eV, showing the Coincidental and Accidental peaks. The ROI(0) and ROI(1) variation with the kinetic energy were similar to each other and an approximate difference of 350 channel numbers was observed consistently in figure 3.2.

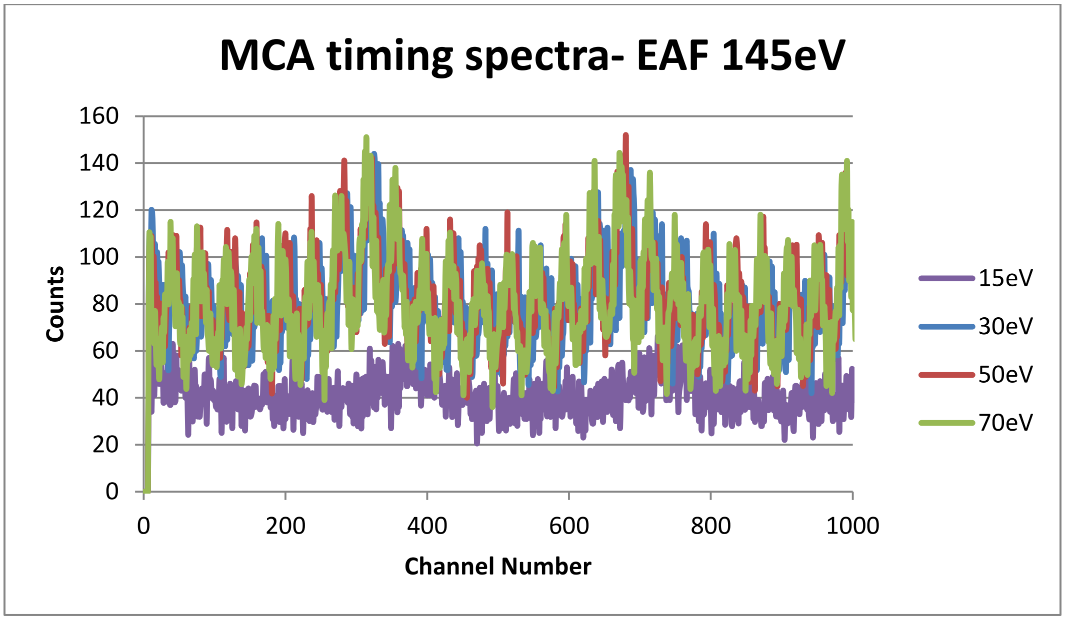

Figure 3-2 MCA timing spectrum for fixed analyzer at 145eV

Time of flight of electrons to reach detector from the sample surface is derived below.

Let ‘l’ be the distance travelled by electrons from the sample surface to the detector (channeltron),

$$TOF = \frac{l}{V_{avg}}, \qquad (3.1)$$

The time of flight TOF will be distance travelled over average velocity of the electron. Inside CMA the electron travels in an electric field region, let the initial velocity be Vi and the final velocity be Vf. The kinetic energy of the electron with velocity V and mass m is,

$$E = \frac{1}{2}mV^2, \qquad (3.2)$$

Implying $V = \sqrt{\frac{2E}{m}}$,

$$Vi = \sqrt{\frac{2E}{m}}, \qquad (3.3)$$

As the electron is accelerated by sample bias (SB) its final velocity

$$Vf = \sqrt{\frac{2(E+SB)}{m}}\ , \qquad (3.4)$$

The average velocity,

$$Vavg = \frac{V_i+V_f}{2} = \frac{1}{2}\left(\sqrt{\frac{2E}{m}} + \sqrt{\frac{2(E+SB)}{m}}\right), \qquad (3.5)$$

Equation 3.1 becomes,

$$TOF = \frac{l}{\frac{1}{2}\left(\sqrt{\frac{2E}{m}} + \sqrt{\frac{2(E+SB)}{m}}\right)},$$

$$TOF = \frac{2l}{\left(\sqrt{\frac{2E}{m}} + \sqrt{\frac{2(E+SB)}{m}}\right)}, \qquad (3.6)$$

It can be observed from the above equation that the electron time of flight is dependent on its kinetic energy.

Our APECS experimental measurement majorly involved collecting the background data by keeping one CMA fixed at various energies in between the core peaks and the valence band, which needed the ROIs variation with the fixed energies. Figure 3.3 shows the ROI variation with electron kinetic energy for various fixed energies. The curves were fitted with non-linear curve fit, double exponential form, in Origin, the curve fit equation and the values of the constant were used in data extraction and in the algorithm that controls communication between the computer and MCA. The equation obtained increased the accuracy of the data extraction and produced a better T/A ratio as the subtraction of coincidental with accidentals becomes more accurate.

3.4 Origin Curve Fits for MCA Timing Spectra

We used Origin nonlinear curve fit to fit the MCA timing data for each of the fixed energies. The ROI peak vs Electron kinetic energy variation for respective fixed energy was plotted and was fit with the double exponential decay equation. The equation and its fitting parameters constants obtained were used is program algorithm while taking and extracting the data. We could accurately measure the MCA timing variation for all fixed energy; this helped us in increasing the accuracy of locating the coincidental and accidental peaks with better T/A ratio hence to get accurate trues after subtracting coincidental counts and accidental counts. Figures below (3.3 and 3.4) are the double exponential decay equation: $y= y0 + A1*\exp(-x/t1) + A2*\exp(-x/t2)$; fit for the ROI0 and ROI1 variation with the scan energies for the fixed analyzer energy at 145eV [for other plots see Appendix B]. The values of the constants obtained after curve fitting are tabulated in table below for all of the fixed energies.

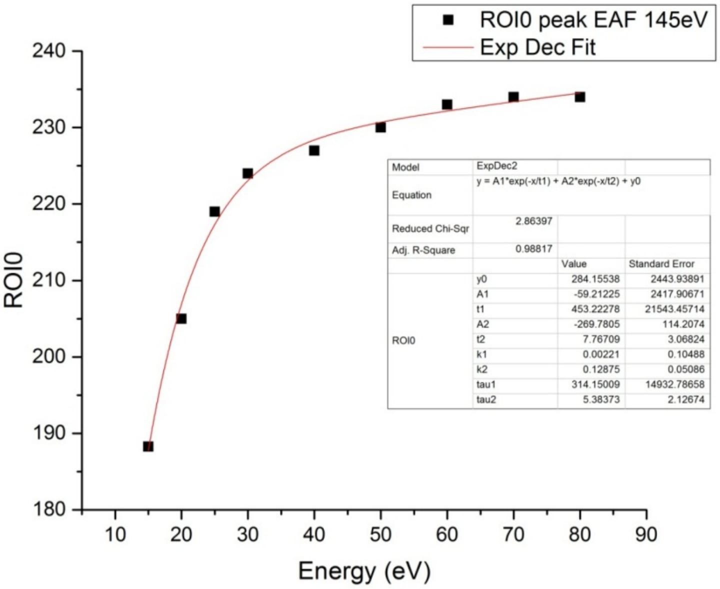

Model	ExpDec2		
Equation	y = A1*exp(-x/t1) + A2*exp(-x/t2) + y0		
Reduced Chi-Sqr	2.86397		
Adj. R-Square	0.98817		
		Value	Standard Error
ROI0	y0	284.15538	2443.93891
	A1	-59.21225	2417.90671
	t1	453.22278	21543.45714
	A2	-269.7805	114.2074
	t2	7.76709	3.06824
	k1	0.00221	0.10488
	k2	0.12875	0.05086
	tau1	314.15009	14932.78658
	tau2	5.38373	2.12674

Figure 3-3 Origin Curve fit for ROI0 peak channel number variation with the scan energy for fixed analyzer at energy 145eV

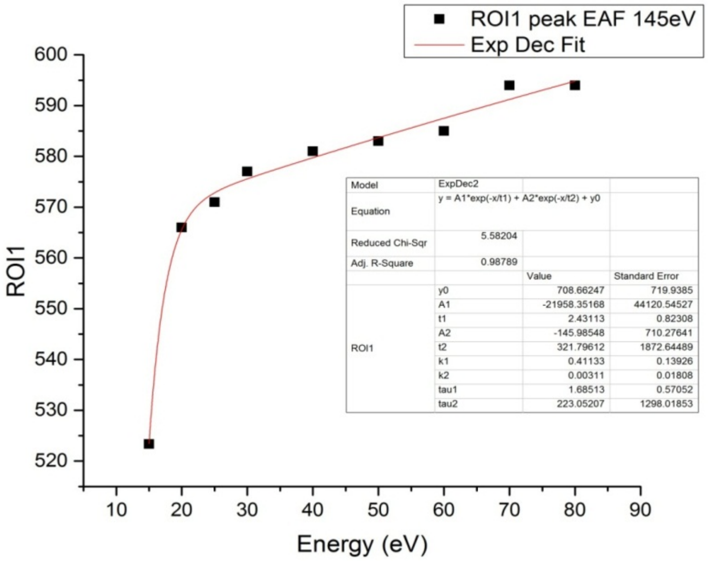

Model	ExpDec2		
Equation	y = A1*exp(-x/t1) + A2*exp(-x/t2) + y0		
Reduced Chi-Sqr	5.58204		
Adj. R-Square	0.98789		
		Value	Standard Error
ROI1	y0	708.66247	719.9385
	A1	-21958.35168	44120.54527
	t1	2.43113	0.82308
	A2	-145.98548	710.27641
	t2	321.79612	1872.64489
	k1	0.41133	0.13926
	k2	0.00311	0.01808
	tau1	1.68513	0.57052
	tau2	223.05207	1298.01853

Figure 3-4 Origin Curve fit for ROI1 peak channel number variation with the scan energy for fixed analyzer at energy 145eV

Table 3-1 ROI0 variation fitting constants for fixed energies

	133eV	145eV	152eV	159eV	166eV	173eV
y0	234.06217	284.15538	233.9	232.9423	186.81207	238.84715
A1	-58.41804	-59.21225	-54.32061	-48.79395	28.08254	-4.48901E10
t1	19.95276	453.22278	22.49329	25.00789	-158.54138	0.72228
A2	-4.48544E9	-269.7805	-2.97245E9	-1.2556E9	-3126.73888	-42.06671
t2	0.79247	7.76709	0.83139	0.8585	3.39417	33.55348

Table 3-2 ROI1 variation fitting constants for fixed energies

	133eV	145eV	152eV	159eV	166eV	173eV
y0	554.08697	708.66247	594.74562	1.28254E6	594.48066	588.92425
A1	20.81976	-21958.35168	-41.80166	-1.28196E6	-6.36074E8	-33.66642
t1	-129.42151	2.43113	30.26682	6.75285E6	0.91628	29.85541
A2	-194.44701	-145.98548	-23196.96709	-2224.0796	-48.10886	-2.43494
t2	5.59718	321.79612	2.24632	3.50941	29.75378	0.83391

Table 3-3 ROI variation fitting constants for 110eV and 416eVfixed energies

	110eV		416eV	
	ROI0	ROI1	ROI0	ROI1
y0	235.71478	102286.19128	227.51672	583.15497
A1	-8805.55559	-71.00737	-54.17433	-50.29354
t1	2.36264	13.60802	19.37723	22.13653
A2	-37.55035	-101702.58304	-2.66053E6	-1.78166E6
t2	29.63722	1.62011E6	1.37544	1.42581

3.5 The APECS Experiment

Photons of energy 180eV (200eV in case of Cu (100)) were incident on the sample present in the UHV chamber at end station. A high statistics singles spectrum was collected to locate the peaks of valence band (VB), 4p core peak energy and the Auger peaks energy. The RHCMA was focused on 4p core energy at 133eV whereas the LHCMA scanned the low energy tail region from 0 to 70eV including the Auger peak.

3.5.1 The APECS Spectrum

A photon beam of energy 180eV was incident on the sample. The incident beam knocks out $4p_{3/2}$ core electron with binding energy ~43eV, and is emitted at energy 133eV which is detected by RHCMA. The core ionization is followed by an Auger transition in which an atom is stabilized by the electron from valence band filling the core vacancy and transferring its excess energy to the neighboring valence electrons which are emitted and contribute to the Auger peak detected by the LHCMA. The 180eV photon beam knocks out $4p_{3/2}$, N core shell electrons to create a N_3VV Auger transition. In the final state of NVV transition creates two holes in the valence band, or sometimes more than two holes when there is multi Auger decay (NVVV in this case of Ag $4p_{3/2}$). We used the scan CMA (LHCMA) as our start signal for TAC and the fixed CMA (RHCMA) looking at the core was our stop signal. In our earlier APECS measurements the start and stop signal input was in the other way around, in our experiments this interchange was done to reduce the frequency of STOPS in order to minimize the effect of premature accidental STOP and to increase the efficiency of the counting process.

3.5.2 Measuring the Inelastically Scattered VB Photo Electrons

The secondary electron contribution due to the incident beam is greatly reduced using the APECS technique. In the non-coincidence singles spectrum the Auger peak gets obscured by the high intensity at the low energy side of the spectrum. The APECS spectrum enhances the Auger peak by eliminating the secondary electron background; however it cannot eliminate the background arising due to the inelastically scattered valence band photo emitted electrons. The true coincidence arising from inelastically scattered VB also contributes to the low energy part of spectrum and this cannot be eliminated with the APECS technique due to the electron's indistinguishable nature. Some of the photo excited inelastically scattered valence electrons can end up with the same energy as that of the core electrons. The fixed analyzer detects them as core electrons and this factor which is Auger unrelated also contributes in the coincidence spectrum. To explain in other words, the photon beam incident on the sample excites the core electrons as well the other energy level electrons, mainly valence band electrons, and if any of the other energy level or valence band electrons are emitted out of the sample with the energy equal to the fixed CMA energy, it is recorded as a stop signal. The remaining energy of the incident beam is shared (Es) with other valence electrons which are low energetic and are detected by the scanning CMA. This Auger unrelated contribution arising in the APECS spectrum affects the accuracy of the quantitative analysis of the Auger line shape. The inelastically scattered VB background contribution arises from electrons in the region in between core and the valence band. The VB peak has contributions of inelastically scattered valence electrons which is extended all the way down till 0eV. The core peak is also situated on top of this contribution (figure). From the figure we can visualize the inelastically scattered valence band and core electrons contribute to the low energy tail. The LET of Ag(100) has significant Auger unrelated contribution, in order to estimate this secondary electrons contributions for the inelastically scattered of the valence band(VB) photoelectron, we have used the VB-VB coincidence instead of the core [2,9,10].

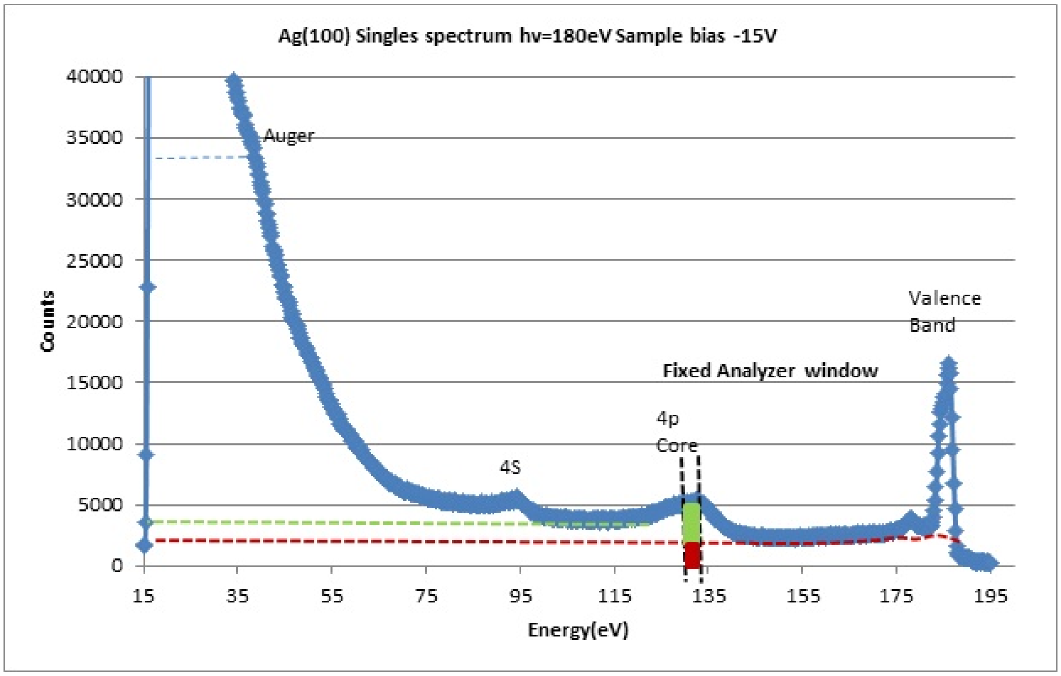

Figure 3-5 Ag(100) Photoelectron spectrum, the red column shows the inelastically scattered VB photoelectrons detected along with 4p core

We did a series of background coincidence measurements with the fixed energy in between core and the valence band. We observed that the contribution to the LET increased as the difference between the core and the valence band energy increased, five fixed analyzer energies were chosen in between valence band and the core in steps of 7eV, the energies for VB coincidence measurements were 145eV, 152eV, 159eV, 166eV, 173eV, with -15V sample bias. We also took low energy spectra in coincidence with the Fermi level and observed no contribution towards the LET, this tested our assumption of increasing contribution as we move away from valence band.

Let us understand the energy sharing mechanism in the valence band inelastic scattering process, when a photon beam of energy hv=180eV is incident on the sample (the sample with bias of 15V sees the beam as 195eV). If the fixed analyzer is at 145eV, we can imagine that the analyzer takes up or detects the electrons with 145eV. The remaining (180-145) 35eV energy minus the work function is available among valence band electrons for sharing. After absorbing this available energy the low energy electrons are emitted out contributing to the LET and detected by the scanning CMA [2].

We refer to KE_1 as the kinetic energy of electron detected by the “fixed” analyzer (RHCMA) and KE_2 as the energy of the electron detected by the scanned analyzer (LHCMA). If an electron detected in the fixed analyzer at energy KE_1 is below the energy of the VB photoemission peak, then it must have shared an amount of energy, ΔE, given by equation 3.7.

$$\Delta E = hv - E_{v1} - \phi_A - KE_1, \qquad (3.7)$$

where KE_1 represents the energy of the detected photo-emitted valence band electron, hv is the energy of the incident photon, E_{v1} is the binding energy of the outgoing electron referenced to the top of the Fermi level, ϕ_A is the work function of the analyzer. If we assume that the energy, ΔE, is shared with 1 or more additional VB electrons then energy conservation considerations result in an upper limit given by eq. 3.8 for the energy KE_2 of another VB electron detected in coincidence.

$$KE_2 \leq \Delta E - E_{v2} - \phi_A, \qquad (3.8)$$

where, E_{v2} is the binding energy of the detected electron. The equality holds for the case of a two-electron process in which all of the energy of the initial photon is shared between the two electrons (either as a result of some direct multi-electron process or through an inelastic collision of the second electron as it exits the surface). The less than relation would apply to multi-electron or energy loss processes in which the energy is shared by more than one additional electron.

Table 3.4 lists the energies of the fixed analyzer used in the coincidence measurements shown in Fig. 3.6, and the estimated cut off energy KE_{2max}. The value of KE_{2max} was calculated using an expression given by equation 3.9,

$$KE_{2max} = KE_{VB-Peak} - KE_1 - \phi_A, \qquad (3.9)$$

that can be justified by substituting equation 3.7 into equation 3.8 and noting that the energy of the VB peak is given by:

$$KE_{VB-Peak} = hv - \overline{E_{v1}} - \phi_A, \qquad (3.10)$$

where $\overline{\boldsymbol{E_{v1}}}$ is close to the peak in the VB density of states.

Table 3-4 Energy shared and cutoff energy for different fixed energies in Ag(100)

Fixed Analyzer Energies	ΔE (eV)	KE2 max
133eV	48.5	≤ 48.5
145eV	36.5	≤ 36.5
152eV	29.5	≤ 29.5
159eV	22.5	≤ 22.5
166eV	15.5	≤ 15.5
173eV	8.5	≤ 8.5
186eV	0	0

The spectrum shown in figure 3.6 is the non coincidence (singles) spectrum of Ag(100) with sample bias -15V,

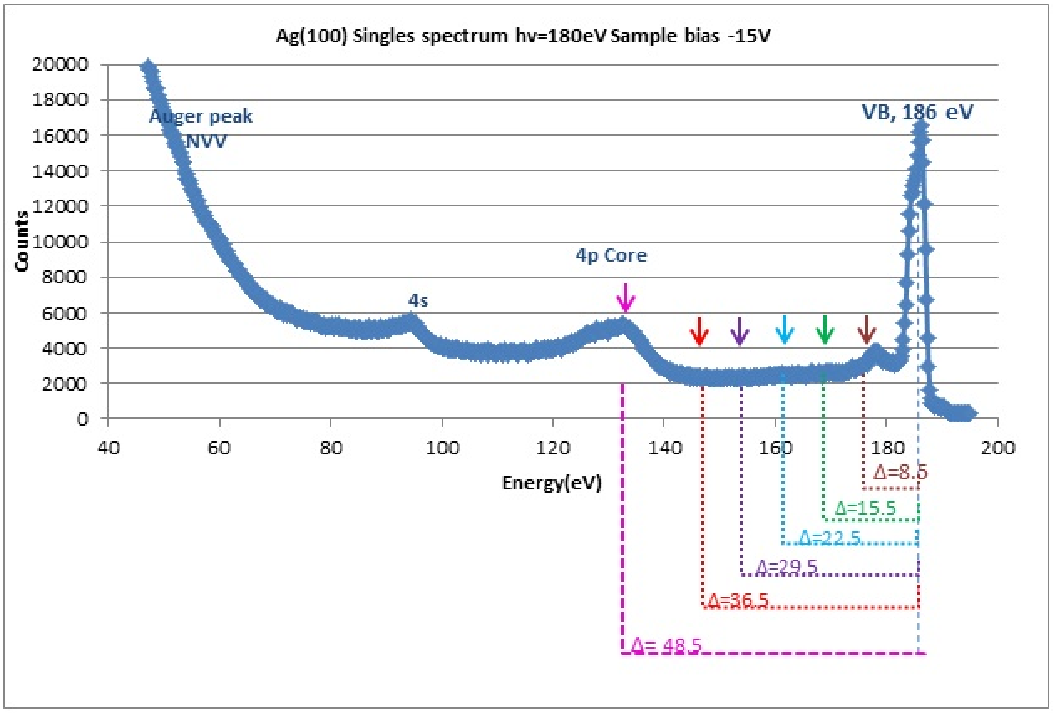

Figure 3-6 Ag(100) Photoelectron spectrum with fixed analyzer positions and values of energy shared indicated

3.6 True Coincidence Data Correction

In our APECS measurements the true counts were counted as the difference between coincidence and the accidental events. The time to amplitude (TAC) converter operational efficiency is affected by the intensity of start and stop signals, thereby affecting coincidental and accidental counts. In our data extraction process we consider the effect of primitive accidental STOP due to high STOP rate.

Let us define TAC efficiency,

$$\varepsilon\ (t) = \frac{No(\#).of\ times\ TAC\ \ is\ started\ and\ NOT\ stopped\ by\ t{=}t1}{No.(\#)of\ time\ TAC\ is\ started}\ , \qquad (3.11)$$

As the TAC is either stopped or NOT stopped, we can write,

$$1 = \frac{\#\ of\ times\ TAC\ is\ started\ and\ NOT\ stopped\ by\ t1}{\#\ of\ time\ TAC\ is\ started} +$$

$$\frac{\#\ of\ times\ TAC\ is\ started\ and\ is\ stoped\ by\ time\ t1}{\#\ of\ times\ TAC\ is\ started}, \tag{3.12}$$

Substituting from equation (3.11)

$$1 = \varepsilon(t1) + \frac{\#\ of\ times\ TAC\ is\ started\ and\ is\ stoped\ by\ time\ t1}{\#\ of\ times\ TAC\ is\ started}, \tag{3.13}$$

Rearranging,

$$\varepsilon(t1) = 1 - \frac{\#\ of\ times\ TAC\ is\ started\ and\ is\ stoped\ by\ time\ t1}{\#\ of\ times\ TAC\ is\ started}, \tag{3.14}$$

$$\varepsilon(t1) = 1 - \frac{\#\ of\ counts\ (0<t<t1)}{(\#\ of\ {}^{starts}/_{\mathrm{sec}})(\ live\ time)},$$

$$\varepsilon(t1) = 1 - \frac{\#\ of\ counts\ (0<t<t1)}{(\#\ of\ fixed\ counts)(\frac{livetime}{Realtime})}, \tag{3.15}$$

We calculated true counts as difference of Coincidental and Accidental counts,

Trues= ROI(0)-ROI(1),

Applying the correction to obtain correct trues,

$$T = \frac{ROI(0)}{\varepsilon(t0)} - \frac{ROI(1)}{\varepsilon(t1)}, \tag{3.16}$$

Here t0 is the TAC stopping time for ROI(0) and t1 is the stopping time for ROI(1). The number of counts for (0<t<t1), the number of fixed counts and the live time, MCA timing spectra is measured in the energy range 0 to 70eV in steps of 1eV.

3.7 Error Analysis

The equation 3.5 is used to calculate the true coincidence counts as the difference of coincidental events minus the accidental events which is similar to equation

x=au+bv, (3.17)

For equation (3.16) the error is determined using $\sigma_x^2=a^2\sigma_u^2+b^2\sigma_v^2+2ab\sigma_{uv}^2$ [29]

To calculate error in true counts- We have equation,

$$Trues = \frac{Coins}{e0} - \frac{Acci}{e1}, \tag{3.18}$$

Where eo is Coins TAC efficiency; e1 is Acci TAC efficiency, comparing equation (3.17) with (3.18),

We have, x=Trues; a= $\frac{1}{e0}$; b= $\frac{-1}{e1}$; u= Coins ; v= Acci; The covariance between Coins and Acci is negligible hence σ_{uv}^2 =0.Thus for our case, $\sigma_x^2=a^2\sigma_u^2+b^2\sigma_v^2$,

Error in Coins, σ_u =$\sqrt{Coins}$; Error in Acci, σ_v =$\sqrt{Acci}$

$$\sigma_x{}^2 = \frac{Coins}{e0^2} + \frac{Acci}{e1^2}, \tag{3.19}$$

$$\sigma_{Trues} = \sqrt{\frac{Coins}{e0^2} + \frac{Acci}{e1^2}}, \tag{3.20}$$

In our error bar calculation, error was normalized to the total singles.

Chapter 4

APECS Data and Analysis

4.1 Ag(100) Photoelectron spectra

A wide range scan data was acquired using the scanning CMA to obtain the non-coincidence singles spectrum (figure 4.1). While acquiring singles spectrum we used a large aperture with the energy resolution of 1.6% of the pass energy to facilitate a higher count rate. The singles spectra helped us located the important core, Auger and valence band peaks.

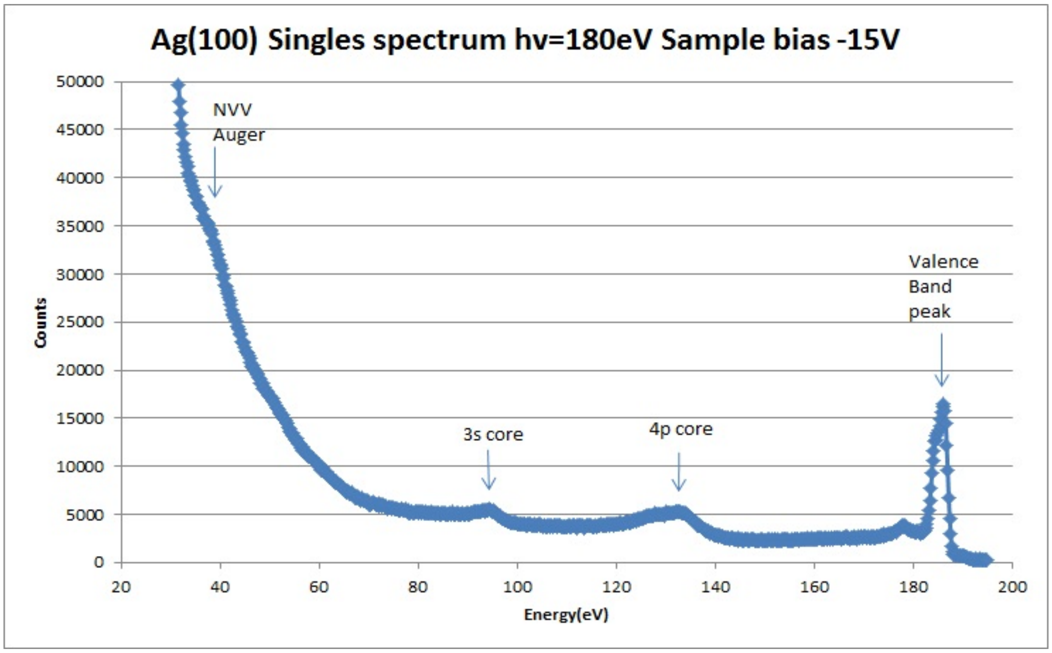

Figure 4-1 Ag(100) Singles spectrum with incident photon beam energy of 180eV with a sample bias -15V

4.2 Ag(100) NVV APECS Auger Spectrum

For coincidence measurements, we focused our fixed CMA (RHCMA) at the Ag 4p core at 133eV with the incident photon beam of 180eV. The scan CMA (LHCMA) scanned to low energy range (0-70eV) including the Auger region. The figure shows the spectrum of true and corrected trues. The correction to the true counts was done once after correcting the coincidental and the accidental by their respective efficiencies and then taking their difference (section 3.5.3).

4.2.1 Comparing APECS Spectrum with the Photoelectron Spectrum

The photoelectron spectrum is the non-coincidence spectrum, and has the spectral contributions arising from all the electronic transitions including secondary electrons emitted from the sample surface. We can see the huge intensity at the low energy part of the spectrum, which obscures the important peak of interest. APECS greatly reduces the contribution from the secondary electrons. Comparing figure 4.1 with figure 4.2, we can observe the intensity of the LET has reduced and Auger peak has become the prominent photoelectron spectrum.

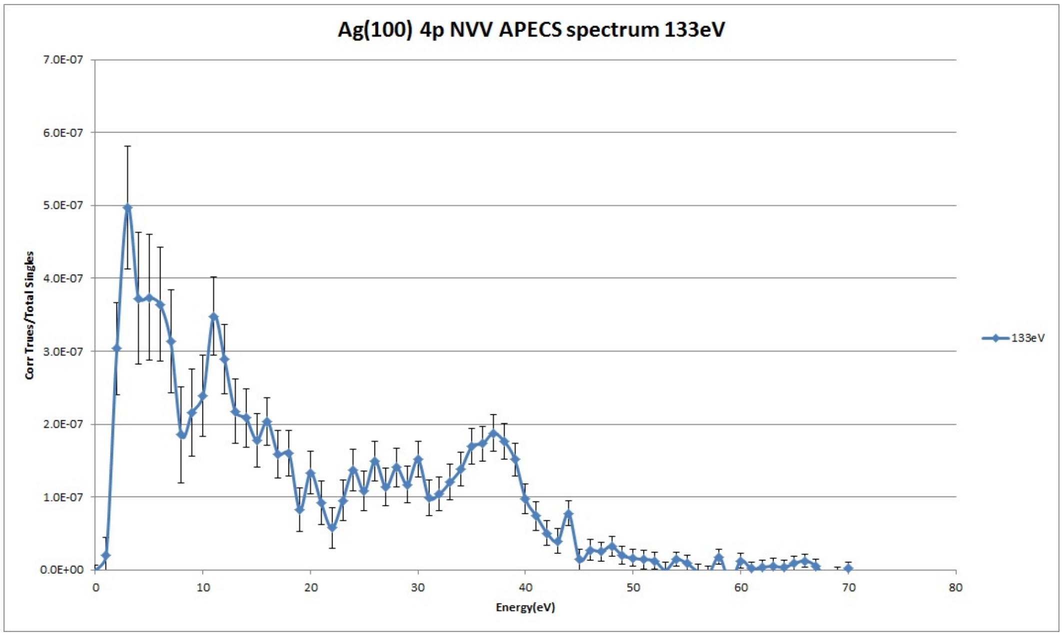

Figure 4-2 Ag(100) 4p NVV APECS spectrum, fixed analyzer energy 133eV

4.3 Auger Unrelated Contributions in the Low Energy Tail (LET)

The huge intensity associated with the Auger peak can be attributed to two factors, one Auger related and other Auger unrelated [1, 30]. The Auger related contributions arise from Auger transition, multi Auger decay and inelastically scattered Auger electrons. The Auger unrelated contribution arises from the primary beam and the inelastic scattering of the valence band electrons. Although the coincidence technique of the APECS makes the low energy tail of the APECS spectrum free of the beam induced secondary electron contributions, there are still contributions arising from false coincidence events. The primary contributors to the APECS LET are the inelastically scattered valence band electrons which are unrelated to the Auger transitions. In our experimental measurements we measured and estimated the inelastically scattered valence band contribution to the low energy tail.

When a photon beam of energy hv is incident on the sample, it can create a valence photoelectron which gets emitted at the pass energy of the fixed analyzer looking at the core (133eV). The remaining energy of photon beam, ΔE eV is transferred or shared with the neighboring valence band electrons. Following the energy conservation principle, the energy shared, ΔE [2], can be calculated by equation 3.7 [$\Delta E = hv - E_{v1} - \phi_A - KE_1$] and the energy of the electrons emitted out in the vacuum with the maximum energy KE_2 by equation 3.9 [$KE_{2max} = KE_{VB-Peak} - KE_1 - \phi_A$].

4.3.1 VB-VB Coincidence Measurements of the Inelastically Scattered Electrons at 145eV

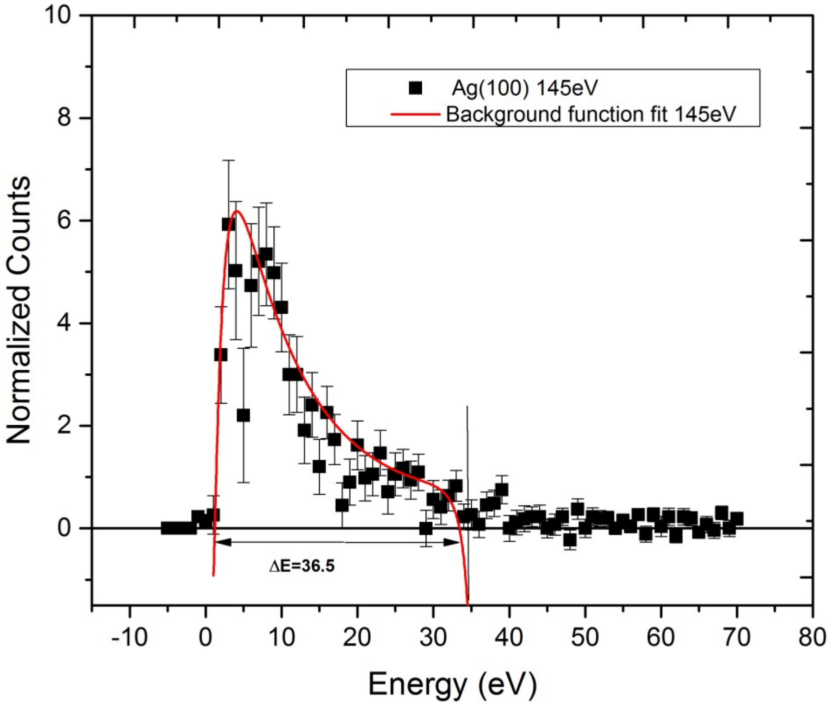

Figure 4-3 Ag(100) VB Coincidence spectrum for fixed analyzer energy at 145eV.

The fixed analyzer (RHCMA) was set at 145eV and the scanned CMA scanned the energy range from 0-70eV. The figure 4.3 shows the Auger unrelated spectrum arising from the coincidence with respect to the valence band photoelectron of energy 145eV for the incident photon beam of 180eV. The energy shared is given by the equation (3.7) ΔE = 186-145-ϕ=36.5eV. The energy value is the energy shared by the valence band electrons which contributes to the low energy region from 0-37eV as shown in table 3.4. The VB-VB coincidence data was extracted using Matlab code (Appendix C) written to find the coincidental and the accidental events from the raw data. The corrected trues are the difference of the coincidental and the accidental counts after their correction with respective efficiency. This procedure was followed for all the fixed analyzer energies.

4.3.2 VB-VB Coincidence Measurements of the Inelastically Scattered Electrons at 152eV

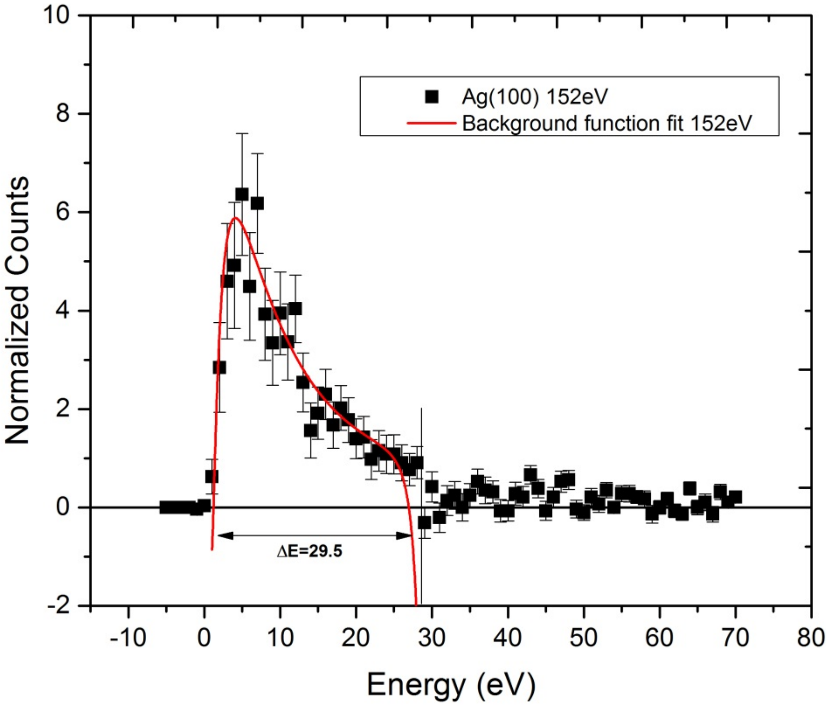

Figure 4-4 Ag(100) VB coincidence spectrum for fixed analyzer energy at 152eV

The fixed analyzer (RHCMA) was set at 152eV and the scan CMA scanned the energy range from 0-70eV. The figure 4.4 shows the Auger unrelated spectrum arising from the coincidence with respect to the valence band photoelectron of energy 152eV for the incident photon beam of 180eV. The energy shared given by the equation (3.7) and shown in table 3.4, ΔE = 186-152-ϕ=29.5 eV.

4.3.3 VB-VB Coincidence Measurements of the Inelastically Scattered Electrons at 159eV

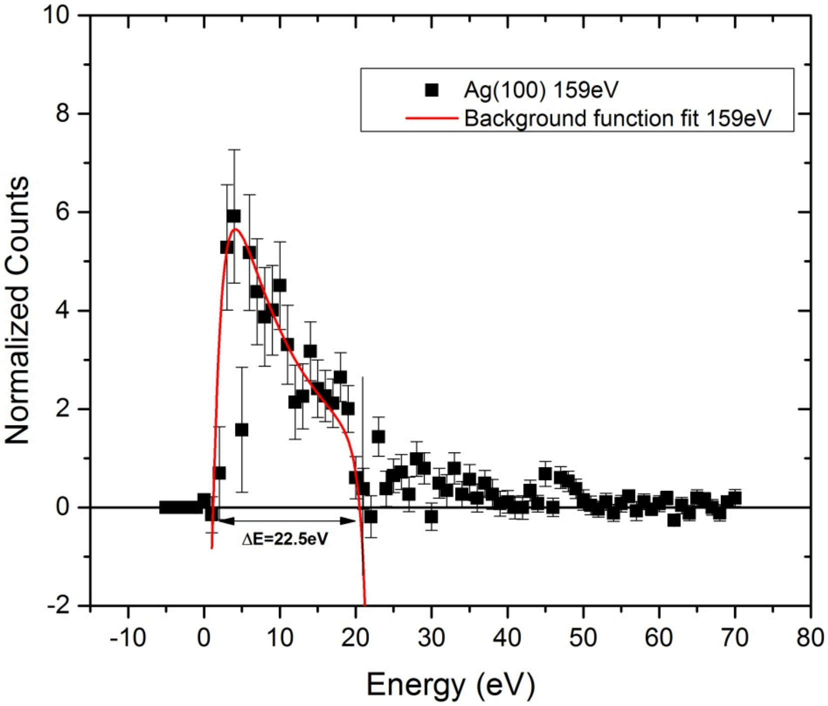

Figure 4-5 Ag(100) VB coincidence spectrum for fixed analyzer energy at 159eV

The fixed analyzer (RHCMA) was set at 159eV and the scan CMA scanned the energy range from 0-23eV. The figure shows the Auger unrelated spectrum arising from the coincidence with respect to the valence band photoelectron of energy 159eV for the incident photon beam of 180eV. The energy shared given by the equation (3.7) and shown in table 3.4, ΔE= 186-159-ϕ=22.5 eV.

4.3.4 VB-VB Coincidence Measurements of the Inelastically Scattered Electrons at 166eV

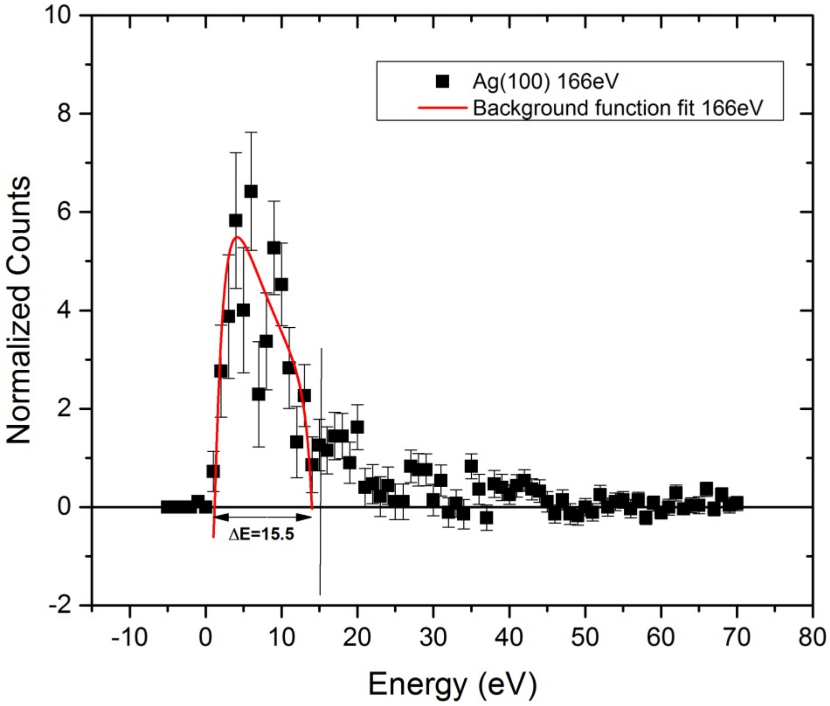

Figure 4-6 Ag(100) VB coincidence spectrum for fixed analyzer energy at 166eV

The fixed analyzer (RHCMA) was set at 166eV and the scan CMA scanned the energy range from 0-70eV. The figure shows the Auger unrelated spectrum arising from the coincidence with respect to the valence band photoelectron of energy 166eV for the incident photon beam of 180eV. The energy shared given by the equation (3.7) and shown in table 3.4, ΔE= 186-166-ϕ=15.5 eV.

4.3.5 VB-VB Coincidence Measurements of the Inelastically Scattered Electrons at 173eV

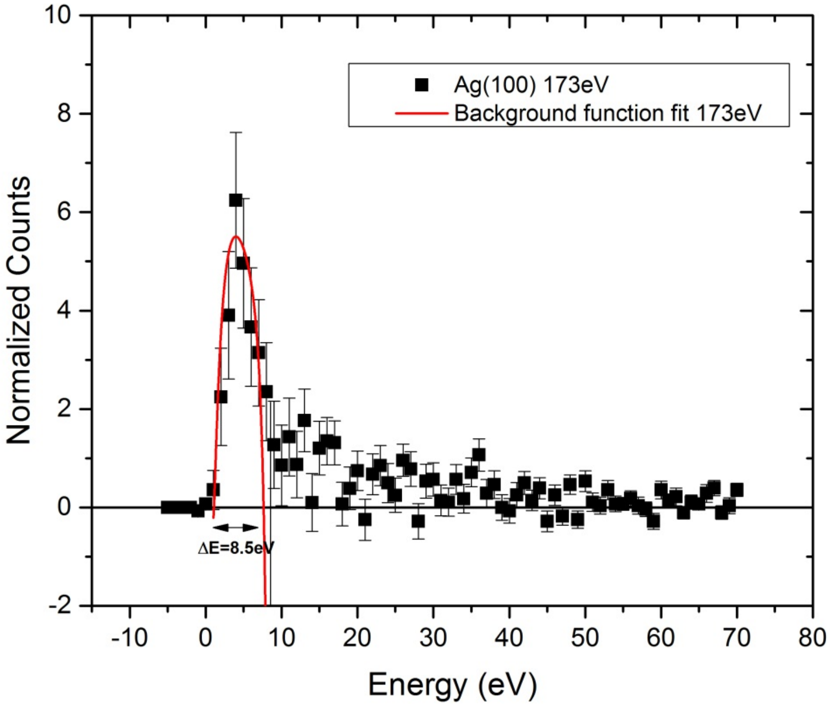

Figure 4-7 Ag(100) VB coincidence spectrum for fixed analyzer energy at 173eV

The fixed analyzer (RHCMA) was set at 173eV and the scan CMA scanned the energy range from 0-70eV. The figure shows the Auger unrelated spectrum arising from the coincidence with respect to the valence band photoelectron of energy 173eV for the incident photon beam of 180eV. The energy shared given by the equation (3.7) and shown in table 3.4, ΔE-ϕ= 186-173-ϕ=8.5 eV.

4.3.6 VB-VB Coincidence Measurements of the Inelastically Scattered Electrons Near Valence Band- 182eV, 186eV, 188.6eV

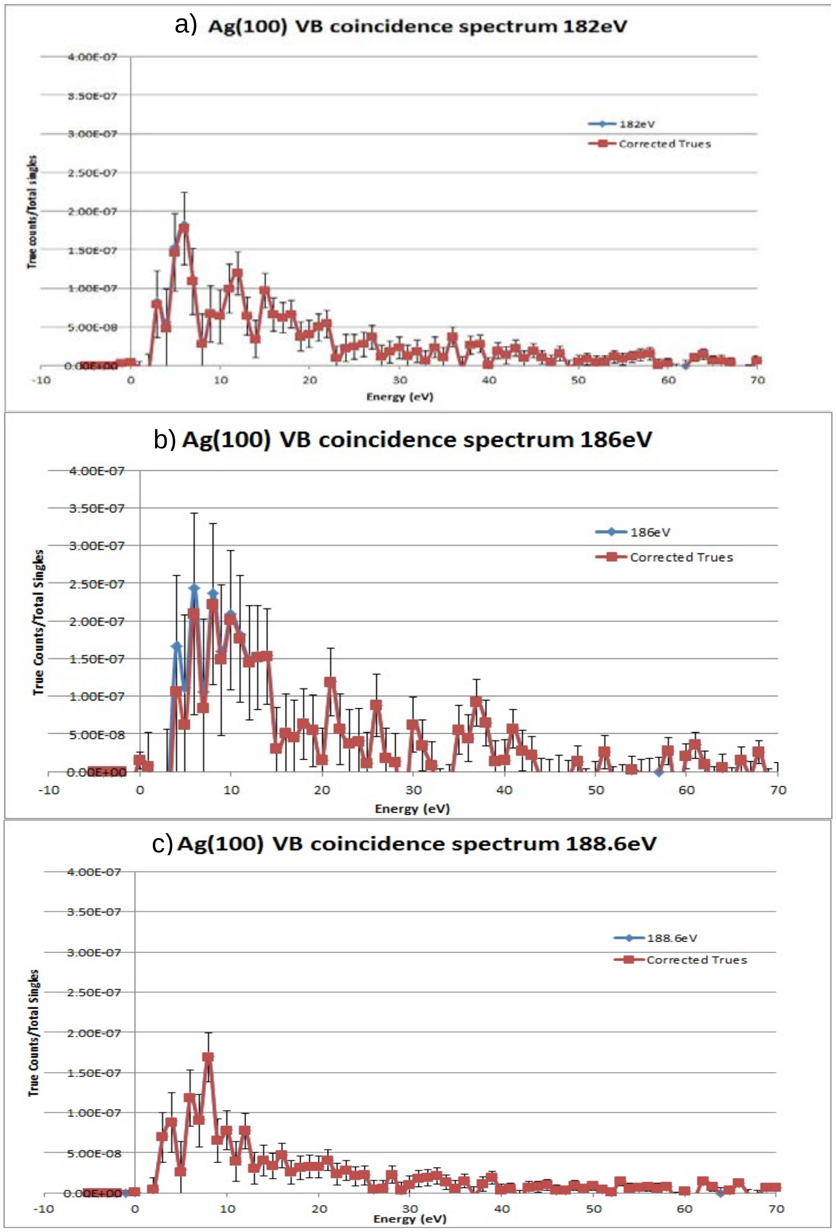

Figure 4-8 Ag(100) VB coincidence spectrum for fixed analyzer energy at (a) 182eV, (b) 186eV and (c)188.6eV

The fixed analyzer (RHCMA) was set at 182eV (before valence band peak), 186eV (on the valence band peak) and 188.6eV (falling edge of the valence band peak) and the scan CMA scanned the energy range from 0-70eV.

4.4 Curve Fitting and Data Extrapolation Using Ramaker Function

There has been considerable theoretical work to extract Auger line shape and removing background from XPS and AES spectrums using numerical methods [13,33]. Ramaker et al developed a background subtraction method by numerically integrating the derivative spectrum of their experimental data [31-33]. For S and P LVV spectrum obtained from the samples of Li salts of SO_4^{2-}, PO_4^{3-}, they used least-square fitting of an appropriate function to the desired range in the Auger spectrum.

The Ramaker background function is described below by the equation

$$B(E) = \frac{A(E)}{(E+E_0)(E+\emptyset)^m} + \frac{B\, ln[(E_p-E)/E_b]}{[(E_p-E)/E_b\,]^n} + C\,, \qquad (4.1)$$

The background function is based on descriptions of the true secondary electrons by Seah and the redistributed primary electrons by Inokuti.

Here the constants A, B, and C are determined by least square fit of the observed inelastic coincidence background. The exponential constants m and n, calculated by Seah and Ramaker are taken as 2 and 1.8 respectively for Ag and m= 1.6 and n= 2 for Cu sample. Other variables in the equation can be described as follows:

E = Energy of the secondary electron with respect to vacuum level

E_p = Primary beam energy (**Δ** eV)

E_b = Binding energy of the primary electron

E_0 = Energy constant determined based on an optimal least sq. fit to the observed data.

The value of Δ can be found from; $\Delta = h\nu - E_{Fixed} - E_B - \phi_A$

In the valence band photoemission process of Ag (100) and Cu (100), when the photon beam knocks out a valence electron which is inelastically scattered on its way out of the sample whilst transferring energy **Δ**E eV to the neighboring electrons. This induces other valence electrons to be knocked out of the sample with lower energy and they end up contributing to the low energy part of the Auger spectrum. The LET background consists of both the electrons from the primary beam and the true secondary electrons from the sample. The primary beam electrons are inelastically scattered valence band photoelectrons and the ones which are emitted after accepting the entire primary beam energy ΔE eV. The true secondary electrons are the ones which are emitted after mutually sharing the primary beam energy or emerging with inelastically accepting transferred energy, thus the secondary electrons emerge out with a range of energy from 0 to ΔE eV.

We measured the Low energy tail plots by electron-electron coincidence; we measured the contribution from the inelastically scattered valence band photoelectron by keeping the fixed analyzer in the energy range between the core(133eV) and the valence band(186eV), and the fixed analyzer was kept at 145eV, 152eV,159eV,166eV and 172eV for Ag(100). These non-APECS LET spectra were measured to observe a trend with respect to fixed energy. The Ramaker like equation was used to fit the data

$$B(E) = \frac{A(E-1)^{1.4}}{((E-1)+D)(E+\emptyset)^{m}} + \frac{B\ ln[(E_p-(E-1))/E_b]}{[(E_p-(E-1))/E_b\,]^{n}} + C\ , \tag{4.2}$$

The A, B, C, and D constants were determined using a non-linear curve fit of the above equation to the data and are obtained using OriginPro 9.1 version software. The Ramakar equation is optimally fitted to the all the LET observed with respect to all of the fixed energies. On the basis of the values for different fixed energies, the constants A, B, C and D are extrapolated to estimate the LET curve for the core level energy.

To account for low energy Plasmon peak in the VB-VB coincidence spectrum we introduced a Gaussian term to equation 4.2,

$$B(E) = \frac{A(E-1)^{1.4}}{((E-1)+D)(E+\emptyset)^{m}} + \frac{B\ ln\left[(E_p-(E-1))/E_b\right]}{[(E_p-(E-1))/E_b\ ]^{n}} + C + He^{\frac{-(x-F)^2}{2G^2}}, \qquad (4.3)$$

The constants H,G, F are determined with non-linear data fit, H is the amplitude-height of the Gaussian peak, F is the center of the peak and G is the width of the peak. The equation 4.3, background fit function was used in our data analysis.

4.5 The Background Function Fit on the Data

4.5.1 Curve Fit For Fixed Analyzer Energy 145eV

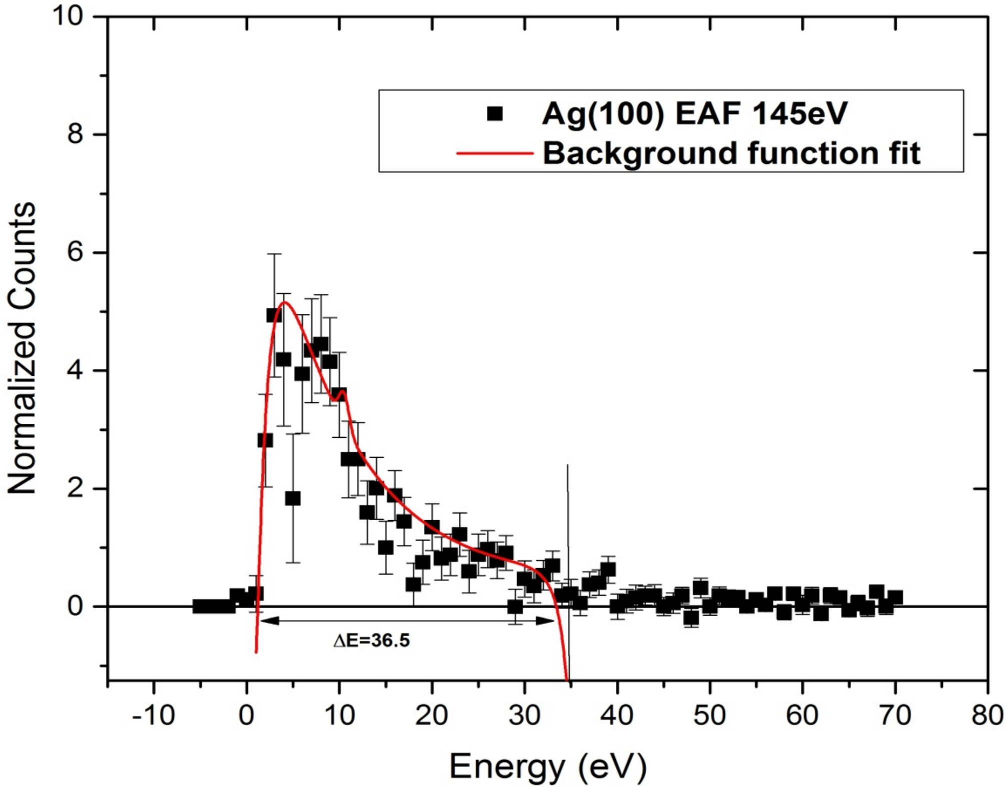

Figure 4-9 Ag(100) VB coincidence spectrum, data fitted with background function fit showing the Auger unrelated contribution in the low energy region when fixed analyzer is set at 145eV.

The distribution of the energy shared ΔE between the valence electrons can be seen from energy range 0 to 36.5eV. The background function, B(E), is used to fit the data using Origin 9.1. The respective parameters were recorded and used in extrapolation.

4.5.2 Curve Fit for Fixed Analyzer Energy 152eV

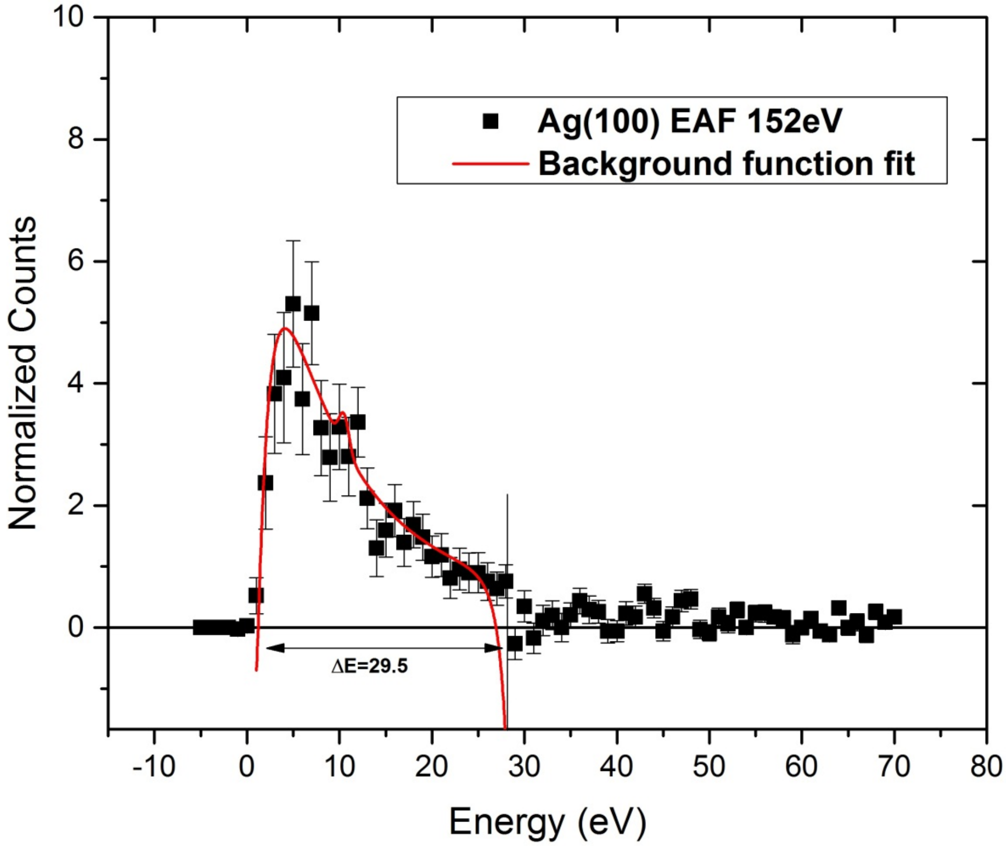

Figure 4-10 Ag(100) VB coincidence spectrum, data fitted with background function fit showing the Auger unrelated contribution in the low energy region when fixed analyzer is set at 152eV.

The distribution of the energy shared ΔE between the valence electrons can be seen from energy range 0 to 29.5eV. The background function, B(E), is used to fit the data using Origin 9.1. The respective parameters were recorded and used in extrapolation.

4.5.3 Curve Fit for Fixed Analyzer Energy 159eV

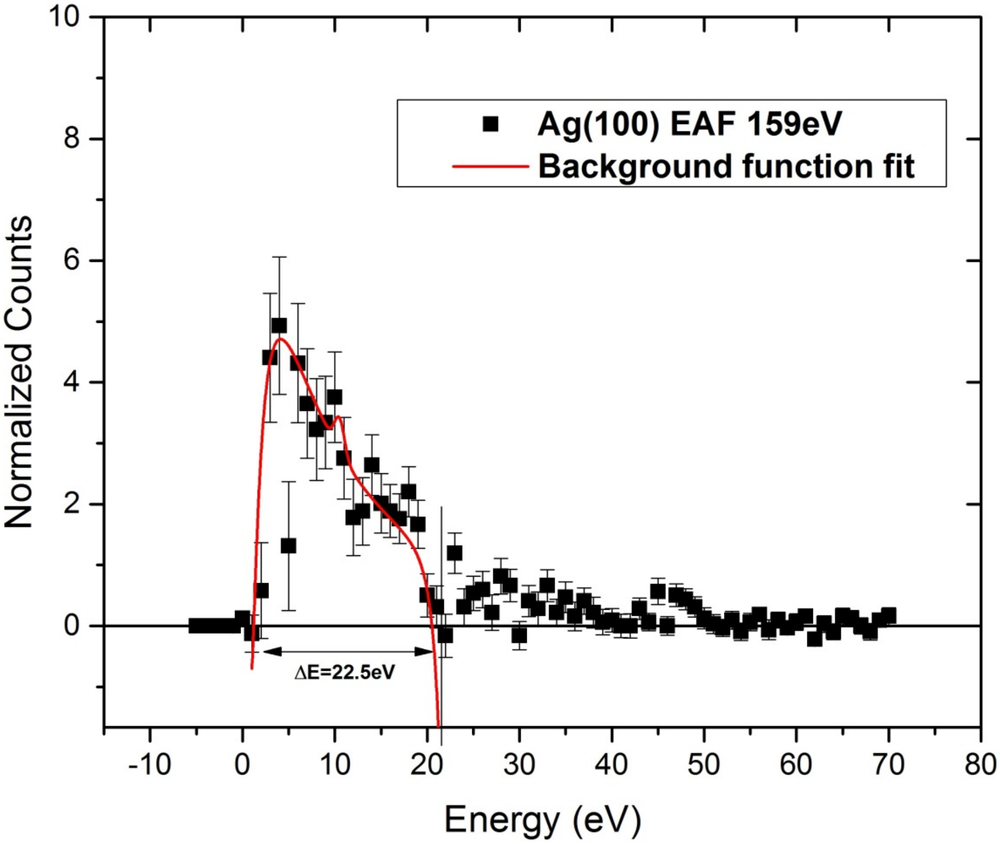

Figure 4-11 Ag(100) VB coincidence spectrum, data fitted with background function fit showing the Auger unrelated contribution in the low energy region when fixed analyzer is set at 159eV.

The distribution of the energy shared ΔE between the valence electrons can be seen from energy range 0 to 21.5eV. The background function, B(E), is used to fit the data using Origin 9.1. The respective parameters were recorded and used in extrapolation.

4.5.4 Curve Fit for Fixed Analyzer Energy 166eV

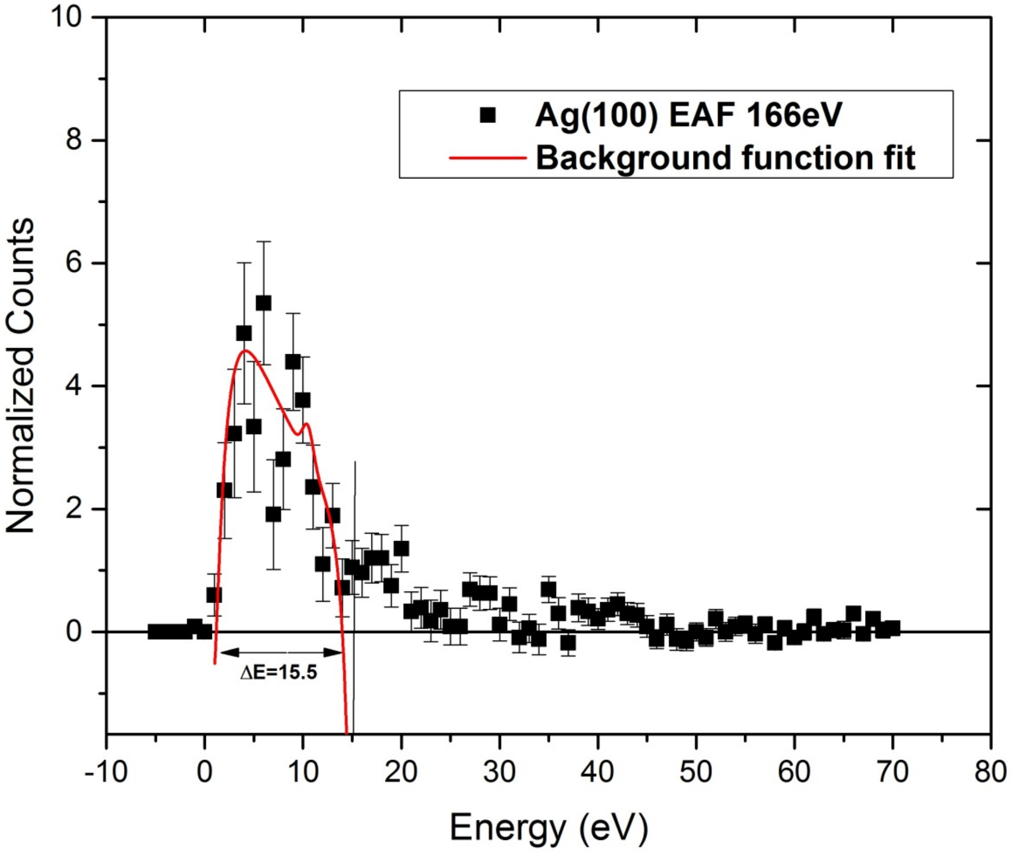

Figure 4-12 Ag(100) VB coincidence spectrum, data fitted with background function fit showing the Auger unrelated contribution in the low energy region when fixed analyzer is set at 166eV.

The distribution of the energy shared ΔE between the valence electrons can be seen from energy range 0 to 15.5eV. The background function, B(E), is used to fit the data using Origin 9.1. The respective parameters were recorded and used in extrapolation.

4.5.5 Curve Fit for Fixed Analyzer Energy 173eV

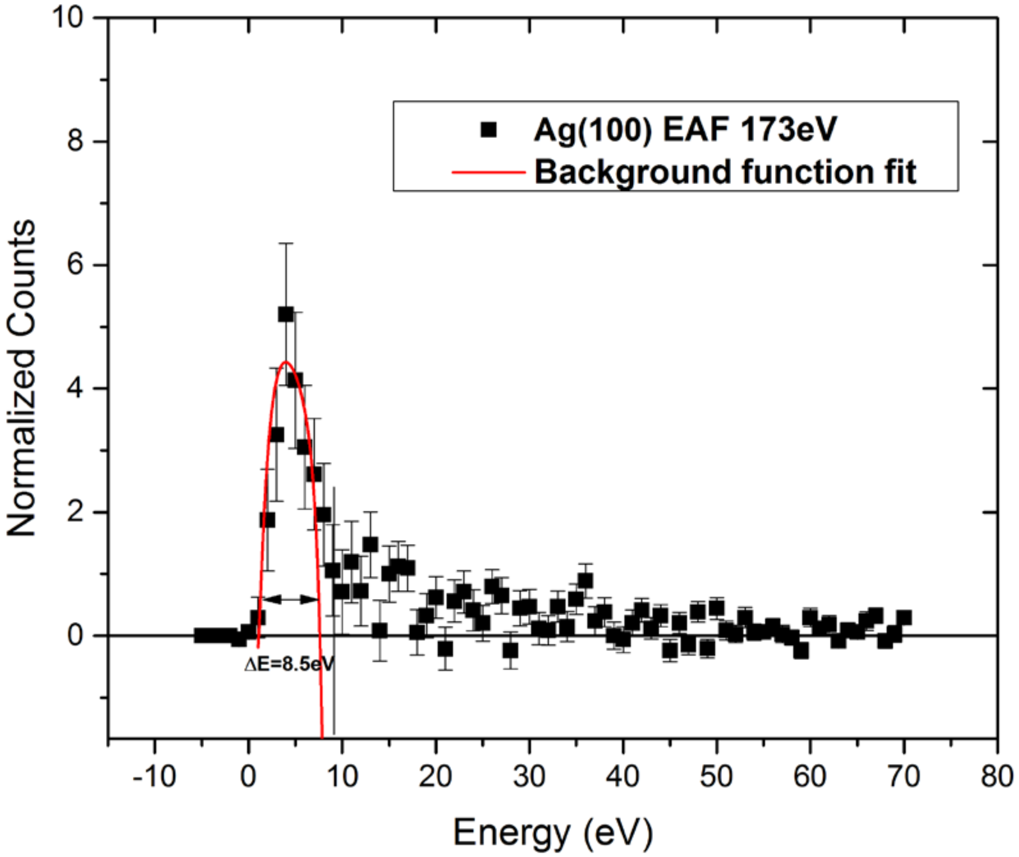

Figure 4-13 Ag(100) VB coincidence spectrum, data fitted with background function fit showing the Auger unrelated contribution in the low energy region when fixed analyzer is set at 173eV.

The distribution of the energy shared ΔE between the valence electrons can be seen from energy range 0 to 8.5eV. The background function, B(E), is used to fit the data using Origin 9.1. The respective parameters were recorded and used in extrapolation.

4.6 Estimation of the Auger Unrelated Contribution in the Ag(100) 4p NVV APECS Spectrum

From the background function fit of our data, we extracted the parameters-constants for all the fixed energies and extrapolated it for 133eV- 4p core fixed analyzer energy.

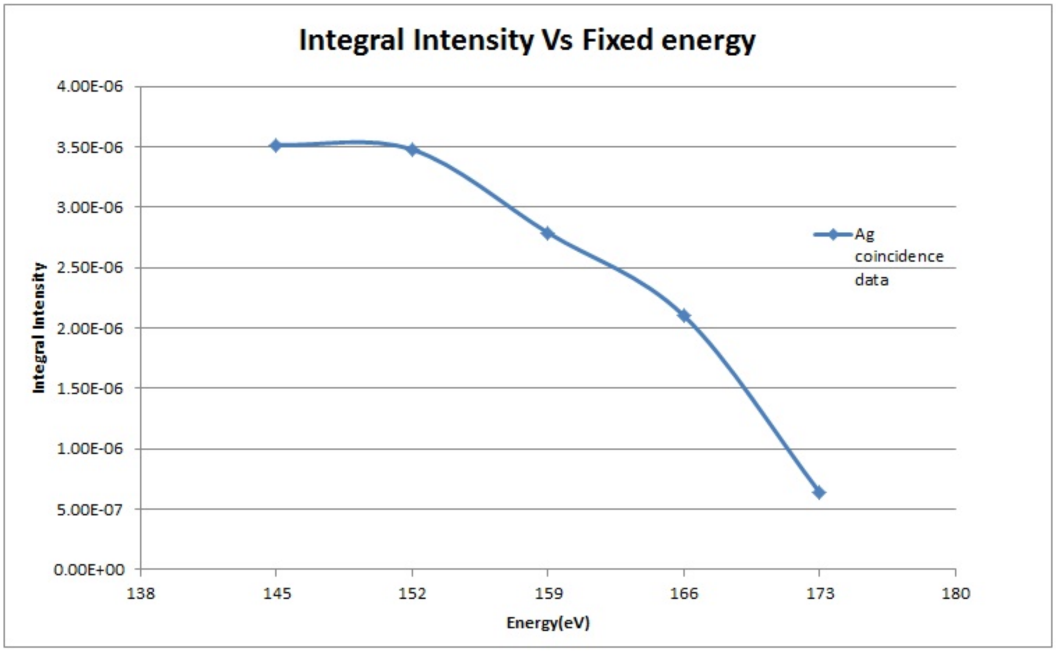

Figure 4-14 Integrated Intensity area variation with respect to fixed energy

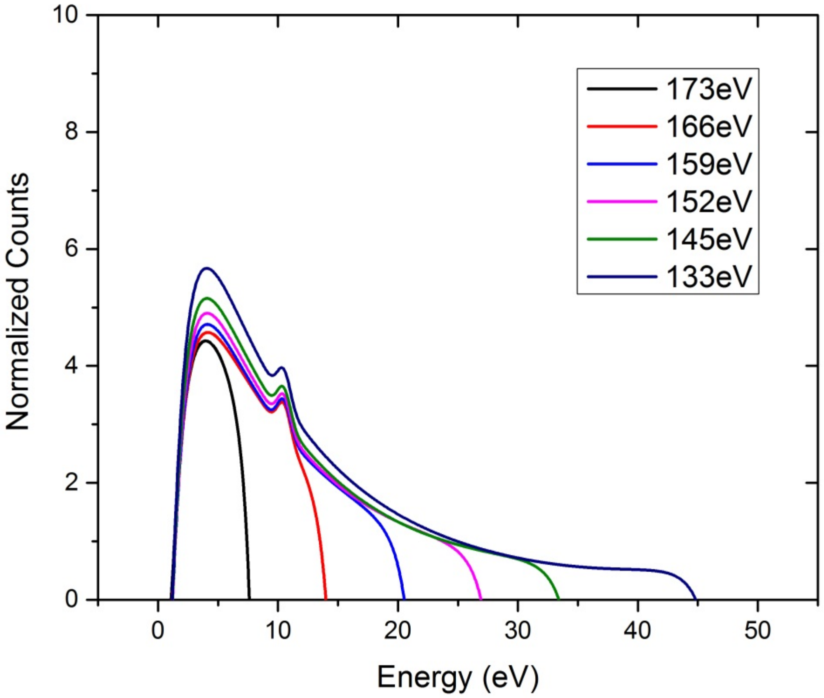

Figure 4-15 The extrapolation of the Auger unrelated contribution on different kinetic energies. The topmost curve is the estimated contribution at 4p core

The figure 4.14 shows the integrated intensity variation with respect to the fixed analyzer energy. The curve figure 4.15 represents the contribution unrelated to the Auger transition, this secondary electron contribution arises from the inelastically scattered VB electrons. In the spectrum, to account for negative 15V sample bias the data is shifted by 15eV to the left of x-axis.

From the curves we can observe that the contribution of the secondary electrons generated by the inelastically scattering of the valence band electrons increases as the Es energy shared by the valence band electrons increases. As expected, when the fixed analyzer is set closer to 4p energy range, that is 133eV, there is more energy available to share by VB electrons and more electrons are emitted with the low energy.

A trend may be seen with the background (VB-VB) coincidence measurements of the VB-VB high fixed energy curves moves one below another, and after a point they drop to zero following the conservation of energy equation [hv-(fixed energy)-Ev1- ϕA]. The photon energy is 180eV plus sample bias -15V resulting in a beam of hv=195eV.

The spectrum taken near valence band 182, 186, 188.6eV, (figure 4.8) shows a little contribution and doesn’t show threshold or cutoff, which is an exception to the above mentioned trend. The possible reason is as we apply sample bias of 15V the threshold is below the bias energy. Another reason could be as the VB band peak is 5 times higher with respect to the low energy tail. It is expected that the VB true coincidences should be ~5 times higher than LET true coincidence as true coincidence count rate is the cumulative probability of electron detection of the fixed analyzer and scanned analyzer by a causal photon. As expected the other coincidence count rate of fixed energies with LET are nearly the same.

In the figure below the red curve represents the extrapolated curve, which is the estimated contribution from inelastically scattered valence band electron which are Auger unrelated and causes false coincidences.

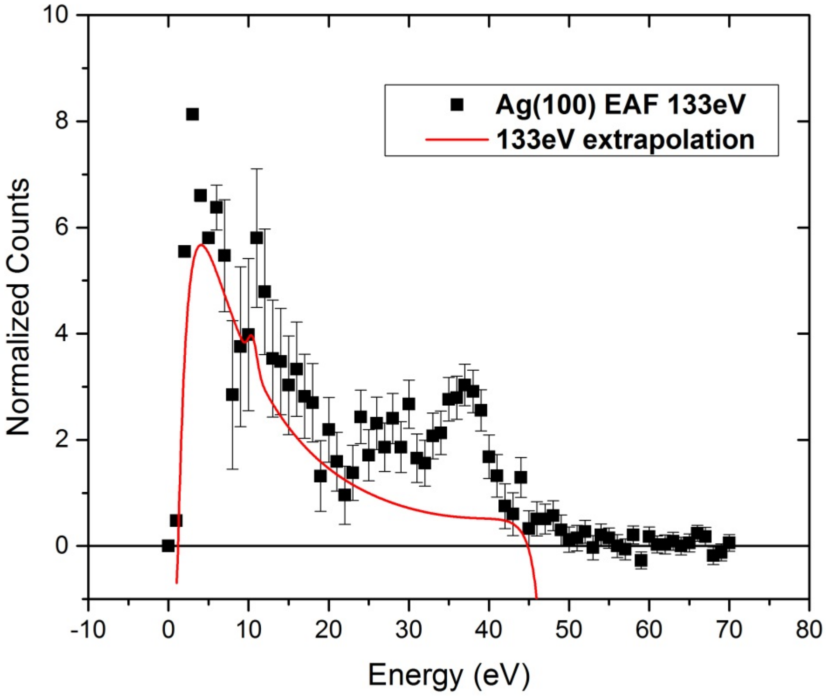

Figure 4-16 Red curve shows the estimated contribution from the inelastically scattered valence band

The red curve in the spectrum shows the Auger unrelated inelastically scattered valence band electron contribution arising in the low energy region of the Auger APECS spectrum. There is high absorption coefficient in Ag and Cu at 10 eV to create surface and bulk plasmons [34]. The peak seen around 30 eV are due to the Plasmon loss peak and the peak seen at around 11eV is due to the Plasmon gain peak. The inelastically scattered Auger electrons give off its energy while coming to continuum may generate surface and bulk Plasmon (the peak observed at 30eV). The Plasmon generated can decay by producing low energy secondary electrons, the low energy peak observed at 11eV [35-39]. The Plasmon peaks were observed similarly in the spectrum of Copper.

4.7 Elimination of the Auger Unrelated Contribution from the spectrum

We subtract the estimated curve from the NVV Auger spectrum to eliminate the Auger unrelated contribution. The spectrum obtained is solely related to the Auger.

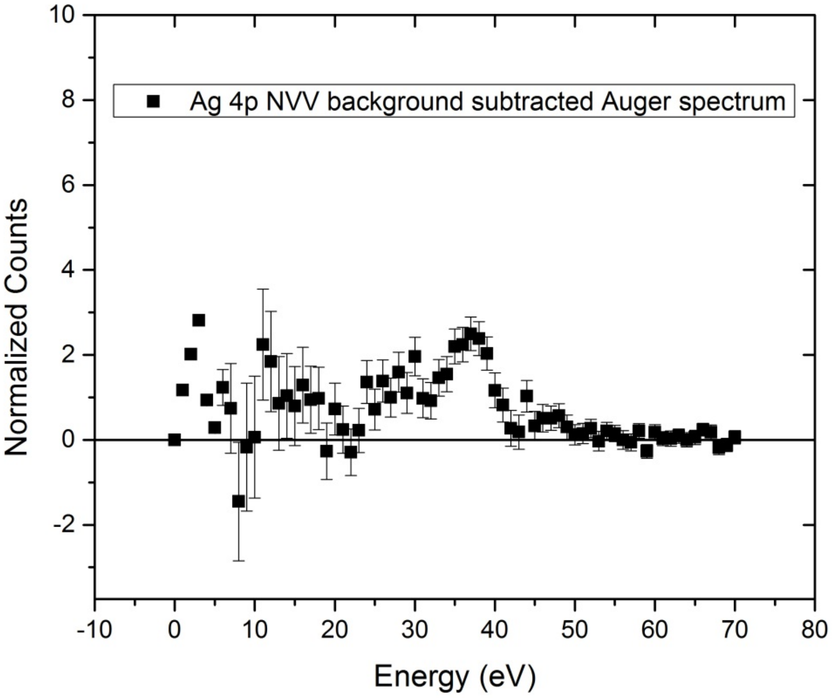

Figure 4-17 Ag(100) 4p NVV Auger spectrum after removing Auger unrelated contributions

The intensity ratio of LET to the Auger is compared before and after subtraction, before subtraction the total intensity I_{TOTAL}= 7.62;; I_{LET} = 6.17;; I_{Auger}= 1.45;; I_{LET}/I_{Auger} = 4.56 , and after subtraction I_{TOTAL}= 2.83;; I_{LET} = 1.52;; I_{Auger}= 1.31;; I_{LET}/I_{Auger} = 1.16.

4.8 Ag(100) APECS Data with High Photon Beam Energy 465eV

We obtained data with a high energy photon beam of energy 465eV. Figure 4.18 describes the singles spectrum at higher photon energy.

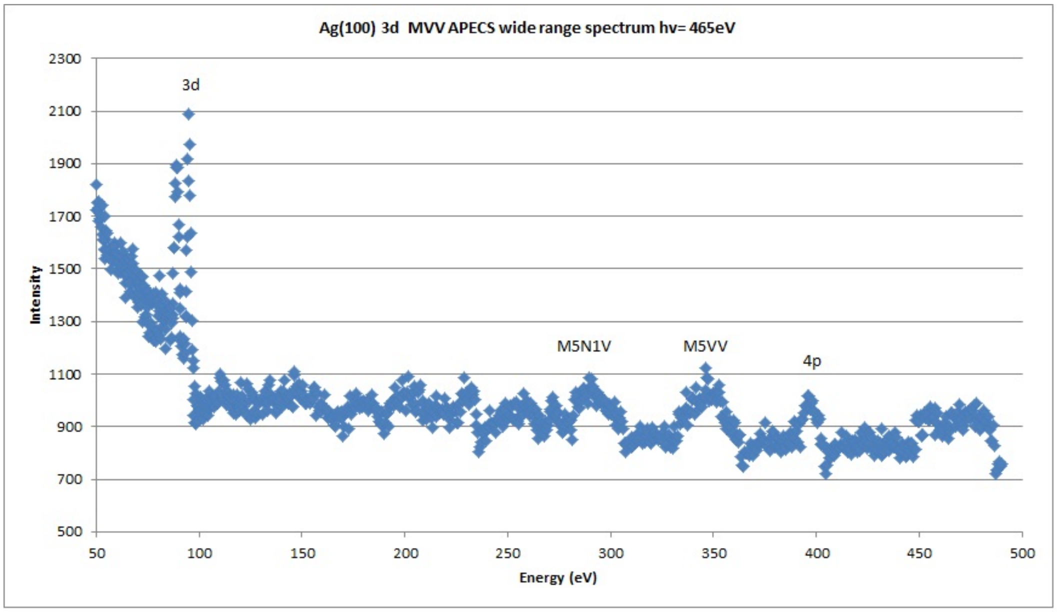

Figure 4-18 Ag(100) 3d MVV singles spectrum hv=465eV

Higher photon energy was used to probe deeper core, 3d contribution arising in the 4p spectrum, we wanted to observe the MNV contributions coming from 3d -4p core, Coster Kronig transition. It can be observed from the above figure 4-18, the 3d core and MVV peaks are very strong compared to the backgrounds, with the MVV peak at relatively high energy (although the 4p core is at higher energy ~400eV). The NVV has the smallest signal-to-background ratio with higher photon energy.

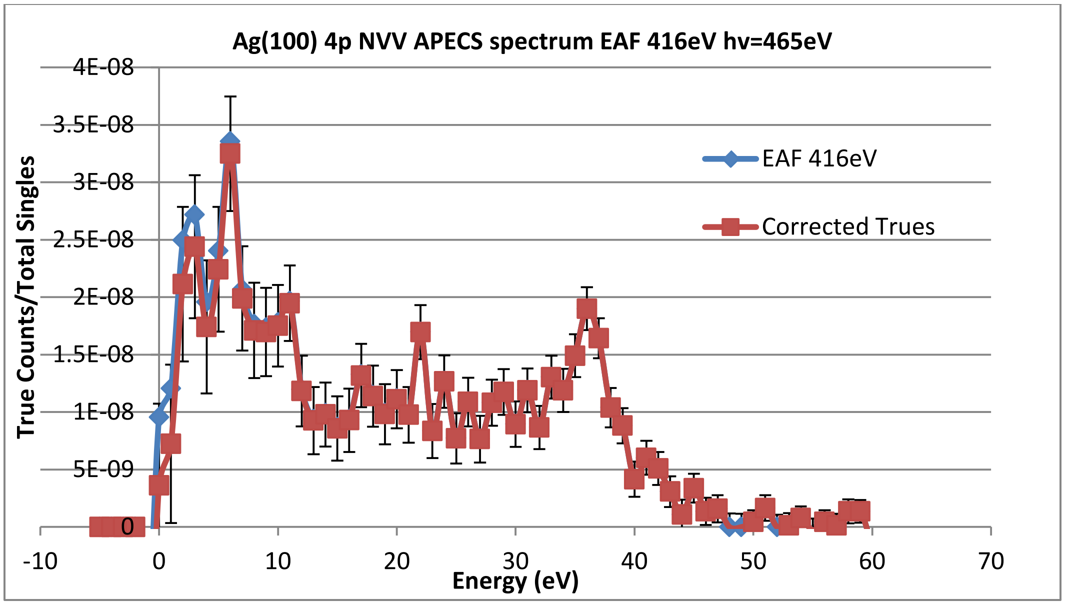

Figure 4-19 Ag(100) 4p NVV Auger spectrum obtained with higher photon energy hv=465eV

The above figure 4.19 shows APECS NVV spectrum with photon energy 465eV and fixed analyzer energy at 416eV of 4p core. The figure 4.20 shows the VB coincidence spectra at fixed analyzer energy 435eV. To account for sample bias of negative 15V both the spectra was shifted by 15eV.

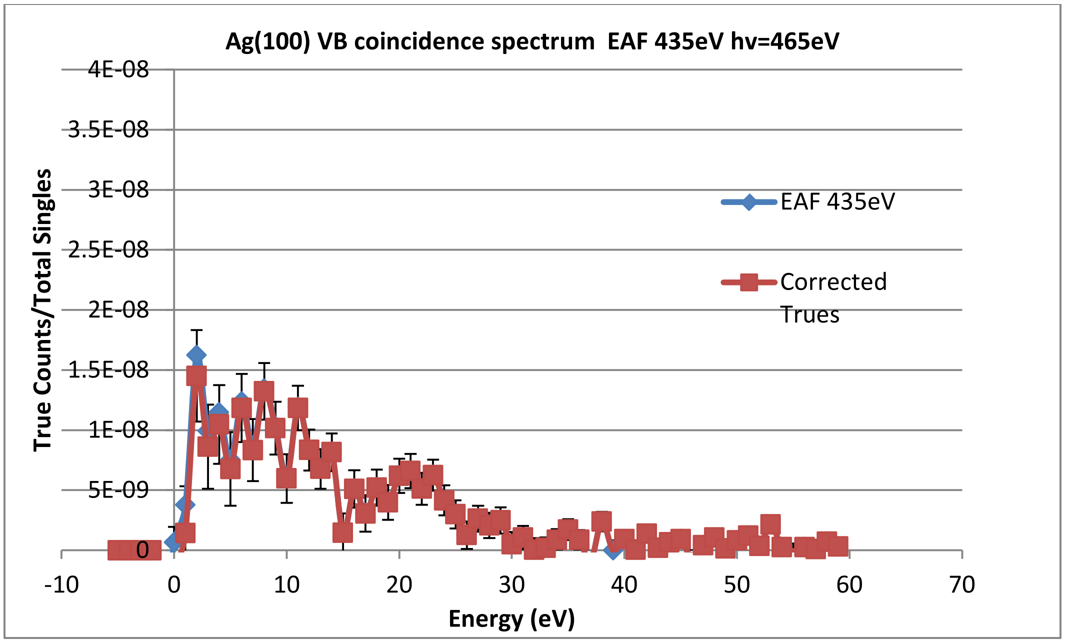

Figure 4-20 Ag(100) APECS spectrum obtained for fixed energy 435eV

Ag(100) coincidence spectra with fixed (KE) analyzer energy at 435eV, which is in a featureless valley above the Ag 4p core level and below the Ag VB, with hv=465eV, bias -15eV (in the above figure 4.20 spectrum shifted by 15eV) . The idea was that this spectrum should be like one of the "background" APECS spectra, at various energy shared (ΔE) delta values, that was taken at lower KE with hv=180eV.

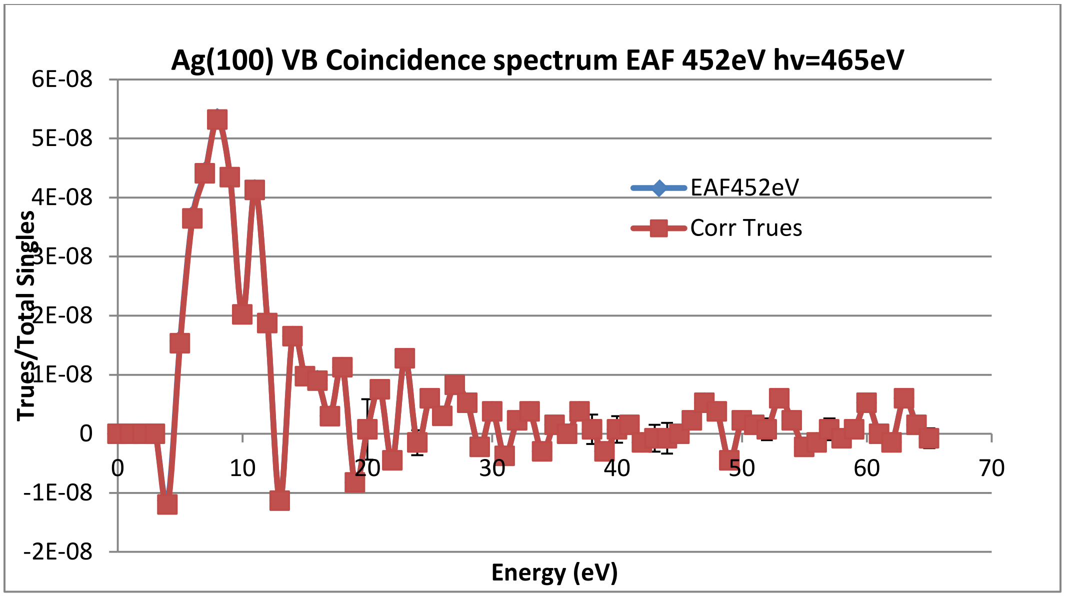

Figure 4-21 Ag(100) APECS spectrum for EAF 452eV

Ag(100) coincidence spectra with fixed (KE) analyzer energy at 452eV, with hv=465eV, bias -15eV (in the above figure 4.21 spectrum shifted by 15eV). The fixed analyzer energy is closer to the valence band. We wanted to observe the Plasmon gain peak (~11eV) as observed with the spectrum taken with hv=180eV.

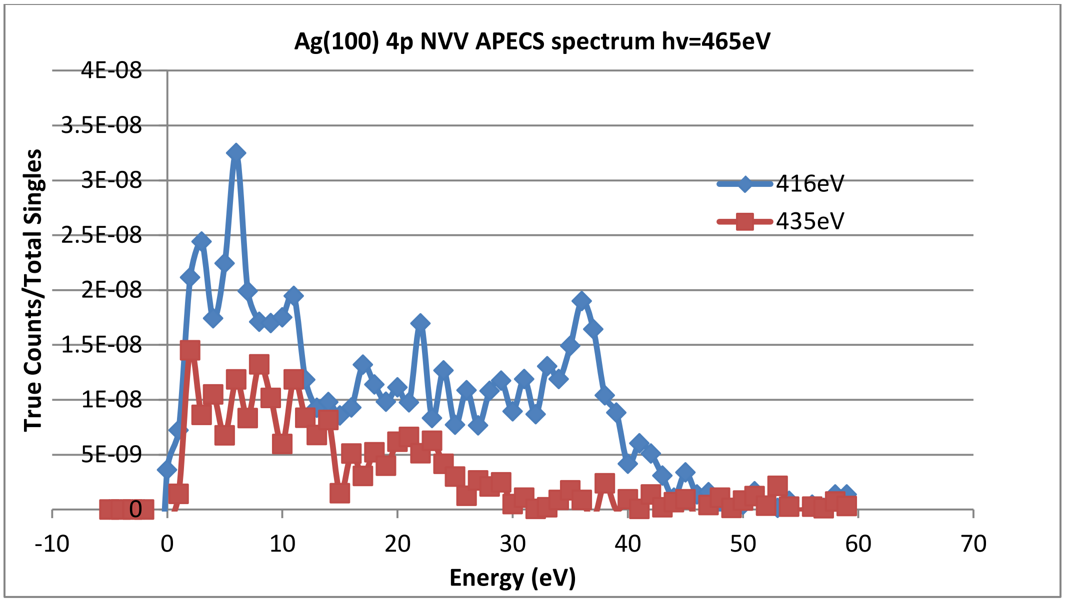

Figure 4-22 Ag(100) APECS spectrum with high photon energy hv=465eV

The figure 4.22 shows the 4p NVV APECS spectrum with a background coincidence spectrum. As the background spectra (red curve) measured is close to the 4p core energy, it is an approximate Auger unrelated contribution arising in the NVV spectrum due to inelastically scattered valence band electrons.

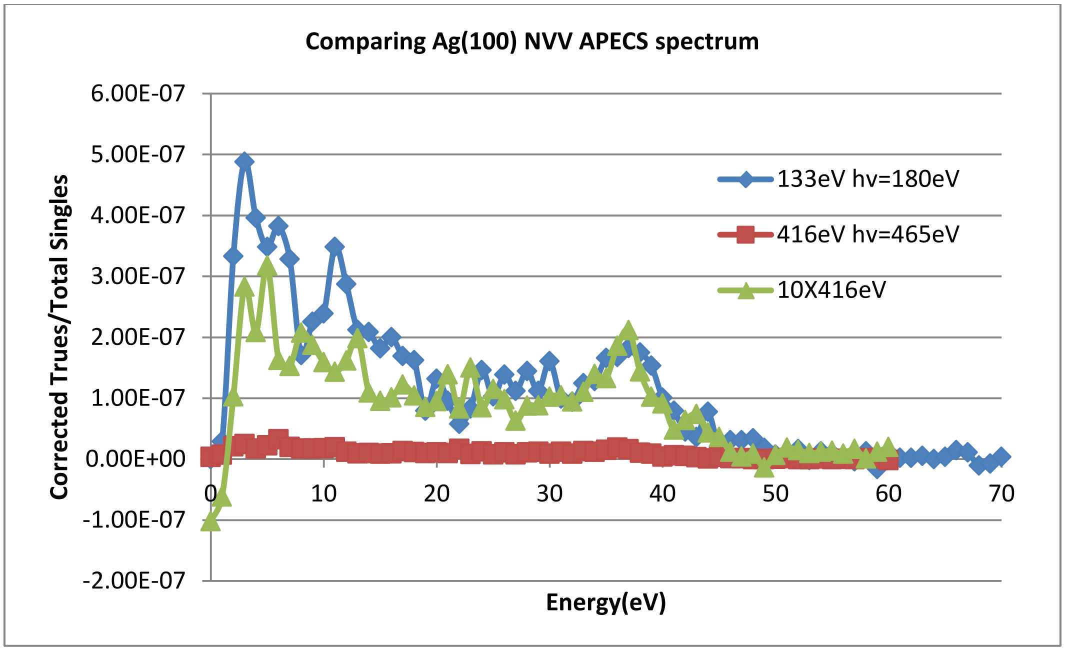

Figure 4-23 Comparing Ag (100) 4p NVV Auger spectrum with beam energies hv=180eV and 465eV.

The VB coincidence spectrum of fixed analyzer energy of 435eV and with photon energy 465eV is analogous to VB coincidence spectrum (figure 4.4) taken at fixed analyzer energy of 152eV with incident photon energy of 180eV. The energy difference of fixed analyzer energy with the core peak is similar in both.

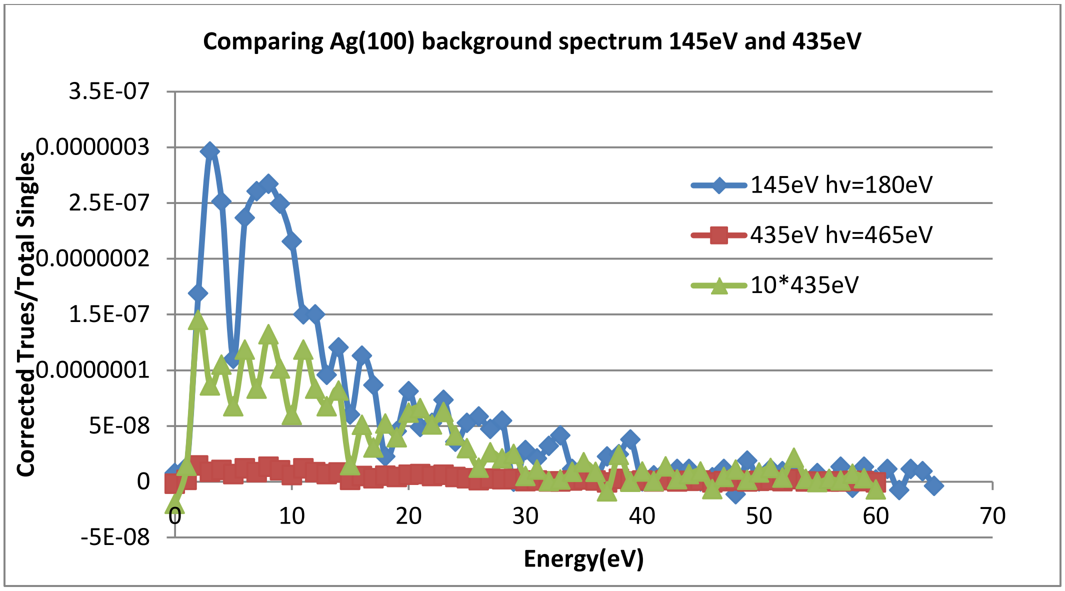

Figure 4-24 Comparing VB coincidence spectrum of EAF 145eV with 435eV

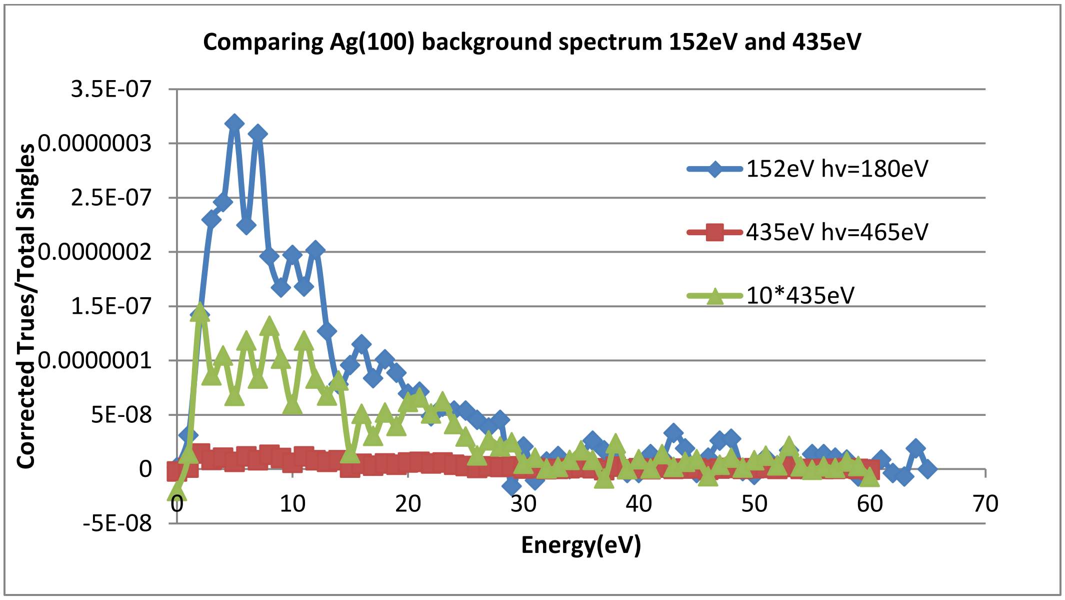

Figure 4-25 Comparing VB coincidence spectrum of EAF 152eV with 435eV

The spectral measurements with photon energy 180eV had an approximately ten times higher count rate when compared to 465 eV incident photon beam. This can be attributed to the signal to noise ratio of the spectrometer which is lower for higher photon energy. The figure 4.24 and 4.25 compares the VB –VB coincidence (background) spectra with different photon energies. It can be observed that the spectra at higher energy are less noisy.

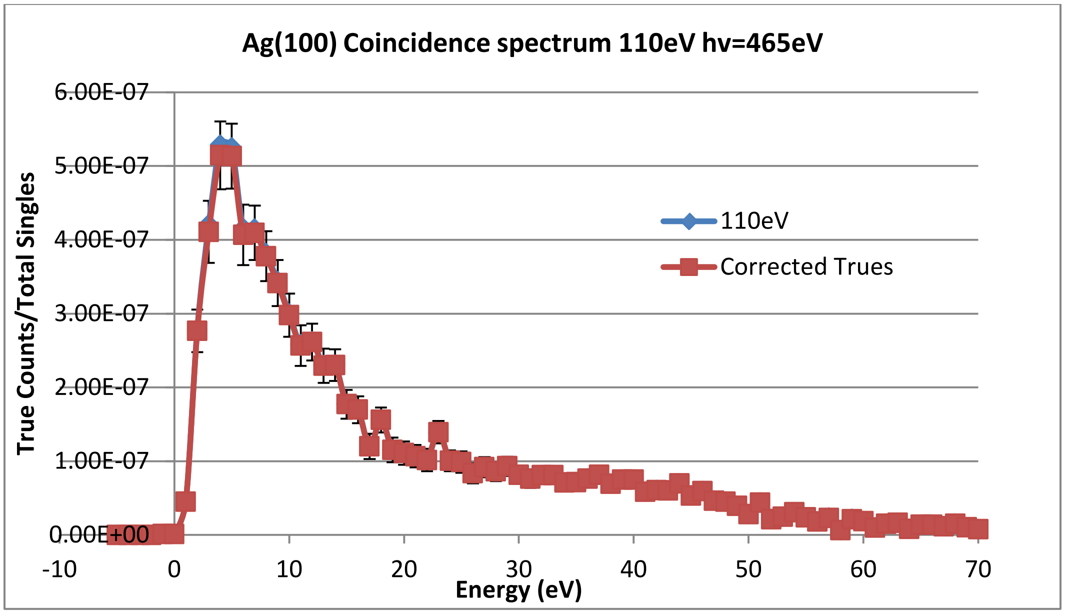

Figure 4-26 Ag(100) Coincidence spectrum for fixed analyzer energy at 110eV for hv=465eV

The above figure 4.26 is the high statistics VB coincidence spectrum taken below the 4p core energy for fixed analyzer energy at 110eV, that is, 3d core energy level.

4.9 Cu(100) APECS Data and Analysis

This section includes a new analysis of VB-VB coincidence measurements done for Cu(100) using a background data fit function which takes into account the plasmon peak observed at low energies in the coincidence spectrum. A series of VB coincidence measurement were done to measure the inelastically scattered valence band contribution in Cu (100) 3p MVV spectrum. The methodology followed was similar as mentioned for Ag. An incident photon beam of energy 200eV was used for Cu (100) experiment [2,10].

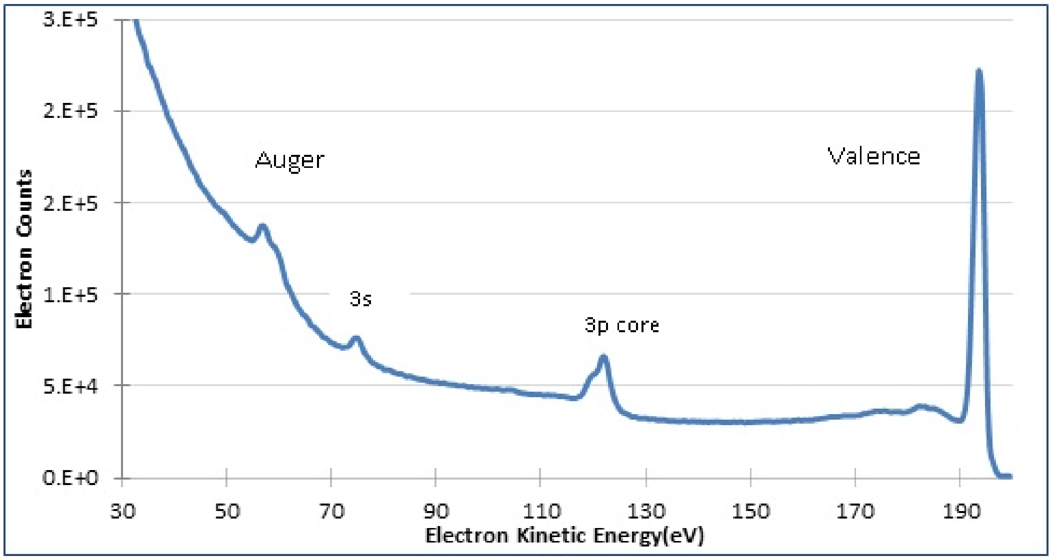

Figure 4-27 Cu(100) Single spectrum hv=200eV [2,10]

To estimate contribution of the inelastically scattered valence band we chose five fixed energies in the energy range between valence band and the core. The fix analyzer energies were 150eV, 165wV, 180eV, 190eV, 197eV as shown in figure 4.28 with their energy share value.

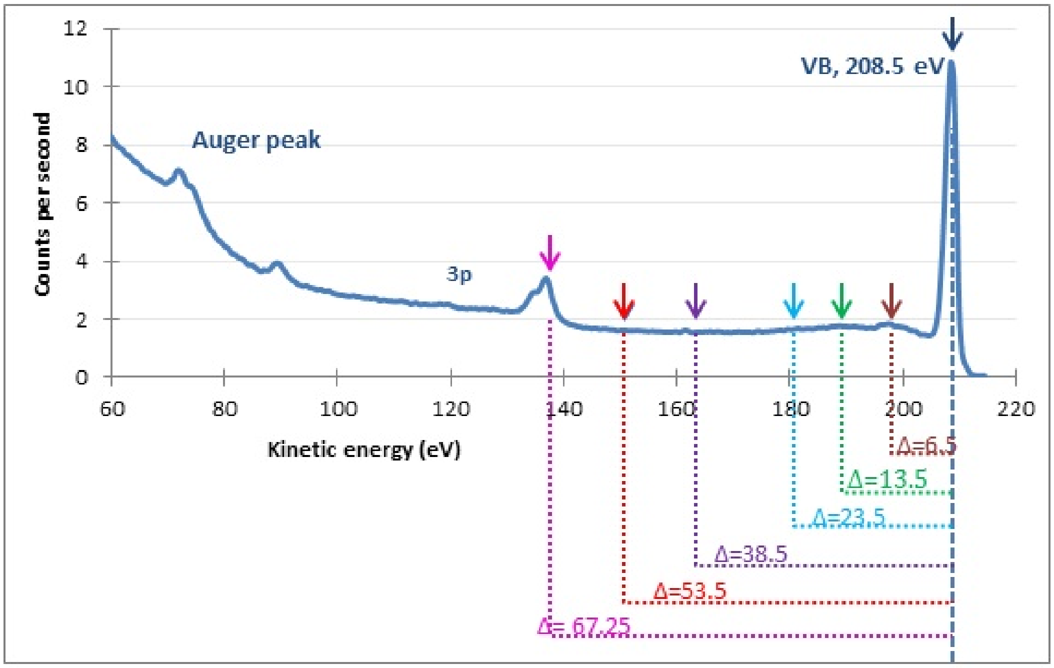

Figure 4-28 The fixed analyzer energies for Cu(100) [10]

To account for a Plasmon decay peak at the low energy (~10eV) of the APECS spectrum, we added a Gaussian peak term to equation 4.2.

$$B(E) = \frac{A(E-1)^{1.4}}{((E-1)+D)(E+\emptyset)^{m}} + \frac{B\, ln[(E_p-(E-1))/E_b]}{[(E_p-(E-1))/E_b\,]^{n}} + C + He^{\frac{-(x-F)^2}{2G^2}}, \qquad (4.3)$$

The data was fitted with the above background fit function the Cu VB coincidence when compare to analysis done in reference [10].

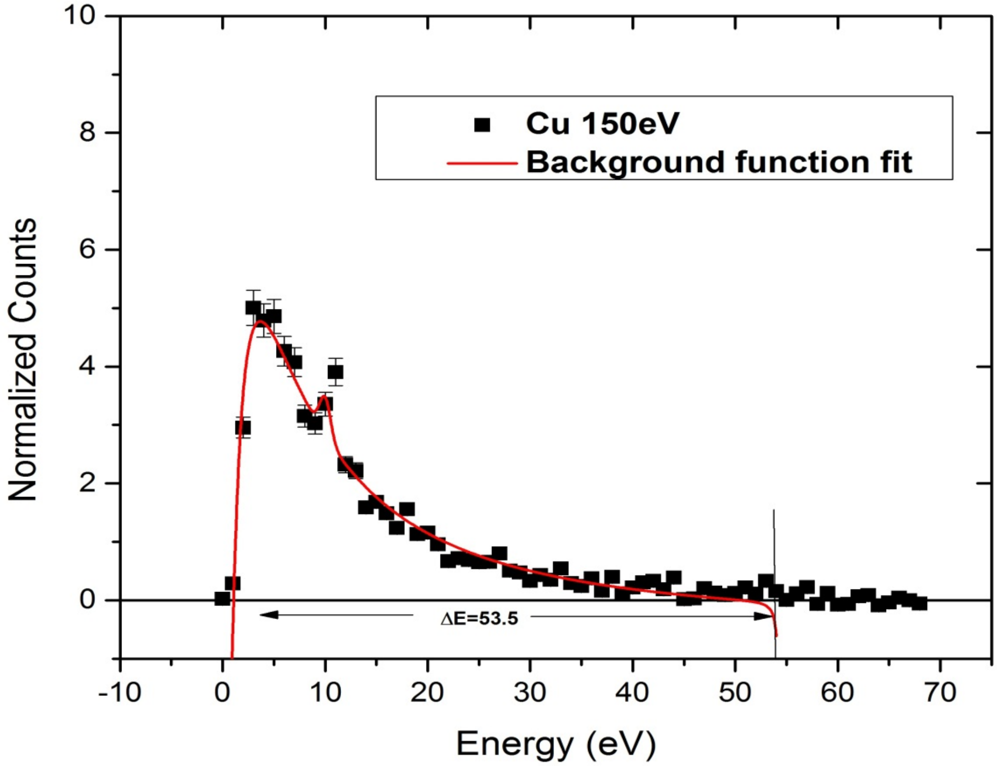

Figure 4-29 Cu(100) VB-VB coincidence spectra for the fixed analyzer energy 150eV

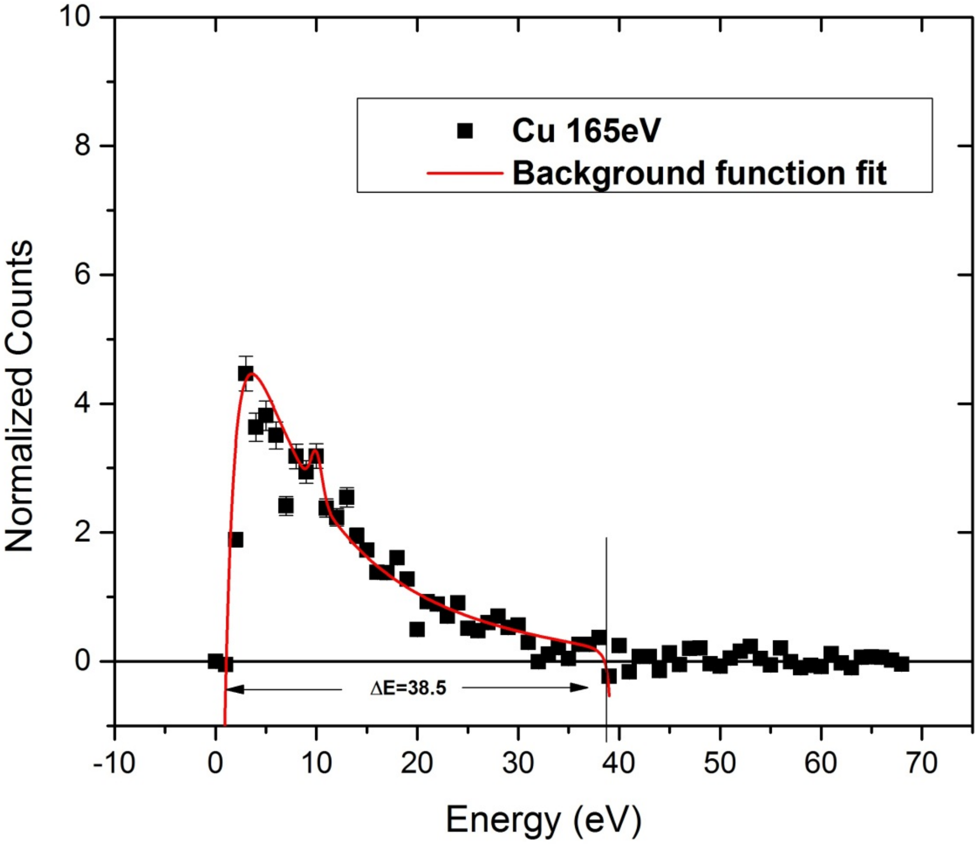

Figure 4-30 Cu(100) VB-VB coincidence spectra for the fixed analyzer energy 165eV

hv=200eV

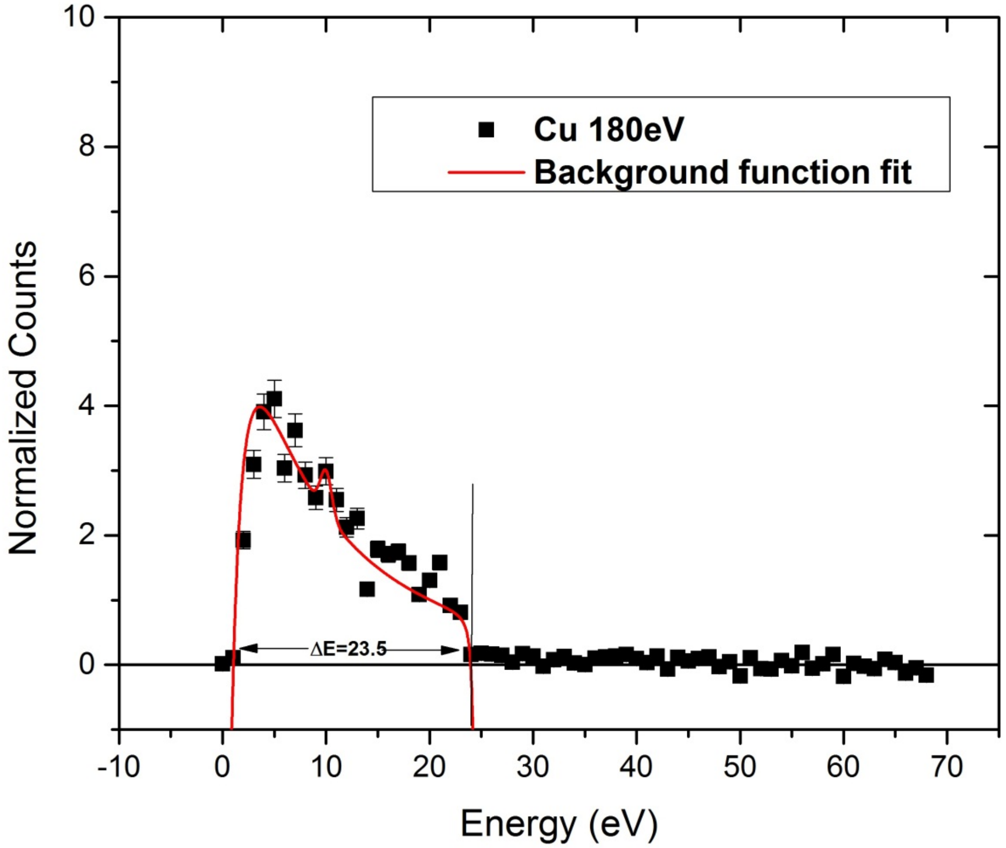

Figure 4-31 Cu(100) VB-VB coincidence spectra for the fixed analyzer energy 180eV

hv=200eV

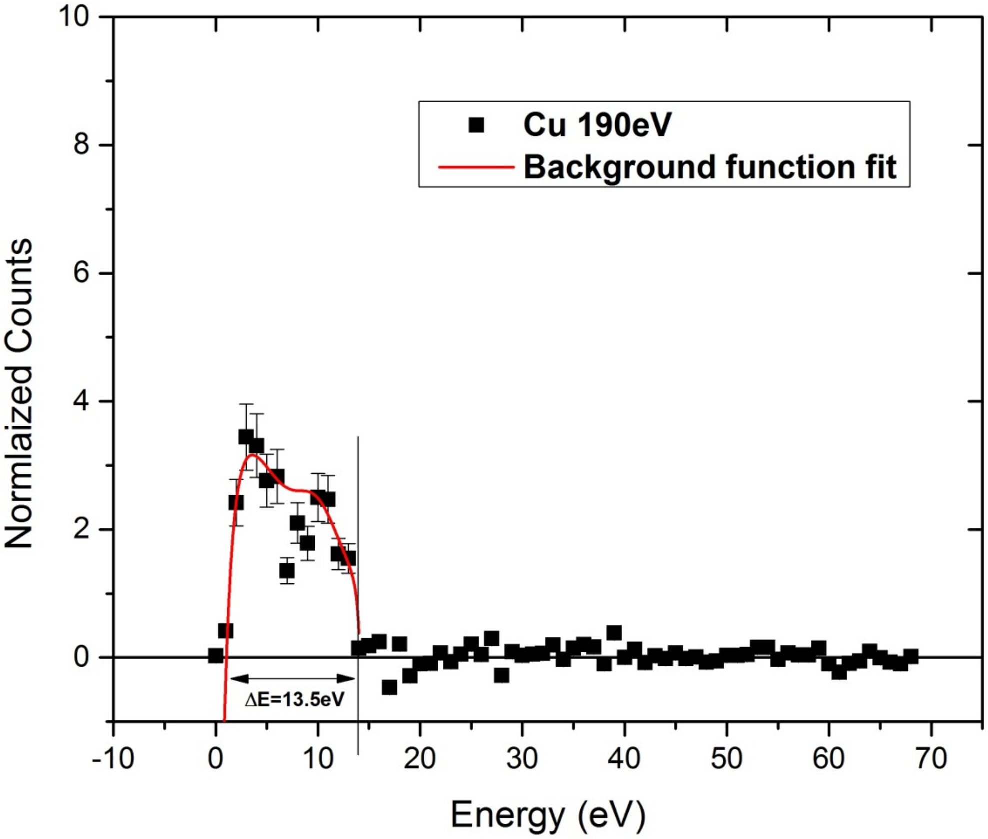

Figure 4-32 Cu(100) VB-VB coincidence spectra for the fixed Analyzer energy 190eV

hv=200eV

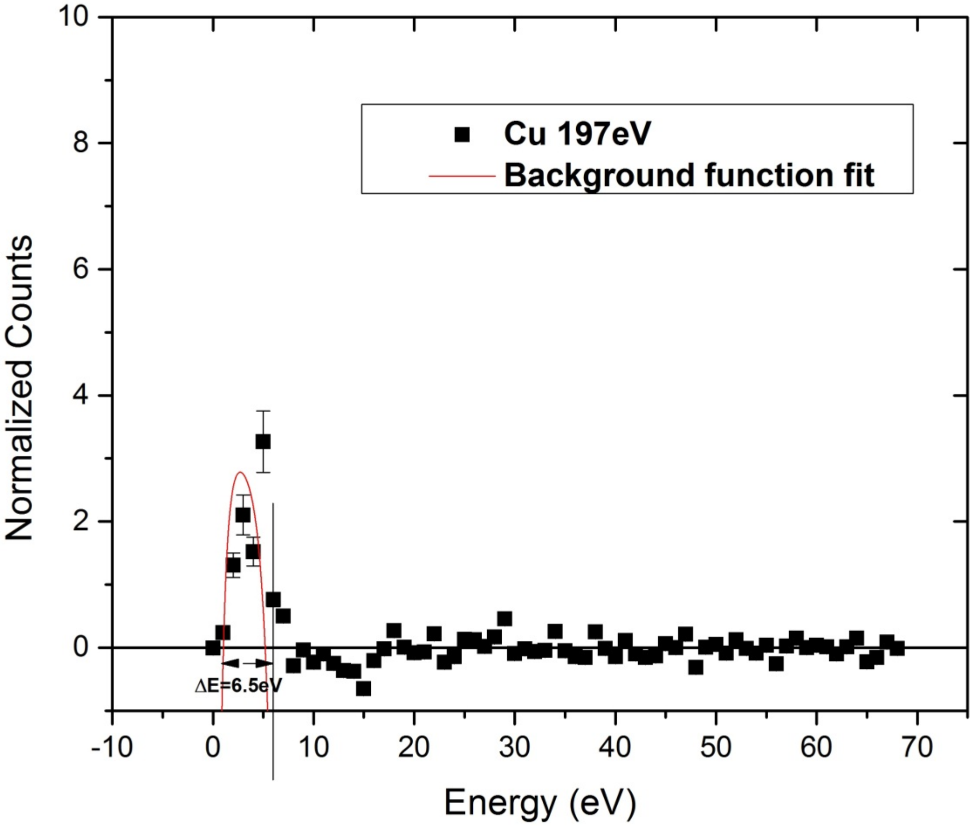

Figure 4-33 Cu(100) VB-VB coincidence spectra for the fixed analyzer energy 197eV

hv= 200eV

The distribution of the energy shared ΔE between the valence electrons can be seen from energy range 0 to 15.5eV. The background function, B(E) of equation 4.3, is used to fit the data using Origin 9.1. The respective parameters were recorded and used in extrapolation.

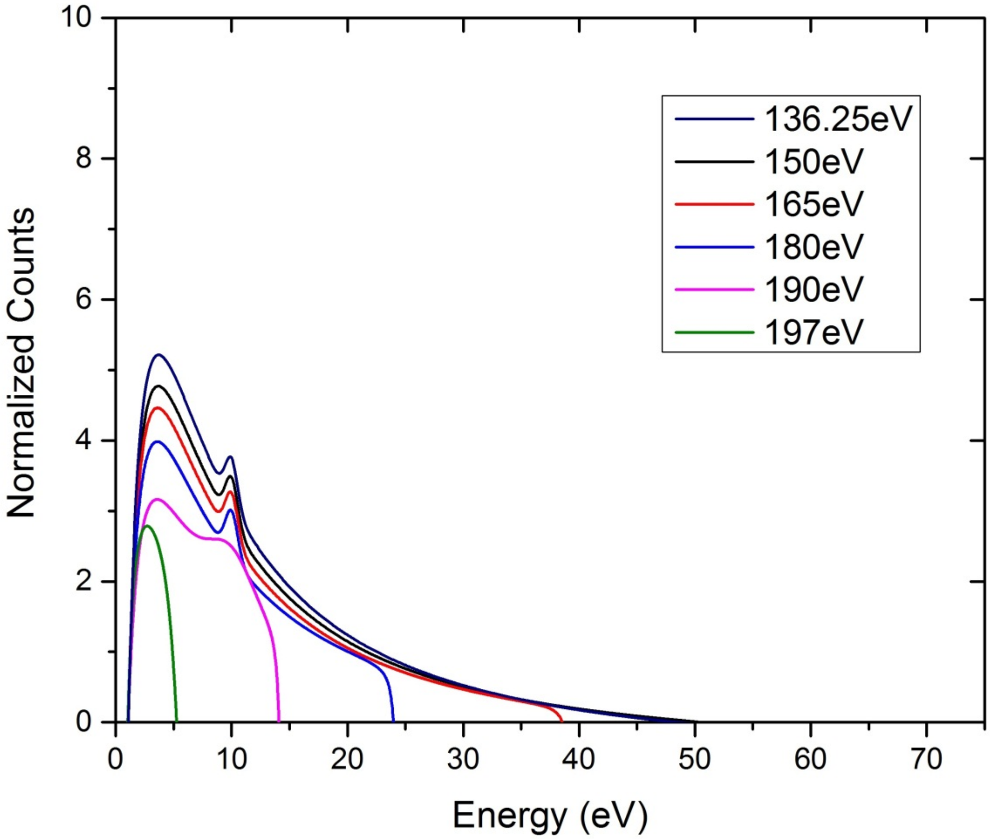

Figure 4-34 The extrapolation of the Auger unrelated contribution on different kinetic energies. The topmost curve is the estimated contribution at 3p core of Cu(100)

The topmost curve is the extrapolated curve for 136.25eV, 3p core energy and is the estimate of Auger unrelated contribution arising from inelastically scattered VB electrons.

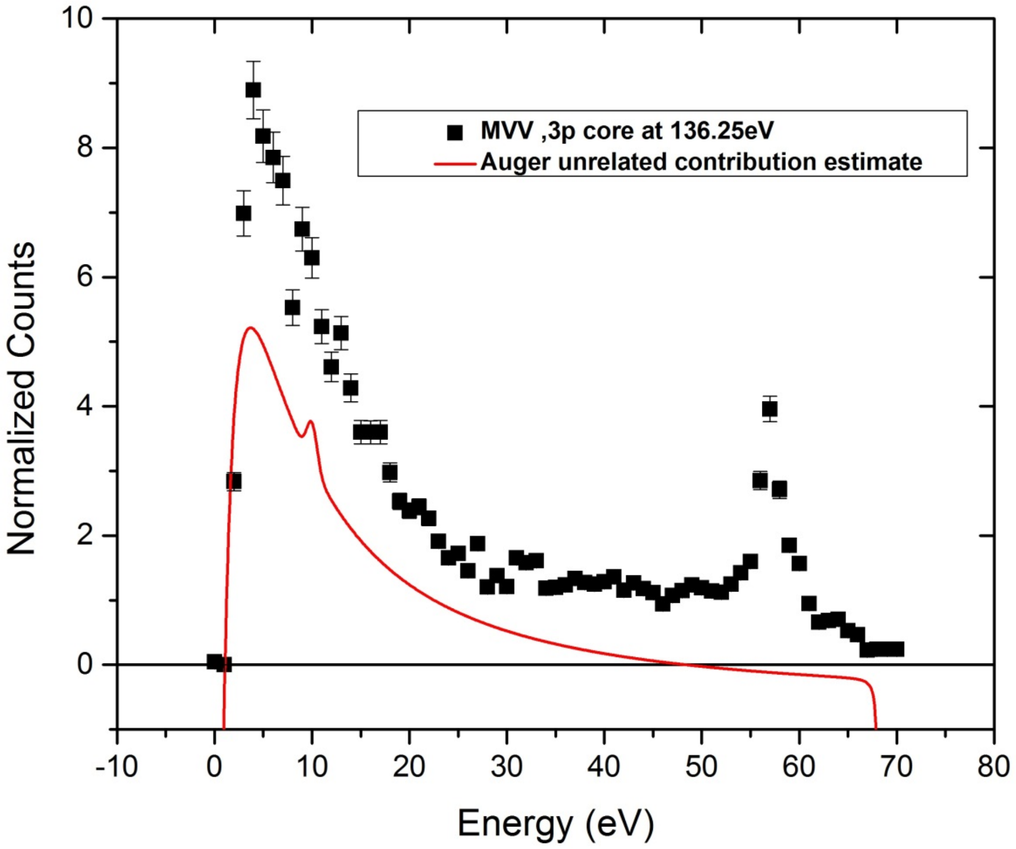

Figure 4-35 Red curve shows the estimated contribution from the inelastically scattered Valence Band of Cu(100)

The red curve shown in the above figure 4.35, is the extrapolated estimate for the inelastically scattered VB electrons contributing to the LET. This Auger unrelated contribution was subtracted to get a spectrum related to Auger.

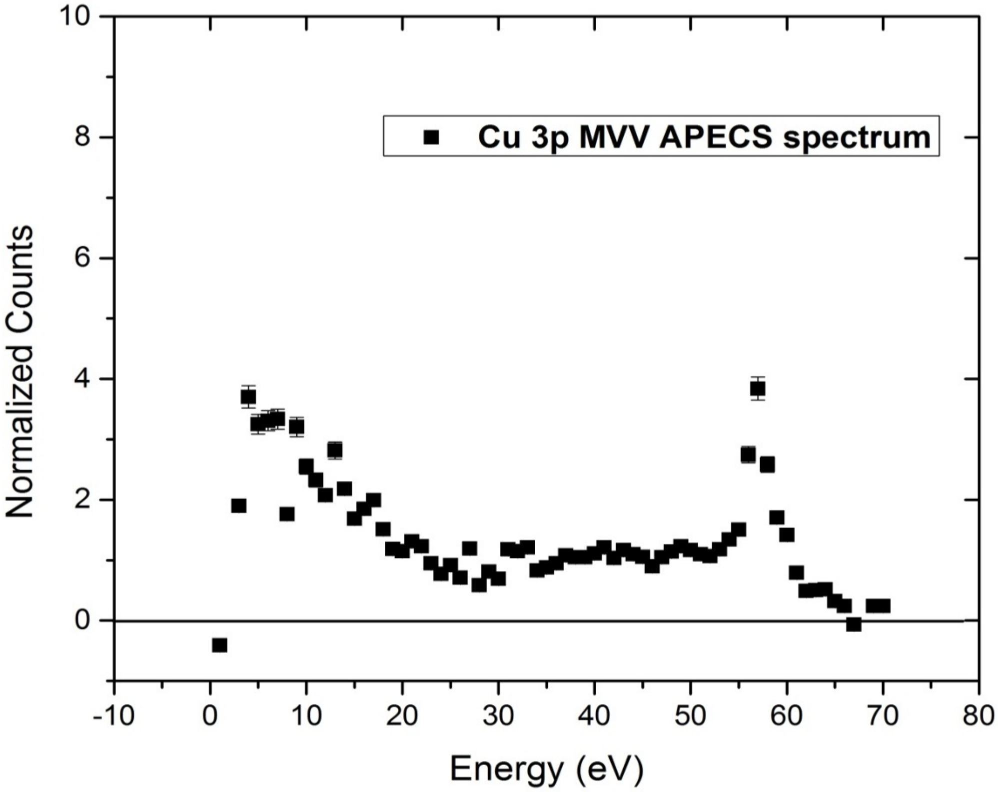

Figure 4-36 Cu 3p MVV Auger spectra after removing Auger unrelated contributions

The above figure (4.36) is the spectrum free of the Auger unrelated contribution of inelastically scatted VB electrons. The Auger peak is followed by a tail at low energies. This tail is as a result of inelastically scattered Auger electrons or multi Auger electrons decay associated with the Auger transitions. The integrated intensity ratio of the intensity in the low energy tail region, I LET to the intensity in the Auger peak region, I Auger, is 2.78 (I LET=2.81E-6, I Auger =1.01E-6) after subtraction of Auger unrelated.

4.10 Conclusion

We have measured the contribution of inelastically scattered electrons associated with the Auger peak arising from surface and sub-surface region of Ag(100) and Cu(100). The inelastically scattered valence band photoelectrons and the Auger electrons along with the secondary electron generated by Plasmon decay attribute to the spectral intensity of the low energy tail.

The low energy tail contribution comes from both Auger transition related and unrelated. The unrelated factor is mainly due to the inelastically scattered VB electron, this Auger unrelated contribution comes from the surface and top few layers of the sample and can be estimated using the electron's elastic scattering probabilities. We have calculated and estimated theoretically the ratio of LET and the peak with the contributions arising from the top layers of the sample, presented in chapter 5. From the experimental data presented in this chapter (4) we observed substantial contribution arising from inelastically scattered valence band electron towards the low energy tail, for silver (copper), I_{TOTAL}= 2.83 (3.82);; I_{LET} = 1.52 (2.81);; I_{Auger}= 1.31(1.01);; I_{LET}/I_{Auger} = 1.16 (2.78) (Fig 4.17 and Fig 4.36). The experimental ratio is compared with the theoretical estimates in the next chapter.

Chapter 5

Theoretical Modeling of the Low Energy Tail of the Auger peak

5.1 Introduction

The low energy tail (LET) as defined in chapter 1 is the spectral region below the Auger peak down till 0eV. Earlier work by *Jensen et. al.* [1] suggesting high spectral weight in the low energy region of the Auger spectrum motivated us to perform the measurement of the spectrum below the Auger peak down till 0eV. The high spectral weight intensity obscures important peaks of the spectrum and hence it's important to understand the contributing factors to the LET for better quantification of the Auger and other low energy peaks. Often the less intense Auger signal is accompanied by a large background signal comprising of redistributed primaries (backscattered) electrons, secondary electrons or inelastically scattered electrons. There have been several background removal techniques, namely measuring the derivative spectrum and numerical background calculations. There have been theoretical calculations done by Shirley, Tougaard, Werner et al [40-44] to calculate the Auger transition related and unrelated contributions.

5.2 Background Removal

The removal of background is often complicated due to many contributing factors in the spectrum. It's challenging to measure each contribution experimentally due to the electron's indistinguishable nature. There have been numerical and semi empirical methods developed and being currently used by scientists to obtain a background free spectrum, but often these techniques were used only around the line shape or near peak region [13, 45]. Also many times to remove background contribution the spectral data is differentiated making the overlapping peaks separate. A caution should be followed while removing the background as it affects the peak intensities and hence the quantification accuracy. The theoretical models for the background removal are often sample dependent, hence a sample suitable method should be chosen. It is often recommended that background should be removed prior to data fitting so as the features of the line shapes are not lost, and improper background subtraction can introduce asymmetric peak. There are three commonly used background removal techniques. First is the linear background removal, the second one is Shirley method which computes integral background and the third one based on inelastic and elastic loss processes called Tougaard style background.

5.2.1 Linear Background

In linear background determination a straight line drawn from a point closer to the low kinetic energy of the peak E_{min} to a point on the higher kinetic energy side E_{max}. This contribution is subtracted from the peak to get a background free peak. A drawback of this method is that it's not well defined and depends on the user for the start (E_{min}) and end (E_{max}) values respectively.

5.2.2 Shirley Background

This is a non-linear, integral background method and involves iterative method for calculations of the background.

$$F^n(E) = \mathrm{J(E)} - \mathrm{k}_n \int_E^{Emax} F^{n-1}(E')dE', \qquad (5.1)$$

The above equation is used for computing the Shirley background. Here F(E) is the primary peak structure, J(E) is the measured spectrum or measured flux, $F^0(E)=J(E)$ and k_n can be found by solving condition $F^n(E_{min})=0$. It is observed that the series typically converges within 5 iterations $F^n(E) \sim F^{n-1}(E)$. The values of E_{min} and E_{max} are selected by the user. The method is dependent of the E_{min} value. It is observed that in general for narrow peaks it give similar peak areas as we get in linear background subtraction, and for wider range peaks it can give incorrect peak areas (sometimes it over subtracting giving negative peak areas) which can mislead the quantification and data analysis. To minimize the error the values for E_{min} and E_{max} must be chosen consistently relative to all of the peaks.

5.2.3 Tougaard Background

The Tougaard background is considered to be more accurate than the linear and Shirley backgrounds as it is based on the extrinsic loss process that is elastic and inelastic scattering loss processes that contribute to the background.

$$F(E) = \mathrm{J(E)} - \mathrm{B}\int_{E}^{Emax} J(E')\frac{E'-E}{[C+(E'-E)^2]^2}\,dE', \qquad (5.2)$$

In background subtraction, contribution from measured spectrum J(E) vs Energy is subtracted to get primary spectrum F(E) vs E, removing the extrinsic processes. The second term in the integral is universal cross section, B and C are constants for metals their values are approx. 2866eV^2 and 1643eV^2 respectively.

5.3 Estimation of the Inelastically Scattered Contribution using Tougaard Background Function

We used QUASES software (developed by Prof. Sven Tougaard) to estimate the inelastically scattered Auger electron contribution for Cu(100) and Ag(100) sample. The experimental data obtained from the APECS experiment was used as our raw data. QUASES [46, 47] uses the equation 5.2 to calculate the inelastically scattered electron contribution coming from the top layers of the sample. The formula is based on the inelastic mean free path of the electrons as a function of elemental depth and energy. The Tougaard formula considers the differential inelastic scattering cross section [48], that is, the diff inelastic mean free path cross section (DIMPF) gives the probability that the electrons with energy E will suffer energy loss in the sample layers and with an energy range we want to compute. The formula computes the inelastically scattered electron contribution of the peak under study, in our case Cu 3p MVV and Ag 4p NVV

Auger peak. In the estimates using the QUASES, the parameter B (of equation 5.2) is adjusted to give zero intensity for energy region 30eV-50eV below the peak. The value of B and thus the numerical estimate of inelastically scattered electron contribution vary with the choice of E_{min}.

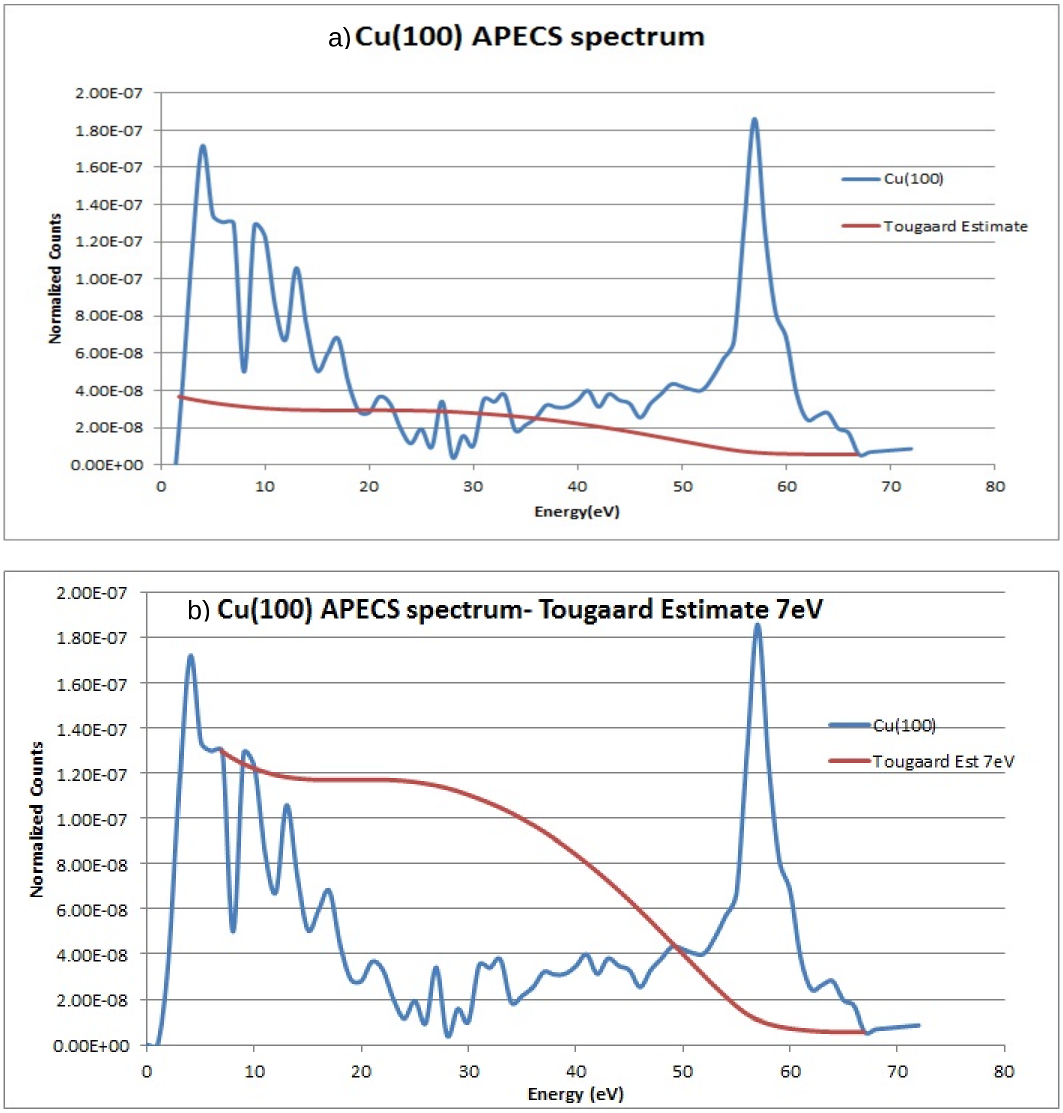

Figure 5-1 Tougaard background estimate using QUASES for Cu(100) with E_{min} as (a) 2 eV and (b) 7eV.

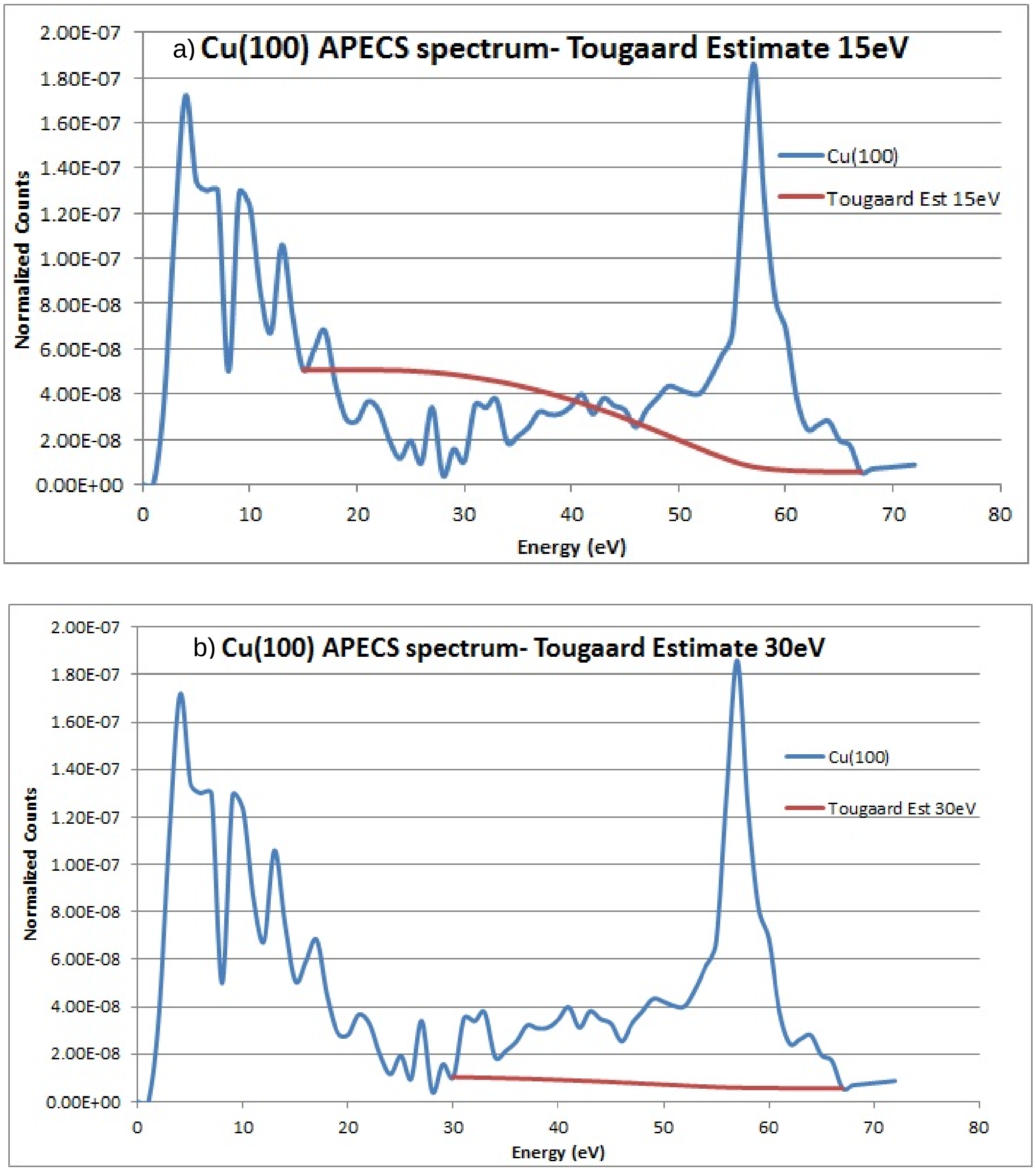

Figure 5-2 Tougaard background estimate using QUASES for Cu(100) with a) E_{min} 15eV and b) 30eV.

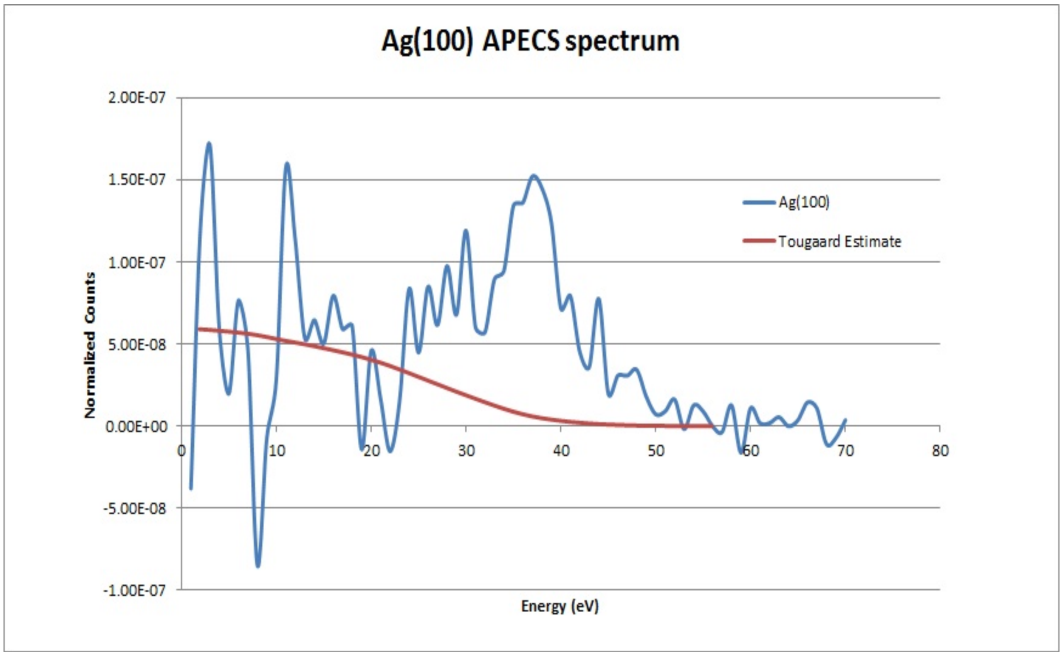

Figure 5-3 Tougaard background estimate using QUASES for Ag(100) with E_{min} as 2eV.

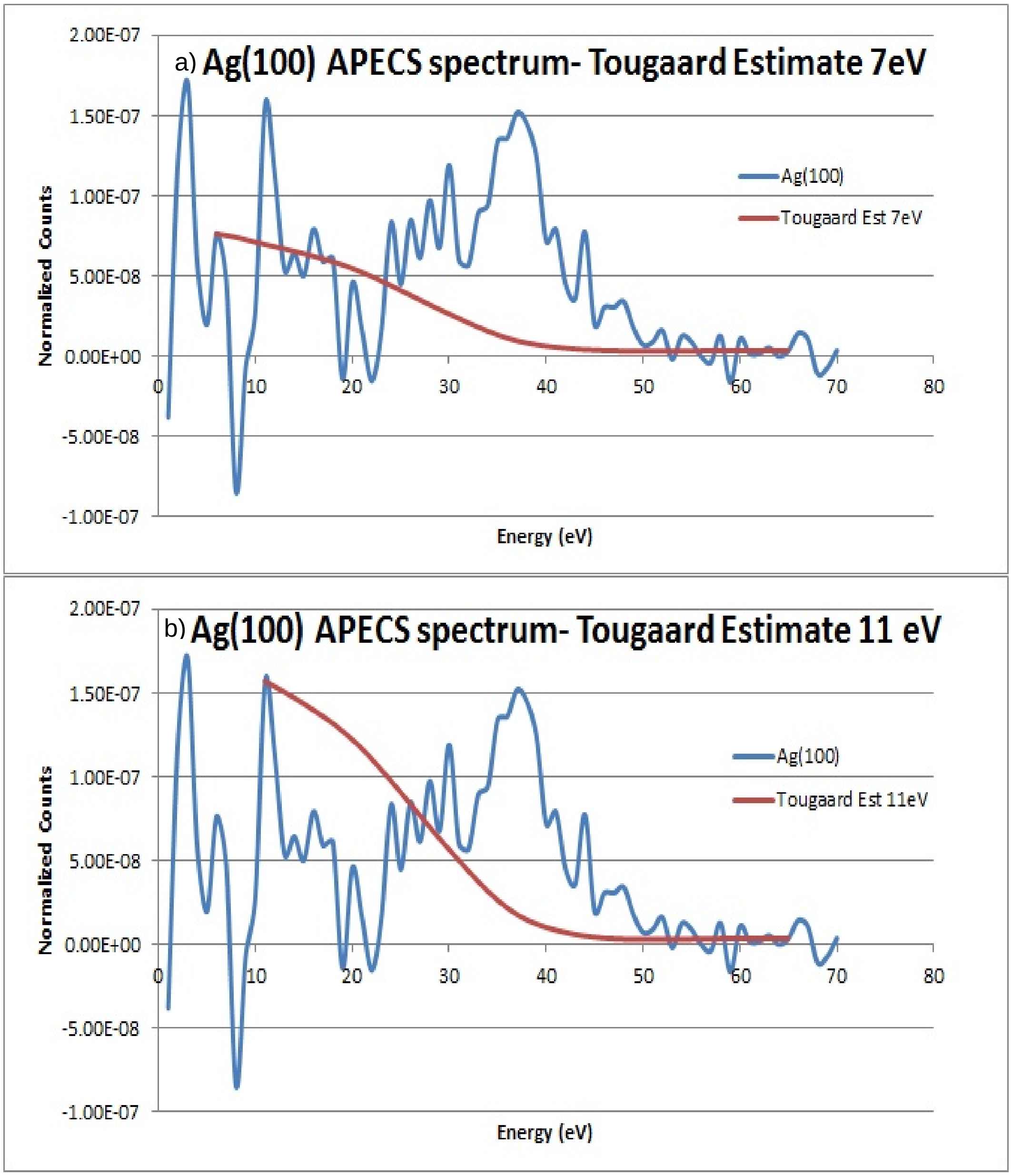

Figure 5-4 Tougaard background estimate using QUASES for Ag(100) with E_{min} (a) 7eV and (b) 11eV.

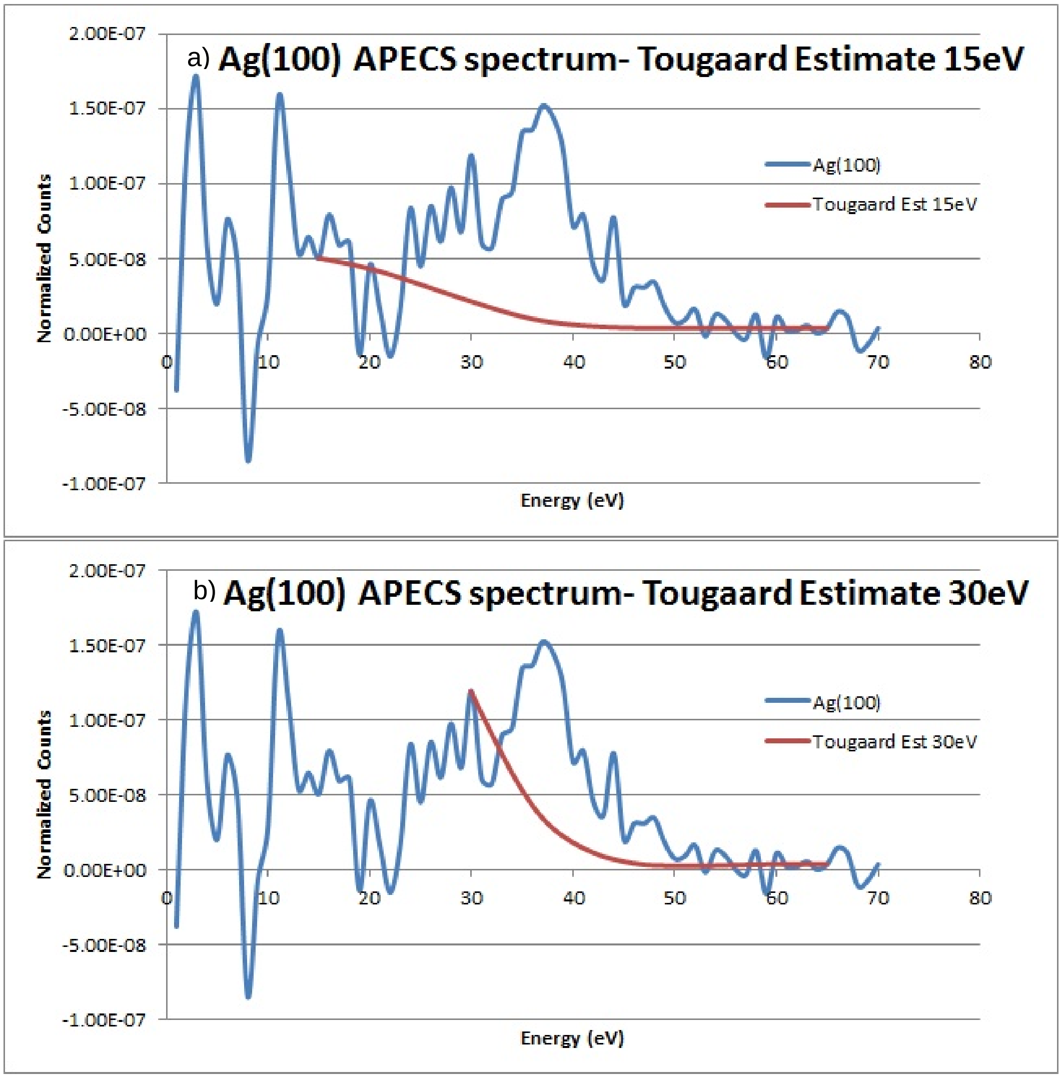

Figure 5-5 Tougaard background estimate using QUASES for Ag(100) with E_{min} as (a) 15eV and (b) 30eV.

The Tougaard estimate of the inelastically scattered Auger electrons using QUASES software for Cu(100) and Ag(100) with different E_{min} are shown from figures 5.1 through 5.4. It can be observed from the figures that the inelastic contribution calculation by Tougaard formula which is a numerical estimate relies on the E_{min} data point and B value fitting. The choice of E_{min} gives different and inconsistent estimate for our data at low energies and hence is not adequate to account for LET.

5.4 Estimate of LET to Peak Ratio using the Semi Empirical Calculation

Here we attempt to estimate the ratio of the fraction of Auger electrons that are emitted elastically from the surface. The probability of electron coming from a depth ‘x’ in the sample with the inelastic mean free path of length λ,

without losing its energy (elastic scattering) is given as: $e^{\frac{-x}{\lambda\, Cos\, \theta}}$, (5.3)

The intensity of the peak due to elastic scattering will be [49].

$$I_{peak} = I_o\, e^{\frac{-x}{\lambda\, Cos\, \theta}}, \qquad (5.4)$$

Let a layer be of depth d units (A), then intensity coming from the first layer (1) of depth d (the inter planer distance) in APECS will be,

$$I_{peak1} = I_o\left(e^{\frac{-d/2}{\lambda a\, Cos\, \theta}} + A^{(1)}_{\text{backscattered elastic}}\right)\left(e^{\frac{-d/2}{\lambda c\, Cos\theta}} + C^{(1)}_{\text{backscattered elastic}}\right), \qquad (5.5)$$

Here λa and λc are inelastic mean free paths of Auger and Core electron. Here we assume that the intensity is coming from half of the depth, that is (n-1/2).

The intensity contributing to the peak from second layer (2) of equal depth will be,

$$I_{peak2} = I_o\left(e^{\frac{-(2-\frac{1}{2}).d}{\lambda a\, Cos\, \theta}} + A^{(2)}_{\text{backscattered elastic}}\right)\left(e^{\frac{-(2-\frac{1}{2}).d}{\lambda c\, Cos\, \theta}} + C^{(2)}_{\text{backscattered elastic}}\right), \qquad (5.6)$$

Similarly intensity from n th deep layer will be,

$$I_{peak\ n} = I_o\left(e^{\frac{-(n-\left(\frac{1}{2}\right)).d}{\lambda a\, Cos\, \theta}} + A^{(n)}_{\text{backscattered elastic}}\right)\left(e^{\frac{-(n-\left(\frac{1}{2}\right)).d}{\lambda c\, Cos\, \theta}} + C^{(n)}_{\text{backscattered elastic}}\right), \qquad (5.7)$$

The probability of $A^{(n)}_{\text{backscattered elastic}}$ and $C^{(n)}_{\text{backscattered elastic,}}$ scattering will be is assumed to be negligible.

The total peak intensity, combining the parenthesis,

$$I_{\text{peak}}=I_{o}\sum_{n=1}^{\infty}\left(e^{\frac{-(n-\left(\frac{1}{2}\right)).d}{\lambda a\, Cos\,\theta}}\right)\left(e^{\frac{-\left(n-\left(\frac{1}{2}\right)\right).d}{\lambda c\, Cos\,\theta}}\right), \qquad (5.8)$$

The probability of inelastically scattered electrons contributing will be (from eq(5.3))

$$1-e^{\frac{-x}{\lambda\, Cos\,\theta}}\ , \qquad (5.9)$$

Now to calculate the total LET contribution we also need to consider the secondary electrons generated by inelastically scattered Auger electrons, thus we will have secondary electron yield δ with equation (8) [51-53]. To take into account the electrons which are able to transmit, we will consider probability of the transmitted electrons. The contribution due to inelastically scattered (Auger) peak electrons towards the low energy tail would be (from eq(5)), with same IMFP,

$$I_{\text{LET m}} = I_{o}\sum_{n=1}^{\infty}\left(m*\left(1-\ e^{\frac{-(n-\frac{1}{2}).d}{\lambda a\, Cos\,\theta}}\right)+\delta\right)\left(e^{\frac{-(n-\frac{1}{2}).d}{\lambda c\, Cos\,\theta}}\right)\left(e^{\frac{-(n-\frac{1}{2}).d}{25\,.Cos\,\theta}}\right), \qquad (5.10)$$

An inelastically scattered electron after sharing it’s energy can produce one or more electrons (it may also produce none); of the electrons generated all may exit from the sample or only some will be successful coming out of the sample. To take this into account let us define variable m, a number, for m=1, one inelastically scattered electron is generated, for m=2, two are generated and so on.

For Cu, IMFP λa= 3.59 Å for electron energy 60eV [50], λc= 4.5 Å for 3p core electron energy (at 136 eV) and assuming each layer depth d= 1.8 Å with θ for our electron detector is 48°± 5°.

The contribution from each layer towards the intensity of the peak and towards the low energy tail due to inelastically scattered electrons will be (from equation 5.8 and equation 5.10).

Table 5-1 Theoretical intensity ratio and layer contribution for Copper

Cu	**Layer1**	**Layer2**	**Layer3**	**Layer4**	**Layer5**	**Total 5 Layers**
I Peak	0.50989	0.13256	0.03446	0.008961	0.00233	0.688217
I LET (m=1)	0.57100	0.40787	0.23083	0.12087	0.061302	1.39187
I LET (m=2)	0.79060	0.64218	0.37594	0.199402	0.10169	2.1098

The ratio I LET/ I Peak = 2.02 (for m=1), and I LET/ I Peak = 2.63 (for m=2).

The ratio of I LET/ I Peak obtained after subtraction of experimentally measured inelastically scattered VB contribution is 2.2, both the above ratios are close to those predicted by Jensen et al.

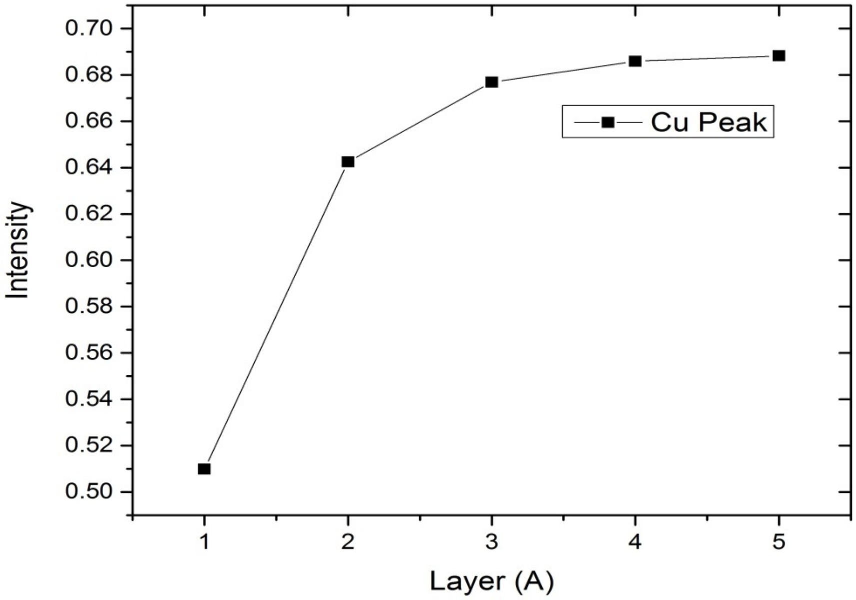

Figure 5-6 Layer contributions to the Cu peak intensity (each layer of thickness 1.8 Å)

It can be observed from the above figure 5.2, the main contribution towards the Auger peak arises from the first and second layer, that is, from the top layers of the sample.

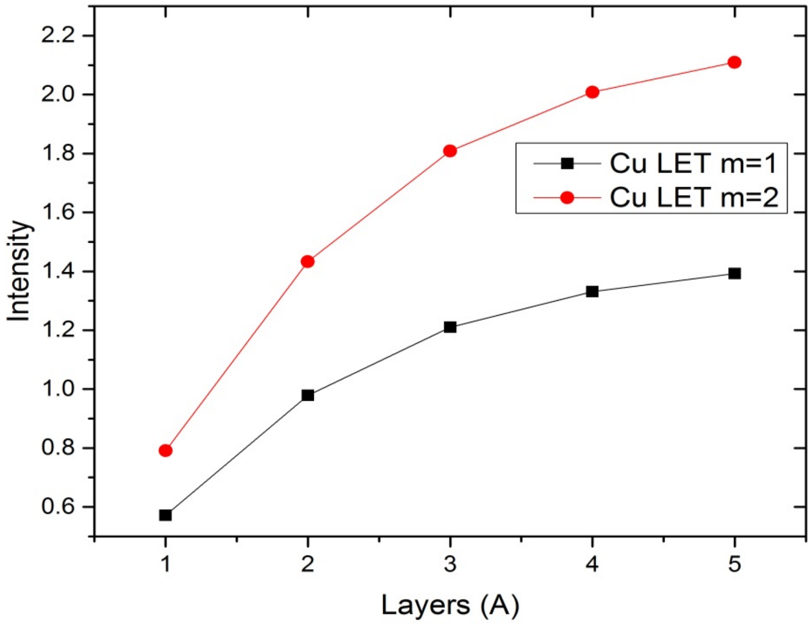

Figure 5-7 Layer contributions to the Cu low energy tail (each layer of thickness 1.8 Å)

For Ag, IMFP of the Auger electron with energy 40eV is λa= 4.16 Å [50], λc= 4.49 Å for 4p core electron energy (at 133 eV) and assuming each layer depth d= 2.04 Å.

The contribution from each layer towards the intensity of the peak and towards the low energy tail due to inelastically scattered electrons will be (from equation 5.8 and equation 5.10).

Table 5-2 Theoretical intensity ratio and layer contributions for Silver

Ag	**Layer1**	**Layer2**	**Layer3**	**Layer4**	**Layer5**	**Total 5 Layers**
I Peak	0.493646	0.120295	0.029314	0.007143	0.001741	0.652139
I LET (m=1)	0.54055	0.35096	0.180908	0.086249	0.039804	1.19847
I LET (m=2)	0.74611	0.55153	0.29431	0.14219	0.066005	1.800158

The ratio I LET/ I Peak = 1.84 (for m=1) and I LET/ I Peak = 2.38 (for m=2).

The ratio of I LET/ I Peak obtained after subtraction of experimentally measured inelastically scattered VB contribution with incident photon energy hv= 180eV is 1.16.

For higher beam energy hv=465eV the I LET/I Peak approximate ratio came out to be 1.28.

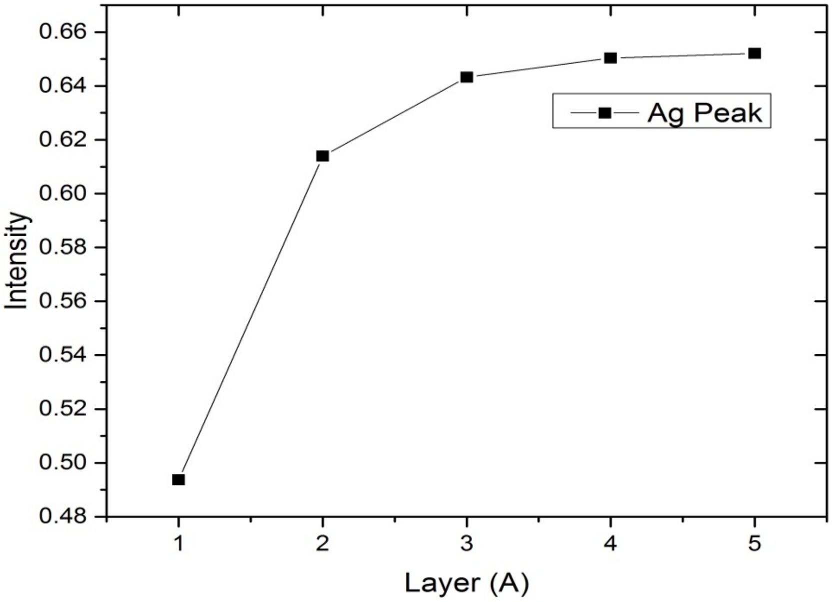

Figure 5-8 Layer contributions to the Ag peak intensity (each layer of thickness 2.04 Å)

From the figure we can observe that the main contribution towards the Auger peak arises from the first and second layer, that is, from the top 10 A of the sample.

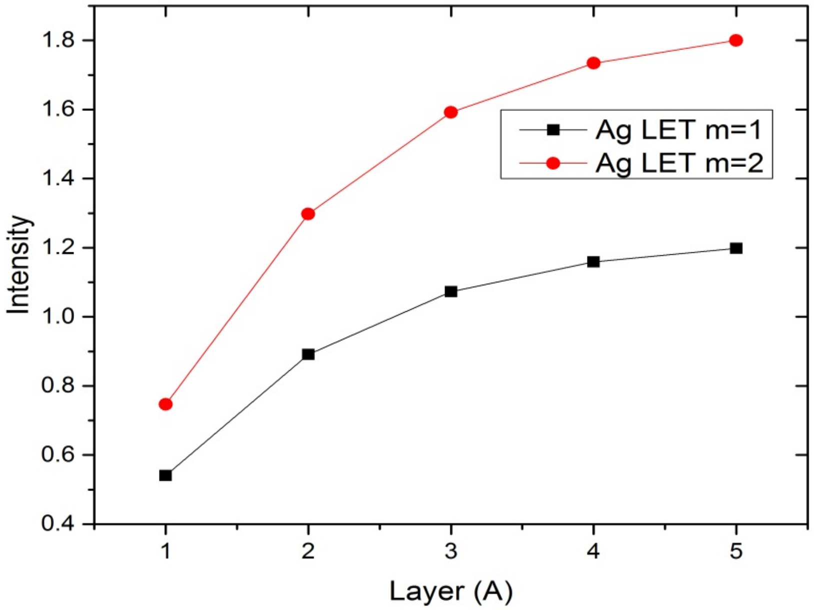

Figure 5-9 Layer contributions to the Ag low energy tail (each layer of thickness 2.04 Å)

5.5 Comparison of Ag APECS with PAES Data

Positron annihilation induced Auger Electron Spectroscopy (PAES) is a highly surface selective and electron induced background free surface analytic technique. The Ag(100) 4p NVV Auger peak obtained from APECS is compared with the Auger spectra obtained using PAES [54-55] (figure 5.10). The blue curve represents the data obtained from PAES and the red curve is from APECS after subtracting the inelastic contribution of the valence band electrons. The PAES peak is wider when compared to the APECS. The reason of this large width is from electron contribution from N_2VV and N_3VV. The degeneracy of N level, spin orbit coupling of N_2 and N_3 and the sensitivity- resolution of the spectrometer are the causal factors of the width.

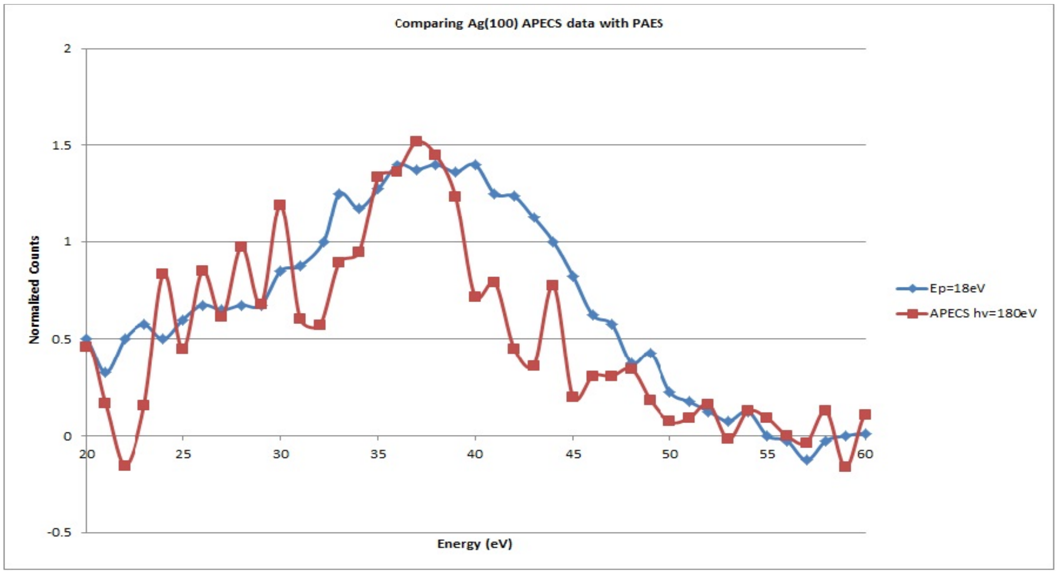

Figure 5-10 Auger peak obtained from APECS is compared with that obtained from PAES (Red curve of APECS shows N_3VV peak whereas the blue curve is N_2VV+N_3VV combination and hence wider).

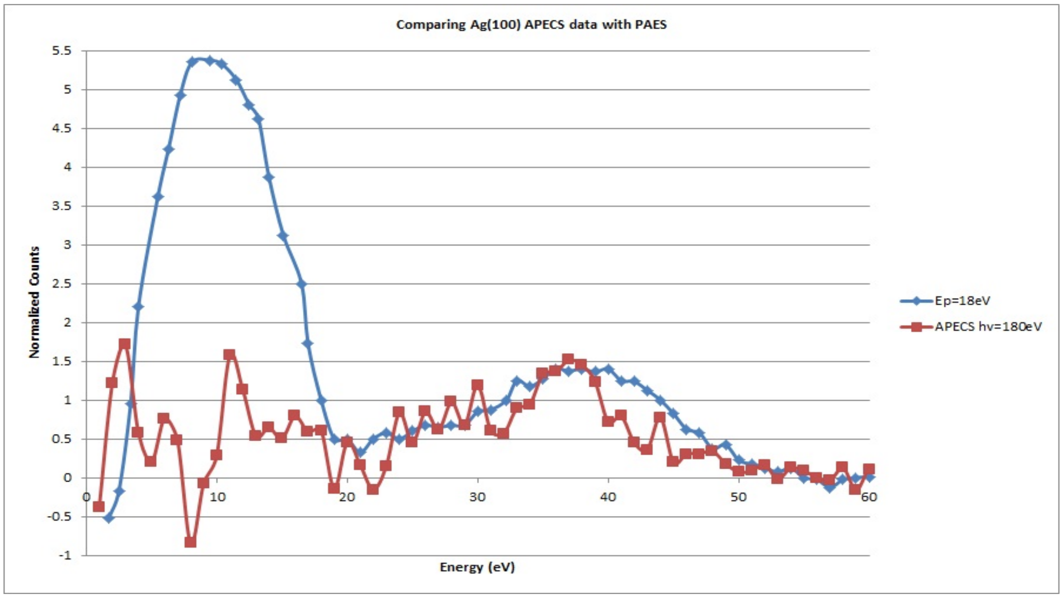

Figure 5-11 The spectrum obtained from APECS is compared with PAES.

In figure 5-11 the full spectrums of Ag(100) APECS are compared with PAES. We observe a high LET peak with the PAES due to beam induced secondary electrons.

Other possible contributions are due to low energy electron contributing via super coster kronig transition, inter band transitions. The PAES data was obtained using a large aperture cylindrical mirror analyzer (CMA) coupled to an electrostatic positron beam. The details of the PAES spectrometer are in reference [54-55].

5.6 Conclusion

In this chapter we compared the experimental data with the theoretical calculations using Tougaard background formula. We also calculated the layer contribution towards LET and the compared the ratio of LET to the Auger peak. The theoretical estimates of the ratio of low energy tail and Auger peak are comparable with the subtracted spectrum’s (I LET/ I Peak) tail to peak ratio at m=1, that is, when inelastically scattered Auger electrons produce one electron.

Chapter 6

Conclusion and Future Work

This concluding chapter summarizes our APECS LET measurements and the theoretical low energy tail intensity calculations. These first of their kind measurements separate the Auger related and Auger unrelated contributions in the low energy tail (down till 0 eV) of the Auger peak were performed on Cu(100) and Ag(100) samples. The Auger peak at low energies of metals is accompanied by a tail of low energy spectral intensity; this contribution obscures the peak of interest and affects the accuracy of the quantitative analysis.

6.1 Conclusion

We used Auger Photoelectron Coincidence Spectroscopy (APECS) to obtain the Auger spectrum of Cu(100) and Ag(100). The APECS measures the Auger spectrum in coincidence with the core energy level and thus discriminating the contributions arising from secondary electrons and electrons arising from the non-Auger transition. Although APECS removes most of the Auger unrelated contributions, it cannot distinguish the contribution which is measured in coincidence with the inelastically scattered valence band electrons emitted at the core energy. To measure this inelastically scattered valence band contribution we did a series of measurements on Ag(100) to study $N_{2,3}VV$ Auger spectrum in coincidence with 4p energy level (in case of Cu(100) to study $M_{2,3}VV$ in coincidence with 3p core) plots summarized in figures 6.1 and 6.2 . The coincidence detection of the core and Auger-valence electrons was achieved by the two cylindrical mirror analyzers (CMAs). One CMA was fixed over a range of energies in between VB and core energy level while other CMA scanned corresponding low energy electrons from 0 to 70eV. The spectrums measured were fit to a parameterized function which was extrapolated to get an estimate of inelastically scattered valence band electrons. The estimated contribution was subtracted for the Ag APECS spectrum to obtain a spectrum solely due to Auger transition with inelastically scattered Auger electron and secondary electrons generated due to Plasmon decay. In the later part of the dissertation we proposed a semi- empirical theoretical model based on the spectral intensity contributions arising from the atomic layers and related with the data obtained from our experiments to estimate Auger related contributions.

Table 6-1 Comparing the Intensity ratio of LET and Auger Peak

I LET/ I Peak	**Experimental subtraction**	**Theoretical Estimate (m=1)**
Cu(100)	2.78	2.02
Ag(100)	1.16 hv=180eV 1.28 hv=465eV	1.83

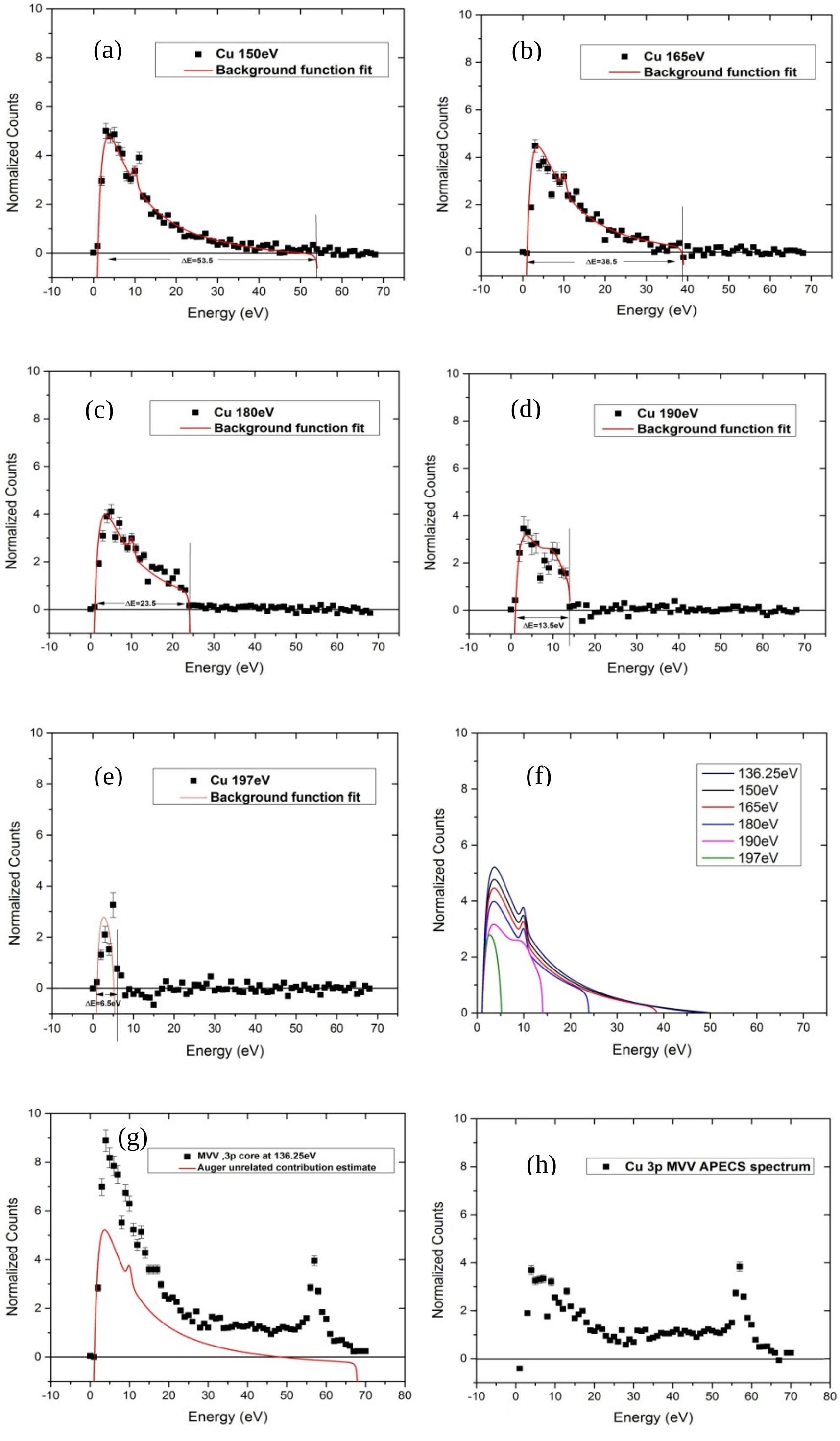

Figure 6-1(a-h) Summary of VB-VB coincidence measurement plots of Cu(100)

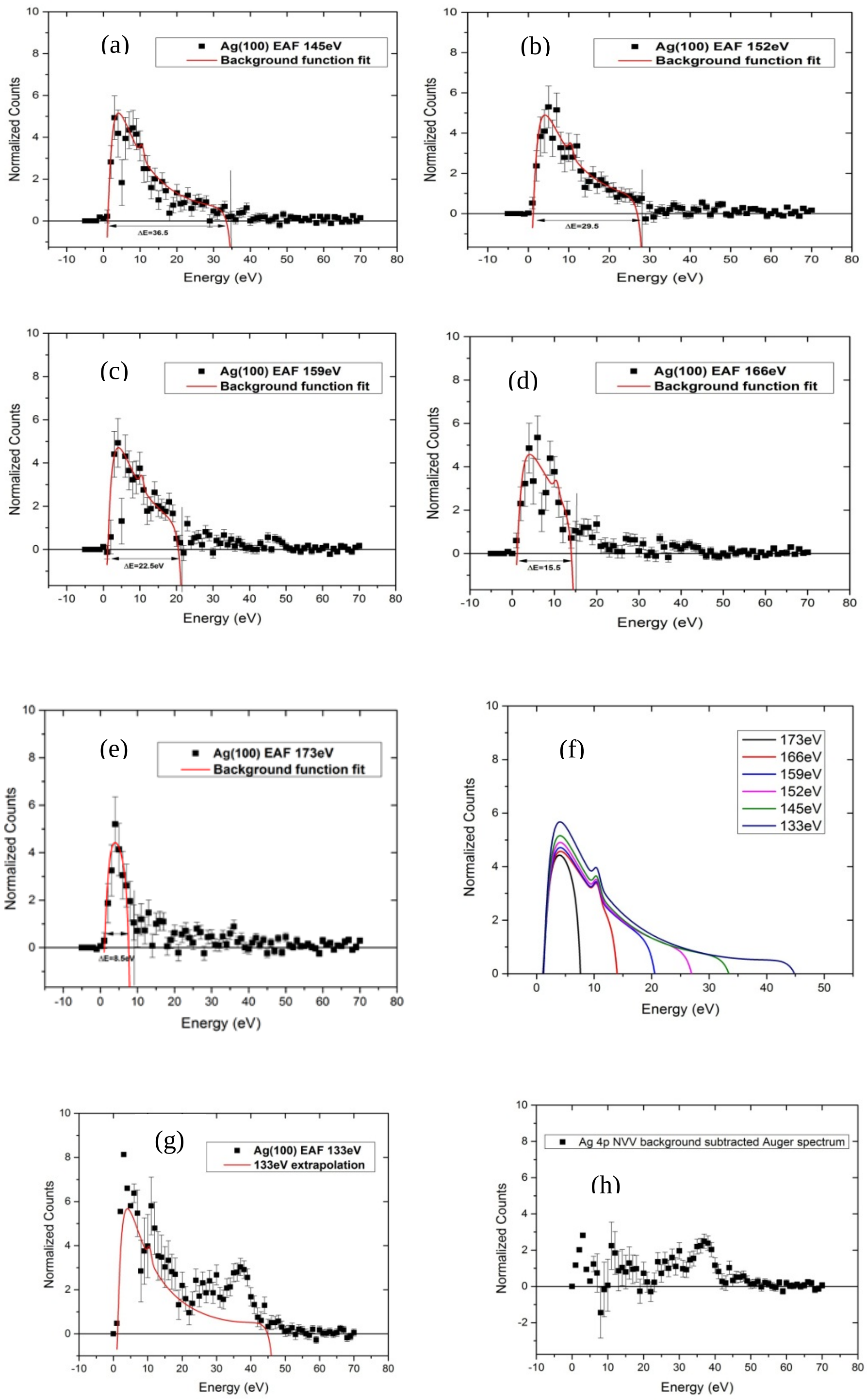

Figure 6-2(a-h) Summary of VB-VB coincidence measurements plots of Ag(100)

6.2 Future Work

6.2.1 VB-VB Coincidence Measurements with Higher Photon Energy

We measured VB-VB coincidence measurement with fixed analyzer at 435eV and using 465eV photon beam energy. The fixed analyzer energies can be chosen in an energy range in between core and valence band (416eV- 465eV). With these measurements we can extrapolate for 4p core energy to get inelastically scattered VB contribution. This contribution can be compared with our low energy beam probe. The inelastic scattering contribution relative to the incident photon beam can be studied.

6.2.2 Coincidence Measurements with Plasmon Loss Peaks

To study the mechanism of electron energy loss, and also to confirm the low energy Plasmon peak at 10eV. The Plasmon contribution arising from the bulk and surface Plasmon contribution can be investigated by taking additional APECS and VB-VB data with higher statistics and with fixed energies set near valence band to probe plasmon loss and plasmon decay processes.

6.2.3 Coincidence Measurements of Au(100) to Study 5p OVV Transition

The VB-VB coincidence measurements on single crystal gold can be carried out to study the low energy tail contribution in transition metals. As the LET contribution also depends on the Auger electron energy, we can establish a relationship by analyzing the data of these metals (Cu, Ag, and Au).

6.2.4 Simulation and Modeling of New High Resolution PAES Spectrometer

At UTA we are constructing a new high resolution, cryo moderated positron beam, time of flight PAES spectrometer [56-57]. We modeled and simulated the charge particle trajectories using SIMION, and the simulations were also done for the current working set up. The simulation work is presented in Appendix D.

Appendix A

Abbreviations

AES	Auger Electron Spectroscopy
AMP	Amplifier
APECS	Auger Photo Electron Coincidence Spectroscopy
BNL	Brookhaven National Laboratory
CFD	Constant Fraction Discriminator
CMA	Cylindrical Mirror Analyzer
CVV	Core Valence Valence
DIMFP	Differential Inelastic Mean Free Path
ERG	Extended Range Grasshopper
IMFP	Inelastic mean free path
IR	Infrared
LEBT	Low Energy Beam Transport
LET	Low Energy Tail
LINAC	Linear Accelerator
MCA	Multi Channel Analyzer
NSLS	National Synchrotron Light Source
PAES	Positron Annihilation Induced Auger Electron spectroscopy
PES	Photo Electron Spectroscopy
PHA	Pulse Height Analyzer
ROI	Region Of Interest
SR	Synchrotron Radiation
TAC	Time to Amplitude Converter
UTA	University of Texas at Arlington

UV	Ultra Violet
VB	Valence Band
VUV	Vacuum Ultra Violet
XPS	X-Ray Photoelectron Spectroscopy

Appendix B

APECS and Related Plots

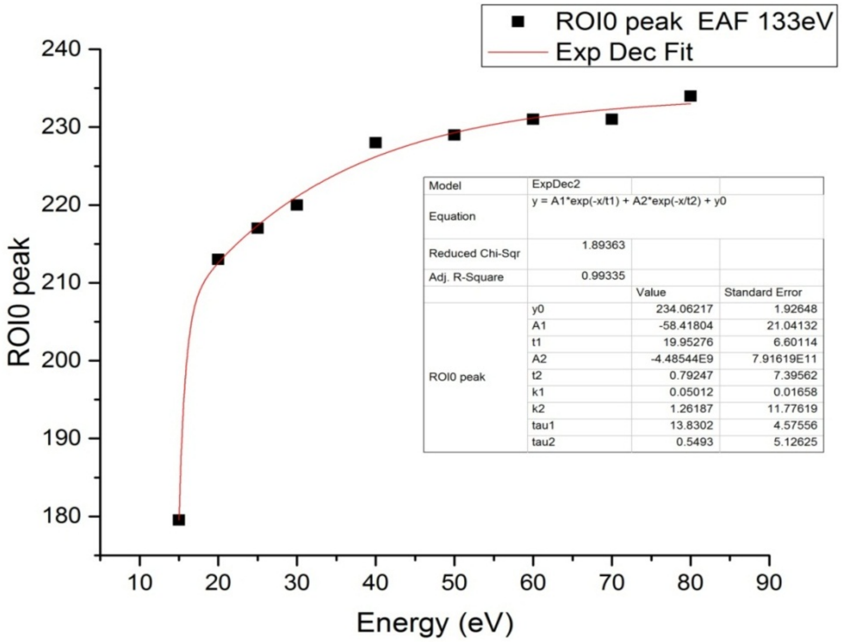

Model	ExpDec2		
Equation	y = A1*exp(-x/t1) + A2*exp(-x/t2) + y0		
Reduced Chi-Sqr	1.89363		
Adj. R-Square	0.99335		
		Value	Standard Error
ROI0 peak	y0	234.06217	1.92648
	A1	-58.41804	21.04132
	t1	19.95276	6.60114
	A2	-4.48544E9	7.91619E11
	t2	0.79247	7.39562
	k1	0.05012	0.01658
	k2	1.26187	11.77619
	tau1	13.8302	4.57556
	tau2	0.5493	5.12625

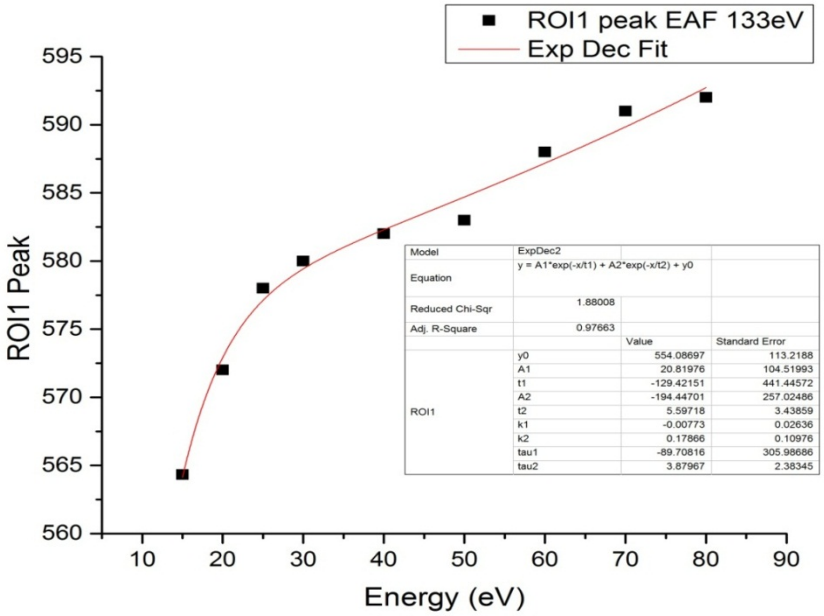

Model	ExpDec2		
Equation	y = A1*exp(-x/t1) + A2*exp(-x/t2) + y0		
Reduced Chi-Sqr	1.88008		
Adj. R-Square	0.97663		
		Value	Standard Error
ROI1	y0	554.08697	113.2188
	A1	20.81976	104.51993
	t1	-129.42151	441.44572
	A2	-194.44701	257.02486
	t2	5.59718	3.43859
	k1	-0.00773	0.02636
	k2	0.17866	0.10976
	tau1	-89.70816	305.98686
	tau2	3.87967	2.38345

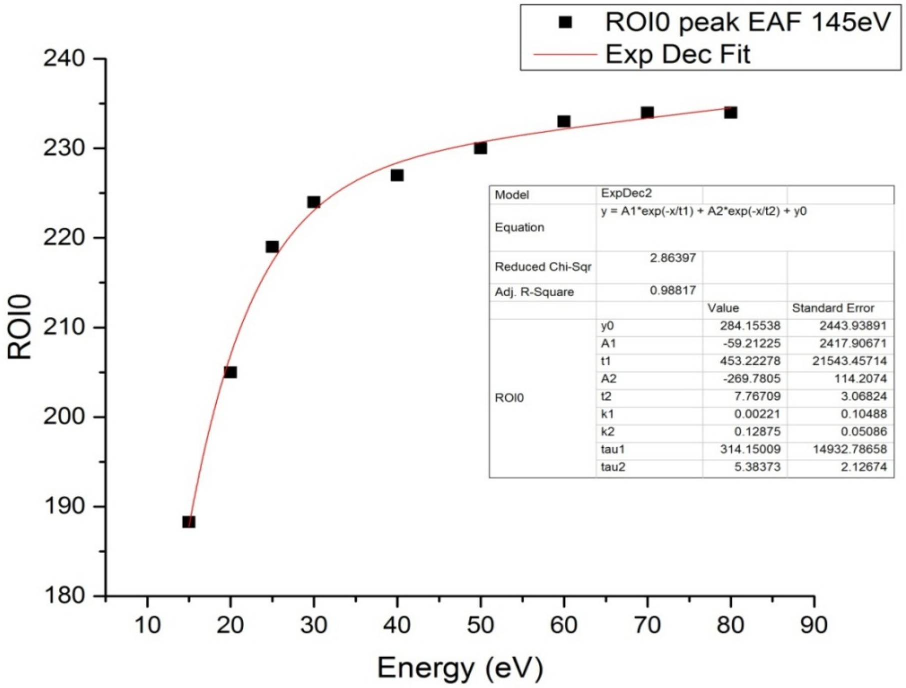

Model	ExpDec2		
Equation	y = A1*exp(-x/t1) + A2*exp(-x/t2) + y0		
Reduced Chi-Sqr	2.86397		
Adj. R-Square	0.98817		
		Value	Standard Error
ROI0	y0	284.15538	2443.93891
	A1	-59.21225	2417.90671
	t1	453.22278	21543.45714
	A2	-269.7805	114.2074
	t2	7.76709	3.06824
	k1	0.00221	0.10488
	k2	0.12875	0.05086
	tau1	314.15009	14932.78658
	tau2	5.38373	2.12674

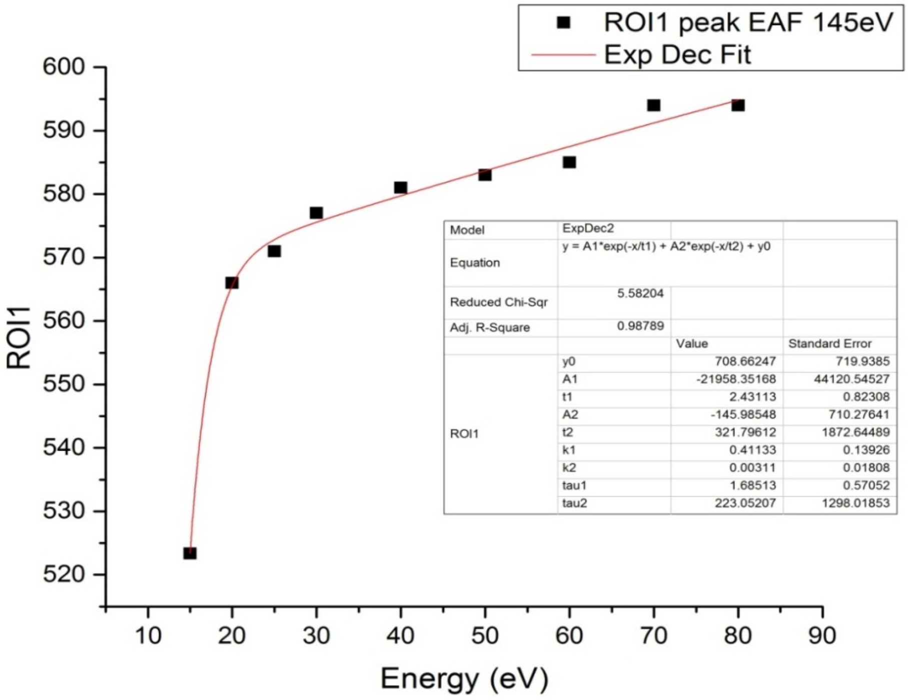

Model	ExpDec2		
Equation	y = A1*exp(-x/t1) + A2*exp(-x/t2) + y0		
Reduced Chi-Sqr	5.58204		
Adj. R-Square	0.98789		
		Value	Standard Error
ROI1	y0	708.66247	719.9385
	A1	-21958.35168	44120.54527
	t1	2.43113	0.82308
	A2	-145.98548	710.27641
	t2	321.79612	1872.64489
	k1	0.41133	0.13926
	k2	0.00311	0.01808
	tau1	1.68513	0.57052
	tau2	223.05207	1298.01853

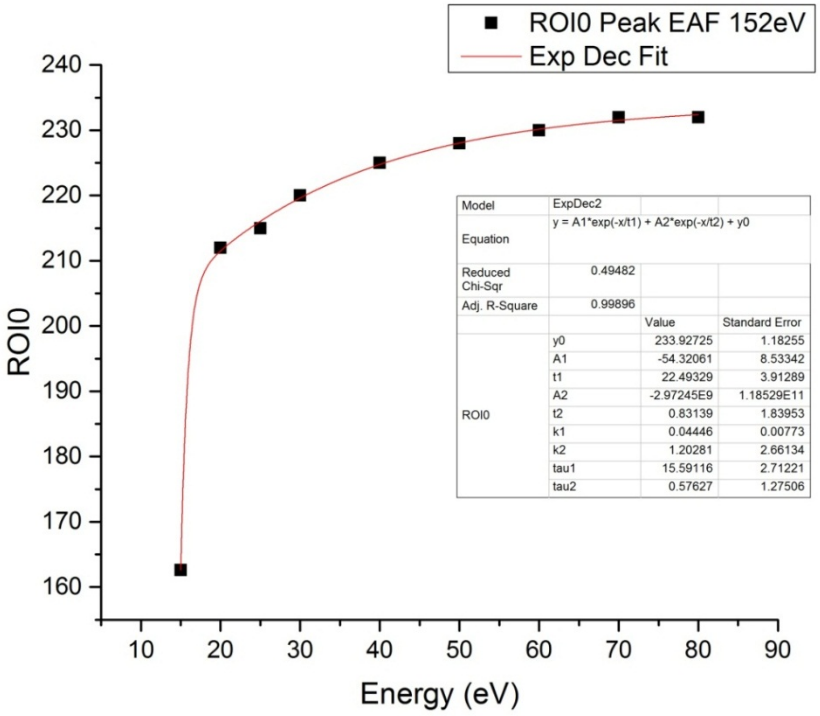
ROI0 Peak EAF 152eV
Exp Dec Fit
ROI0
Energy (eV)
240
230
220
210
200
190
180
170
160
10
20
30
40
50
60
70
80
90
Model | ExpDec2
Equation | y = A1*exp(-x/t1) + A2*exp(-x/t2) + y0
Reduced Chi-Sqr | 0.49482
Adj. R-Square | 0.99896
Value | Standard Error
ROI0
y0 | 233.92725 | 1.18255
A1 | -54.32061 | 8.53342
t1 | 22.49329 | 3.91289
A2 | -2.97245E9 | 1.18529E11
t2 | 0.83139 | 1.83953
k1 | 0.04446 | 0.00773
k2 | 1.20281 | 2.66134
tau1 | 15.59116 | 2.71221
tau2 | 0.57627 | 1.27506

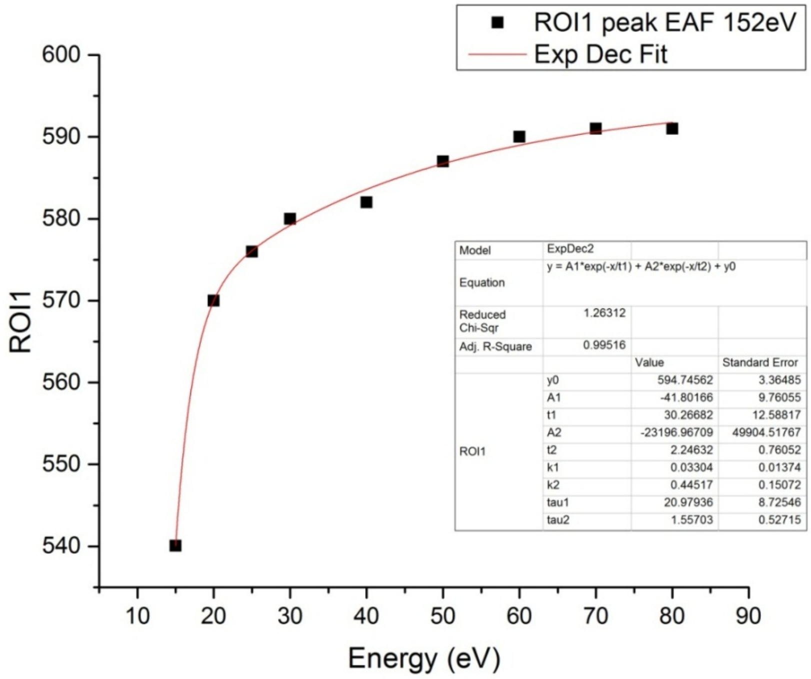
ROI1 peak EAF 152eV
Exp Dec Fit
ROI1
Energy (eV)
600
590
580
570
560
550
540
10
20
30
40
50
60
70
80
90
Model | ExpDec2
Equation | y = A1*exp(-x/t1) + A2*exp(-x/t2) + y0
Reduced Chi-Sqr | 1.26312
Adj. R-Square | 0.99516
Value | Standard Error
ROI1
y0 | 594.74562 | 3.36485
A1 | -41.80166 | 9.76055
t1 | 30.26682 | 12.58817
A2 | -23196.96709 | 49904.51767
t2 | 2.24632 | 0.76052
k1 | 0.03304 | 0.01374
k2 | 0.44517 | 0.15072
tau1 | 20.97936 | 8.72546
tau2 | 1.55703 | 0.52715

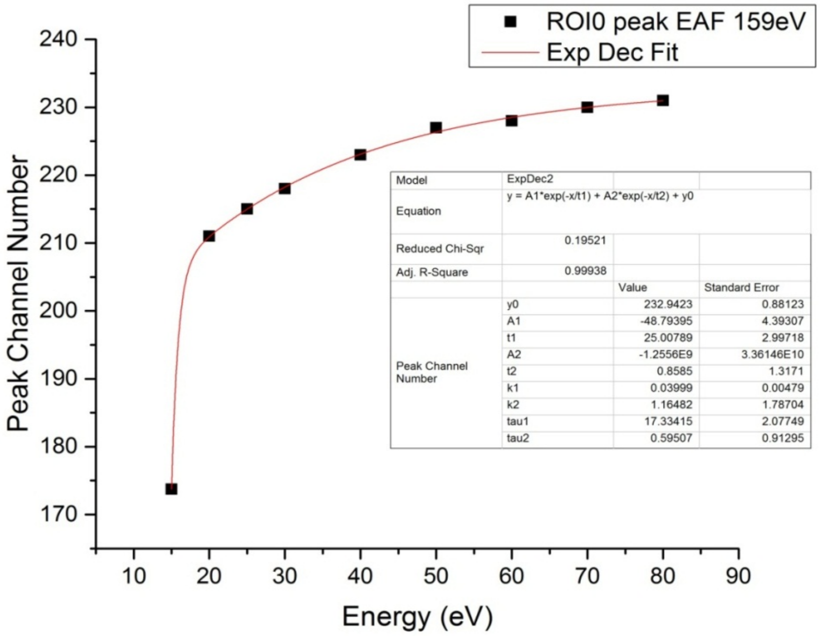

Model	ExpDec2		
Equation	y = A1*exp(-x/t1) + A2*exp(-x/t2) + y0		
Reduced Chi-Sqr	0.19521		
Adj. R-Square	0.99938		
		Value	Standard Error
Peak Channel Number	y0	232.9423	0.88123
	A1	-48.79395	4.39307
	t1	25.00789	2.99718
	A2	-1.2556E9	3.36146E10
	t2	0.8585	1.3171
	k1	0.03999	0.00479
	k2	1.16482	1.78704
	tau1	17.33415	2.07749
	tau2	0.59507	0.91295

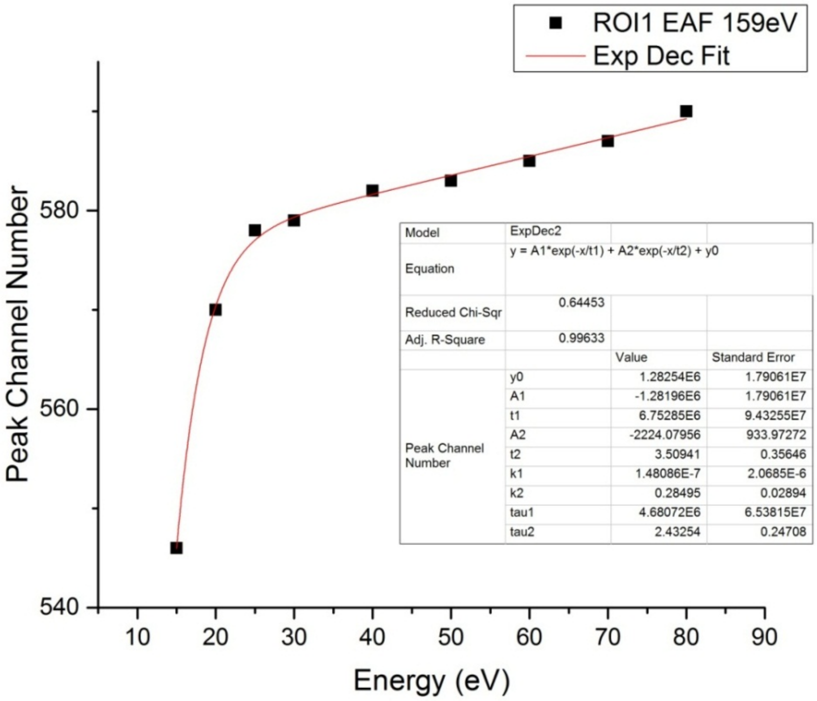

Model	ExpDec2		
Equation	y = A1*exp(-x/t1) + A2*exp(-x/t2) + y0		
Reduced Chi-Sqr	0.64453		
Adj. R-Square	0.99633		
		Value	Standard Error
Peak Channel Number	y0	1.28254E6	1.79061E7
	A1	-1.28196E6	1.79061E7
	t1	6.75285E6	9.43255E7
	A2	-2224.07956	933.97272
	t2	3.50941	0.35646
	k1	1.48086E-7	2.0685E-6
	k2	0.28495	0.02894
	tau1	4.68072E6	6.53815E7
	tau2	2.43254	0.24708

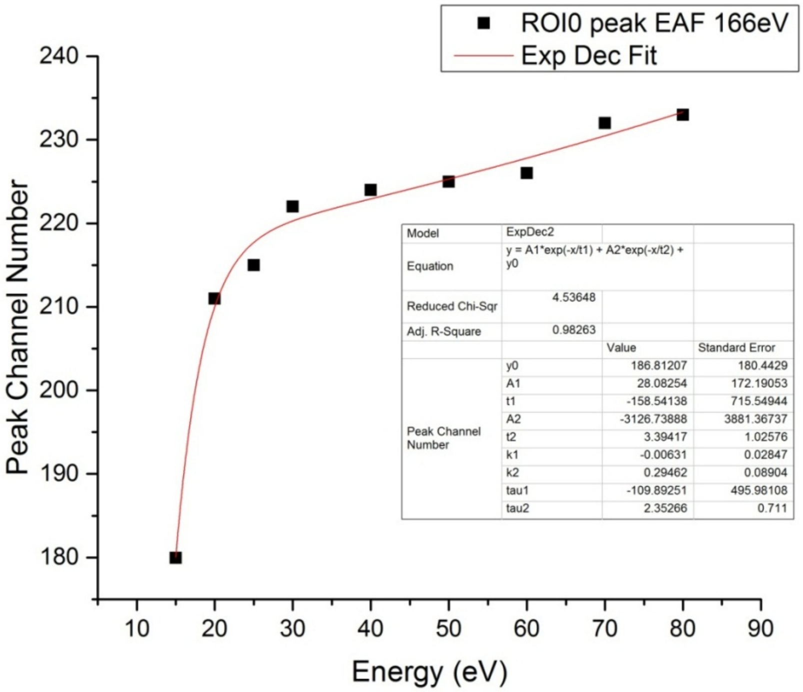

Model	ExpDec2		
Equation	y = A1*exp(-x/t1) + A2*exp(-x/t2) + y0		
Reduced Chi-Sqr	4.53648		
Adj. R-Square	0.98263		
		Value	Standard Error
Peak Channel Number	y0	186.81207	180.4429
	A1	28.08254	172.19053
	t1	-158.54138	715.54944
	A2	-3126.73888	3881.36737
	t2	3.39417	1.02576
	k1	-0.00631	0.02847
	k2	0.29462	0.08904
	tau1	-109.89251	495.98108
	tau2	2.35266	0.711

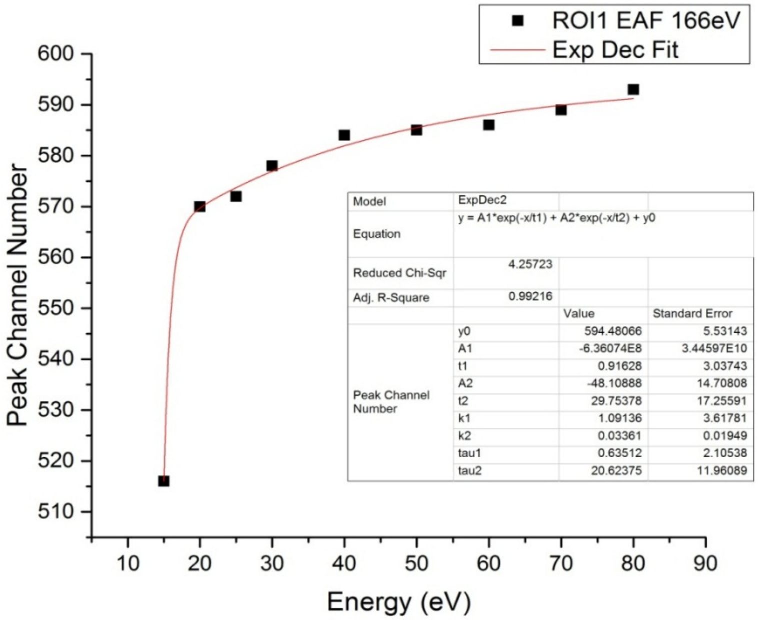

Model	ExpDec2		
Equation	y = A1*exp(-x/t1) + A2*exp(-x/t2) + y0		
Reduced Chi-Sqr	4.25723		
Adj. R-Square	0.99216		
		Value	Standard Error
Peak Channel Number	y0	594.48066	5.53143
	A1	-6.36074E8	3.44597E10
	t1	0.91628	3.03743
	A2	-48.10888	14.70808
	t2	29.75378	17.25591
	k1	1.09136	3.61781
	k2	0.03361	0.01949
	tau1	0.63512	2.10538
	tau2	20.62375	11.96089

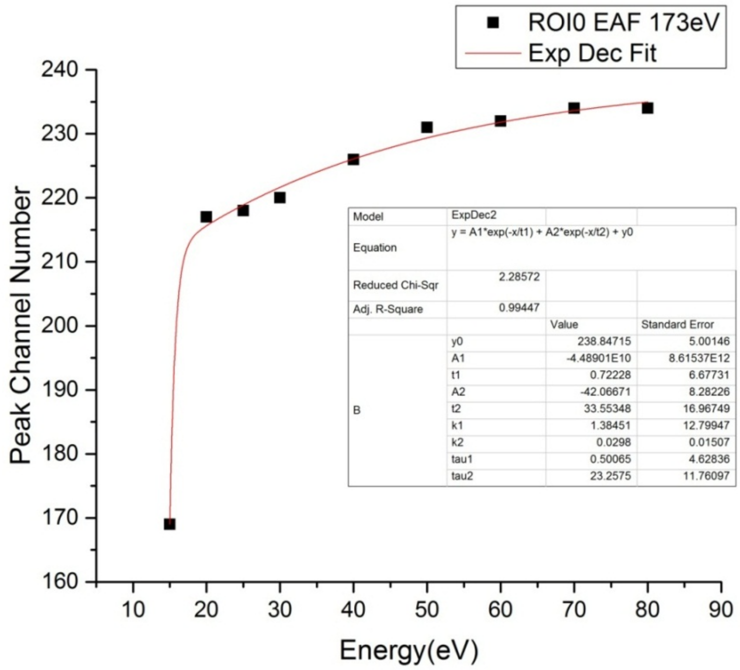

Model	ExpDec2		
Equation	y = A1*exp(-x/t1) + A2*exp(-x/t2) + y0		
Reduced Chi-Sqr	2.28572		
Adj. R-Square	0.99447		
		Value	Standard Error
B	y0	238.84715	5.00146
	A1	-4.48901E10	8.61537E12
	t1	0.72228	6.67731
	A2	-42.06671	8.28226
	t2	33.55348	16.96749
	k1	1.38451	12.79947
	k2	0.0298	0.01507
	tau1	0.50065	4.62836
	tau2	23.2575	11.76097

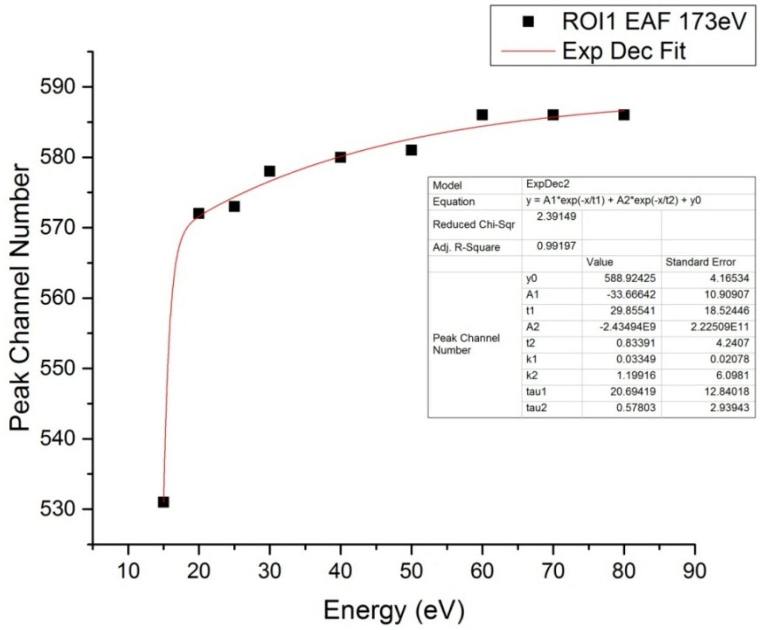

Model	ExpDec2		
Equation	y = A1*exp(-x/t1) + A2*exp(-x/t2) + y0		
Reduced Chi-Sqr	2.39149		
Adj. R-Square	0.99197		
		Value	Standard Error
Peak Channel Number	y0	588.92425	4.16534
	A1	-33.66642	10.90907
	t1	29.85541	18.52446
	A2	-2.43494E9	2.22509E11
	t2	0.83391	4.2407
	k1	0.03349	0.02078
	k2	1.19916	6.0981
	tau1	20.69419	12.84018
	tau2	0.57803	2.93943

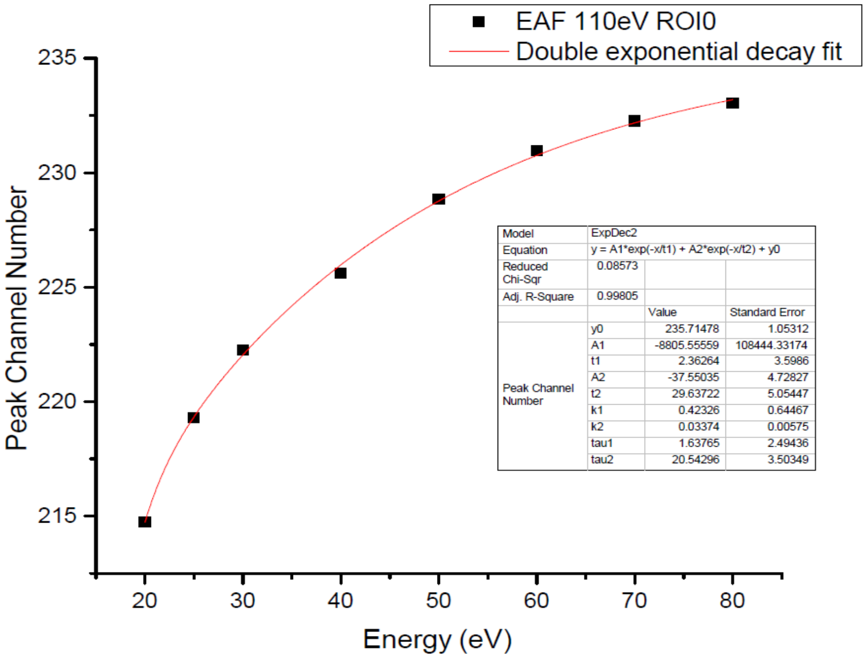

Model	ExpDec2		
Equation	y = A1*exp(-x/t1) + A2*exp(-x/t2) + y0		
Reduced Chi-Sqr	0.08573		
Adj. R-Square	0.99805		
		Value	Standard Error
Peak Channel Number	y0	235.71478	1.05312
	A1	-8805.55559	108444.33174
	t1	2.36264	3.5986
	A2	-37.55035	4.72827
	t2	29.63722	5.05447
	k1	0.42326	0.64467
	k2	0.03374	0.00575
	tau1	1.63765	2.49436
	tau2	20.54296	3.50349

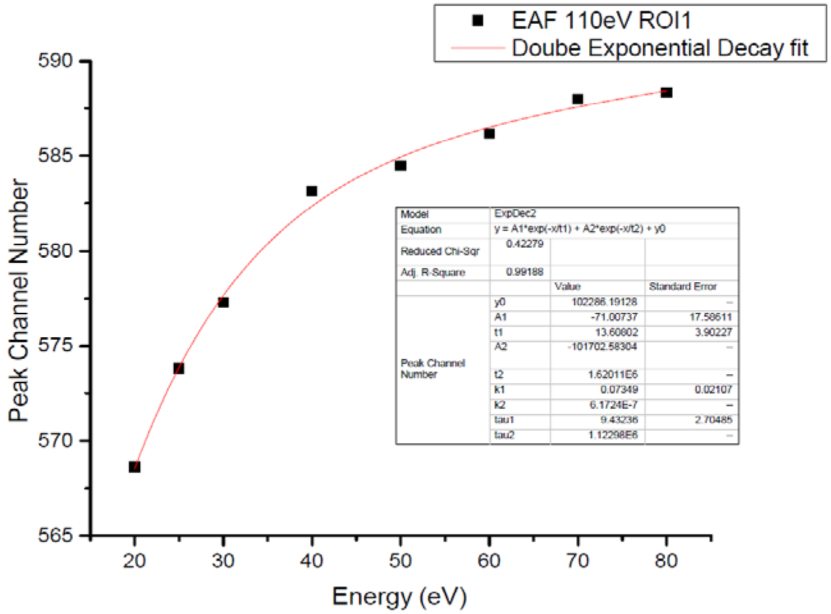

Model	ExpDec2		
Equation	y = A1*exp(-x/t1) + A2*exp(-x/t2) + y0		
Reduced Chi-Sqr	0.42279		
Adj. R-Square	0.99188		
		Value	Standard Error
Peak Channel Number	y0	102286.19128	--
	A1	-71.00737	17.58611
	t1	13.60802	3.90227
	A2	-101702.58304	--
	t2	1.62011E6	--
	k1	0.07349	0.02107
	k2	6.1724E-7	--
	tau1	9.43236	2.70485
	tau2	1.12298E6	--

Parameters

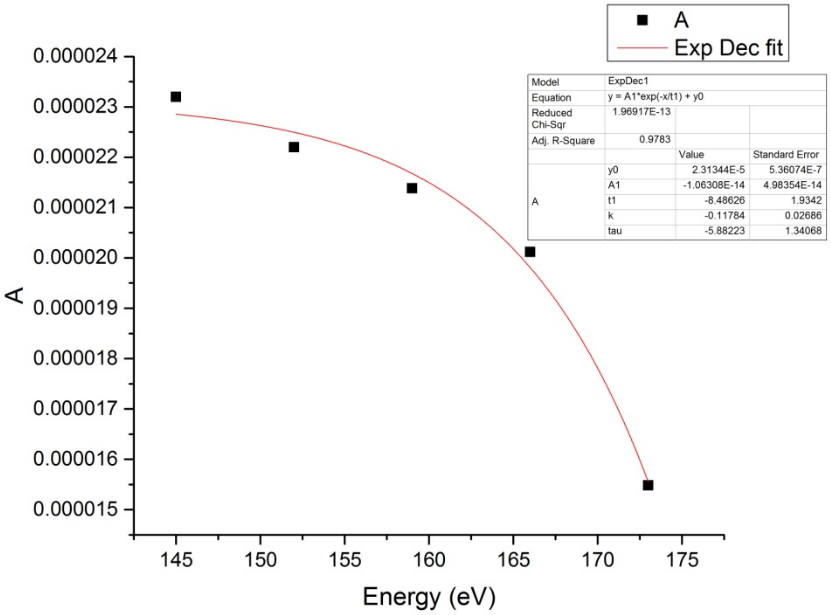

Model	ExpDec1		
Equation	y = A1*exp(-x/t1) + y0		
Reduced Chi-Sqr	1.96917E-13		
Adj. R-Square	0.9783		
		Value	Standard Error
A	y0	2.31344E-5	5.36074E-7
	A1	-1.06308E-14	4.98354E-14
	t1	-8.48626	1.9342
	k	-0.11784	0.02686
	tau	-5.88223	1.34068

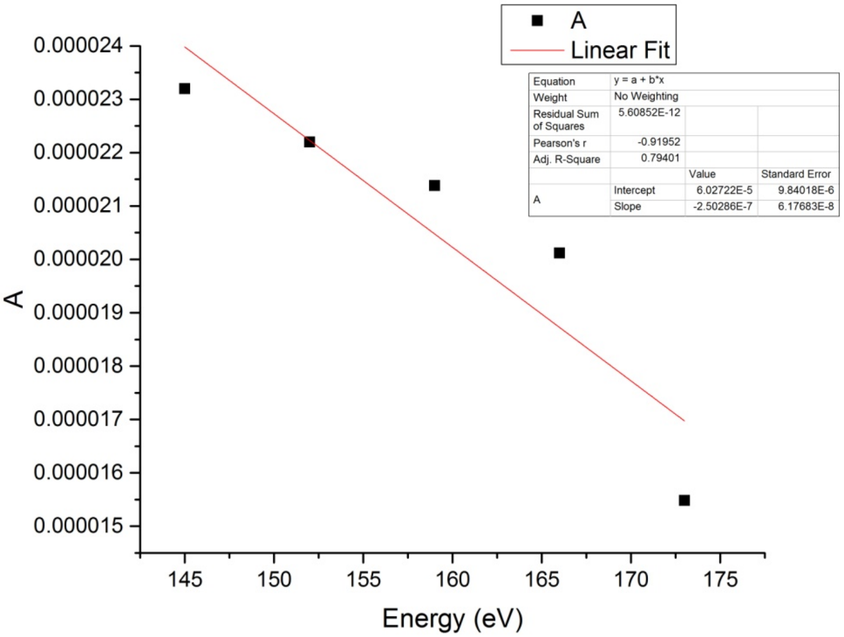

Equation	y = a + b*x		
Weight	No Weighting		
Residual Sum of Squares	5.60852E-12		
Pearson's r	-0.91952		
Adj. R-Square	0.79401		
		Value	Standard Error
A	Intercept	6.02722E-5	9.84018E-6
	Slope	-2.50286E-7	6.17683E-8

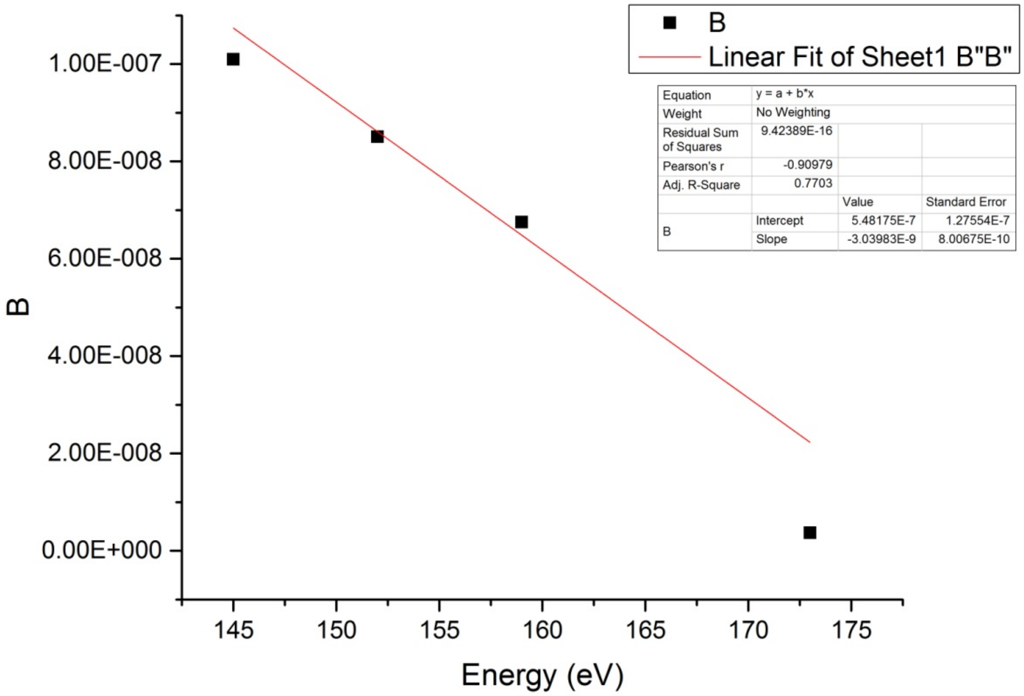

Equation	y = a + b*x		
Weight	No Weighting		
Residual Sum of Squares	9.42389E-16		
Pearson's r	-0.90979		
Adj. R-Square	0.7703		
		Value	Standard Error
B	Intercept	5.48175E-7	1.27554E-7
	Slope	-3.03983E-9	8.00675E-10

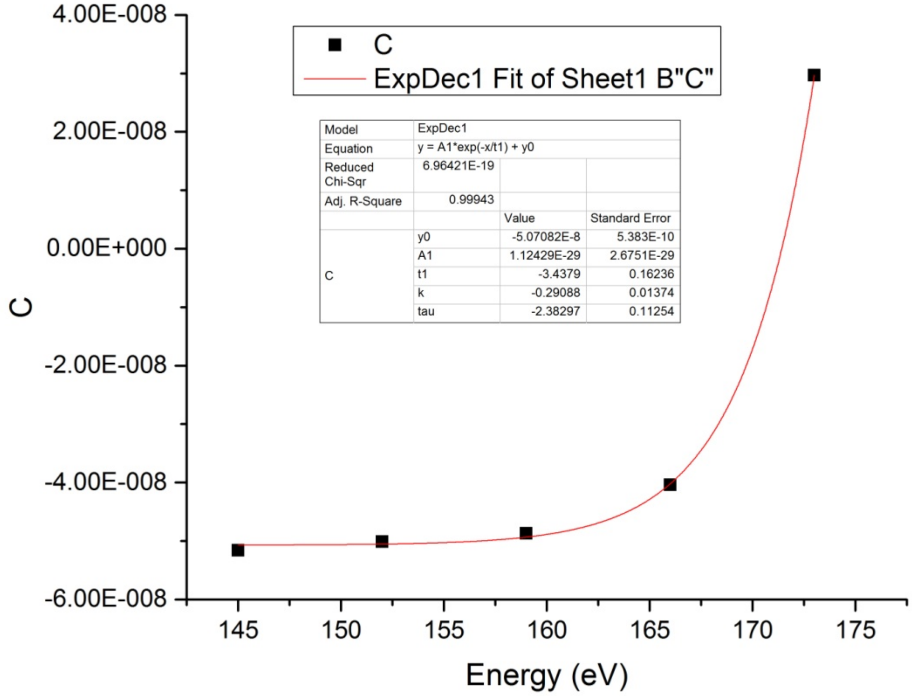

Model	ExpDec1		
Equation	y = A1*exp(-x/t1) + y0		
Reduced Chi-Sqr	6.96421E-19		
Adj. R-Square	0.99943		
		Value	Standard Error
C	y0	-5.07082E-8	5.383E-10
	A1	1.12429E-29	2.6751E-29
	t1	-3.4379	0.16236
	k	-0.29088	0.01374
	tau	-2.38297	0.11254

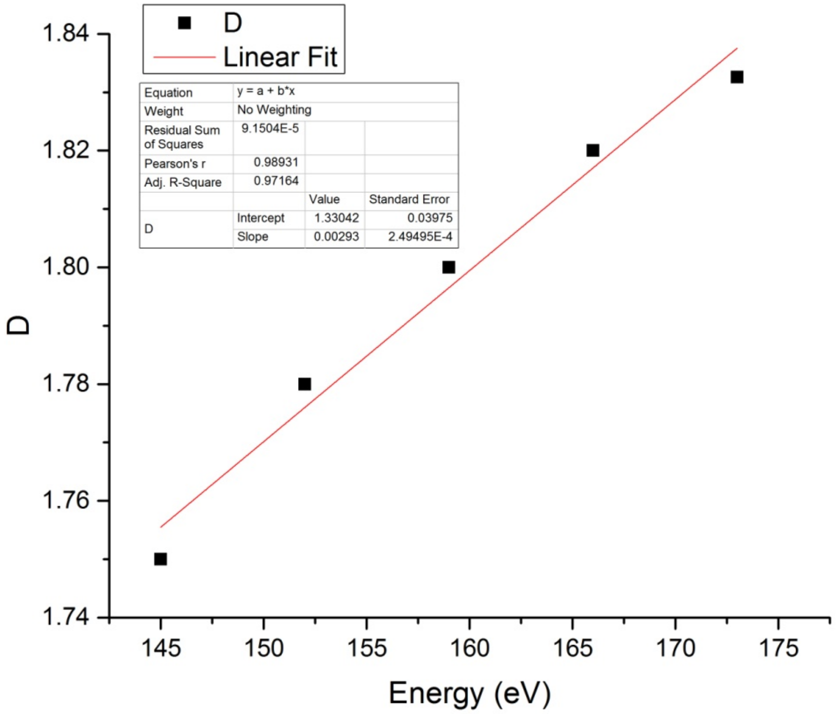

Equation	y = a + b*x		
Weight	No Weighting		
Residual Sum of Squares	9.1504E-5		
Pearson's r	0.98931		
Adj. R-Square	0.97164		
		Value	Standard Error
D	Intercept	1.33042	0.03975
	Slope	0.00293	2.49495E-4

Appendix C

MATLAB Code

Matlab code for extrapolating 133eV data, For other fixed energies the code was same except the ROI0 and ROI1 parameters (yo,A1,A2,t1,t2) used for respective energies refer table 1 and 2 of chapter 3.

```
% Program to extract data
 clear all;
close all;
%-----------------------------------------------------------------%
% File read-in, reads the excel sheet
data=xlsread('133eV_reverseSS.xlsx');
% Curve-fit equation for ROI(0)
y0=309.4;
A1=25874.6098;
t1=2.25674;
A2=33.47414;
t2=36.74182;
% x represents the value of energy i.e.: 10, 11, 12....85
for i=10:1:85
    x(i)=i;
end
% To compute the position of the peak i.e.: ROI0 and ROI1
for j=10:1:85
    y(j)=(((A1*exp(-x(j)/t1)+A2*exp(-x(j)/t2)+y0))*-1)+ 543.799;
end
```

```
% Selecting the range for diff. energy levels by rounding-off y, shifting
% the array by discarding the first 9 zeros
for i=1:1:76
    y_range(i)=round(y(i+9));
    y_range=y_range';
end
 % Selecting ROI(0)
for i=1:1:72
     min(i+4)=y_range(i+4)-26;
    max(i+4)=y_range(i+4)+26;
    sum=0;
    prev_sum=0;
         for row=(min(i+4):1:max(i+4))
            sum=data(row,i+5)+sum;
        end
                for prev_row=(1:1:min(i+4))
            prev_sum=data(prev_row,i+5)+prev_sum;
        end


    ROI0(i+4)=sum;
    previous_sum(i+4)=prev_sum;
end
%-----------------------------------------------------------------%
% Curve-fit equation for ROI(1)
y1=669.82694;
```

```
A3=39.6663;
t3=25.43976;
A4=68429.68275;
t4=1.9723;
 for i=10:1:85
    x2(i)=i;
end
 for j=10:1:85
    y2(j)=(((A3*exp(-x2(j)/t3)+A4*exp(-x2(j)/t4)+y1))*(-1)+1261.819);
end
 % Selecting the range for diff. energy levels by rounding-off y
for i=1:1:76
    y_range2(i)=round(y2(i+9));
    y_range2=y_range2';
end
% Selecting ROI(0)
for i=1:1:72
    min2(i+4)=y_range2(i+4)-26;
    max2(i+4)=y_range2(i+4)+26;
    sum2=0;
    prev_sum2=0;
            for row=(min2(i+4):1:max2(i+4))
            sum2=data(row,i+5)+sum2;
        end
```

```
        for prev_row2=(1:1:min2(i+4))
            prev_sum2=data(prev_row2,i+5)+prev_sum2;
        end
    ROI1(i+4)=sum2;
    previous_sum2(i+4)=prev_sum2;
end
%-----------------------------------------------------------------%
 % Taking difference of ROI(0)-ROI(1)
for i=1:1:76
    diff(i)=ROI0(i)-ROI1(i);
end
plot(diff);
```

For high energy photon beam hv= 465eV and for the fixed energies 110eV, 416eV and 435eV the MCA data matrix was different, hence the ‘for loop’ modified in the code below.

```
% Program to extract data
clear all;
close all;
%-----------------------------------------------------------------%
% File read-in
data=xlsread('EAF416_R635.xlsx');
% Curve-fit equation for ROI(0)
y0=227.51672;
A1=-54.17433;
t1=19.37723;
A2=-2.66053E6;
t2=1.37544;
 % x represents the value of energy i.e.: 10, 11, 12....85
for i=10:1:85
   x(i)=i;
end
 % To compute the position of the peak i.e.: ROI0 and ROI1
for j=10:1:85
   y(j)=((A1*exp(-x(j)/t1)+A2*exp(-x(j)/t2)+y0));
end
```

```
% Selecting the range for diff. energy levels by rounding-off y, shifting
% the array by discarding the first 9 zeros
for i=1:1:66
    y_range(i)=round(y(i+9));
    y_range=y_range';
end
 % Selecting ROI(0)
for i=1:1:62
       min(i+4)=y_range(i+4)-26;
    max(i+4)=y_range(i+4)+26;
    sum=0;
    prev_sum=0;
           for row=(min(i+4):1:max(i+4))
            sum=data(row,i+5)+sum;
        end

        for prev_row=(1:1:min(i+4))
            prev_sum=data(prev_row,i+5)+prev_sum;
        end

    ROI0(i+4)=sum;
    previous_sum(i+4)=prev_sum;
end
%-----------------------------------------------------------------%
```

```
% Curve-fit equation for ROI(1)

y1=583.15497;

A3=-50.29354;

t3=22.13653;

A4=-1.78166E6;

t4=1.42581;

 for i=10:1:85

    x2(i)=i;

end

 for j=10:1:85

    y2(j)=((A3*exp(-x2(j)/t3)+A4*exp(-x2(j)/t4)+y1));

end

 % Selecting the range for diff. energy levels by rounding-off y

for i=1:1:66

    y_range2(i)=round(y2(i+9));

    y_range2=y_range2';

end

 % Selecting ROI(0)

for i=1:1:62

      min2(i+4)=y_range2(i+4)-26;

    max2(i+4)=y_range2(i+4)+26;

    sum2=0;

    prev_sum2=0;

            for row=(min2(i+4):1:max2(i+4))

            sum2=data(row,i+5)+sum2;
```

```
        end
        for prev_row2=(1:1:min2(i+4))
            prev_sum2=data(prev_row2,i+5)+prev_sum2;
        end
          ROI1(i+4)=sum2;
    previous_sum2(i+4)=prev_sum2;
end
%----------------------------------------------------------------%
 % Taking difference of ROI(0)-ROI(1)
for i=1:1:66
    diff(i)=ROI0(i)-ROI1(i);
end
 plot(diff);
```

Appendix D

SIMION Simulations

Simulation and Modeling of Charge Particle Transport in Time of Flight Positron Annihilation Induced Auger Electron spectroscopy system.

Time of flight- Positron Annihilation Induced Auger Electron Spectroscopy (TOF-PAES) system, a highly surface selective analytical technique using time of flight of auger electron resulting from the annihilation of core electrons by trapped incident positron in image potential well. We simulated and modeled the trajectories of the charge particles in TOF-PAES using SIMION for the development of new high resolution system at U T Arlington and for current TOFPAES system. Here we present our simulations results, Time of Flight calculations and larmor radius calculations for electrons emerging from the sample in current system as well as new system.

D.1 Introduction

The PAES setup uses time of flight technique to obtain the electron energy spectrum. TOF-PAES a highly surface selective and background free technique utilizes the annihilation of the positrons trapped in the image potential well at the sample surface with the core electrons. The annihilation creates a core vacancy causing an imbalance of the atomic charge. The electrons from the valence band fill the core vacancy with giving off the excess energy to the neighboring valence electrons which are emitted out as the Auger electrons. The positrons are generated by the beta decay of Na22 leaving a neutrino, electrons and Ne22. The positron beam is electromagnetically guided using axial magnetic field and perpendicular electric field toward the sample. As the positrons reach towards the sample they get trapped in the image potential well at the surface and annihilate with the core electrons at the surface (~5 A), the signal measured comes for the top most layers of the sample. The spectrum obtained is free of the secondary electron background when compared to electron Auger electron spectroscopy

(EAES), as in PAES the positron beam is used to probe the sample creates no secondary electrons due to annihilation whereas when electron beam is used as the probe it creates a cascade of core electrons and inelastically scattered and backscattered electron influencing the Auger spectrum.

The Time of Flight (TOF) technique effectively differentiates electrons emerging from the sample on the basis of their energy. The electrons with different energies have different drift speed. The electrons travel in electric field free region of a cylindrical tube of length ‘ l’ called as time of flight tube. Time of Flight tube consist of two concentric cylinders. The inner tube 2 m in length and 2 inch dia, has a uniform retarding potential of +/- 1000 V. The outer cylinder is vacuum chamber (beam) and is grounded. Charged particles (electrons and positrons) are either accelerated or decelerated at the TOF tube entrance. In the tube they travel with at a constant speed in the field free central region and after leaving the tube, particles recover their initial speed. As the particles spend most of the time in TOF tube, this increases the energy resolution.

When electrons of mass m_e travelling in the electric field free region for a length ‘l’ (meters) the time of flight t (sec) is given by,

$$t = l\,\frac{m_e}{p} = l\sqrt{\frac{m_e}{2E}},$$

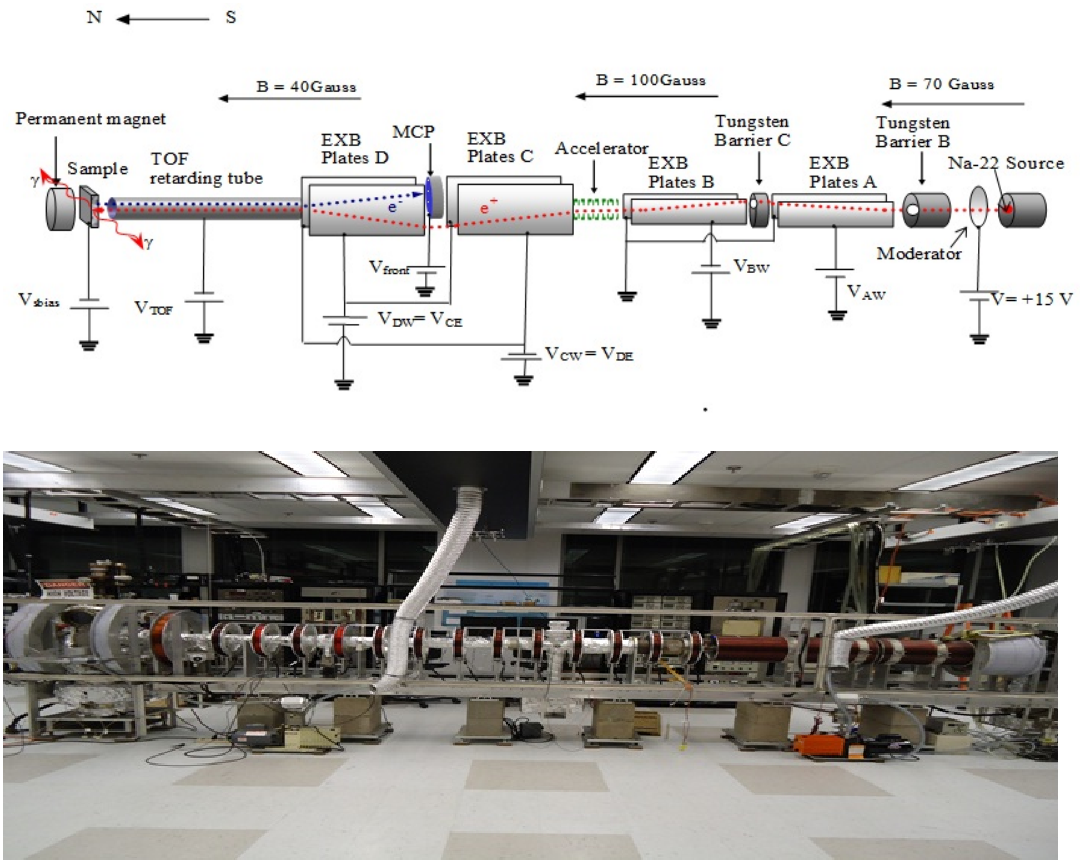

Figure D-1 TOF PAES setup

The positrons travel through 4 sets of E X B plates, tungsten barrier and TOF retarding tube. The first two EXB plates and the tungsten barrier as as energy filters, they filter out fast high energetic electrons and positrons along with gamma rays coming from the source. The beam of mono energetic positron beam gets selected by voltages on EXB plates. The third and fourth set of EXB plates guide the secondary electron towards the electron detector (Micro Channel Plate- MCP) also allowing the incident positron beam to avoid the MCP. The upward and downward deflection is realized using Lorentz Force produced by electric field plates and axial magnetic field.

$$\mathbf{F} = q(\boldsymbol{E} + \boldsymbol{V} \times \boldsymbol{B}), \tag{D.1}$$

D.2 SIMION Basics

To simulate the charge particle trajectory we used SIMION software. SIMION is an ion optics simulation program. Potential Arrays (PA’s) are used to define the geometry of the system (electrodes, and magnetic poles). Potential between electrodes is calculated by solving Laplace's equation by finite difference method (this process is known as refining). Refined PA’s can be positioned as potential array instances (3D virtual images) into an ion optics workbench volume. Ions particles trajectories are simulated by user set parameters in a workbench volume.

User sets initial energy, electric and magnetic potentials source coordinates, velocity direction and components. SIMION computes Electrostatic, Magnetic force and acceleration by numerical integration methods (finite difference method and Runge-Kutta method) [58].

D.3 SIMION Simulations

In the figures D.2, D.3, the charge particle travelling in EM field is simulated.

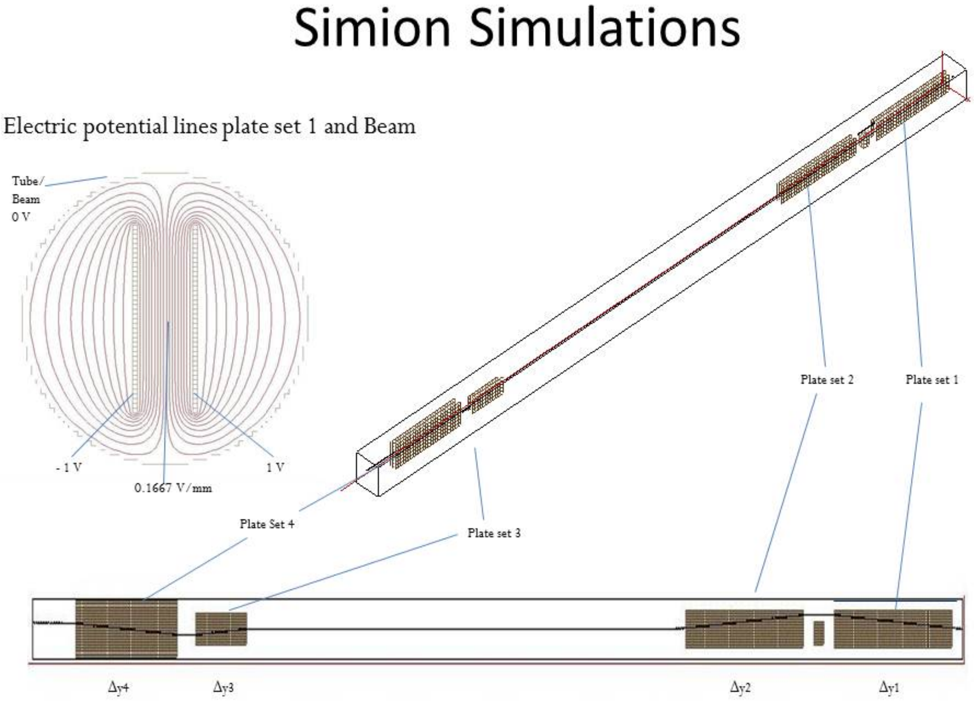

Figure D-2 Beam deviation and electric field lines between parallel palates

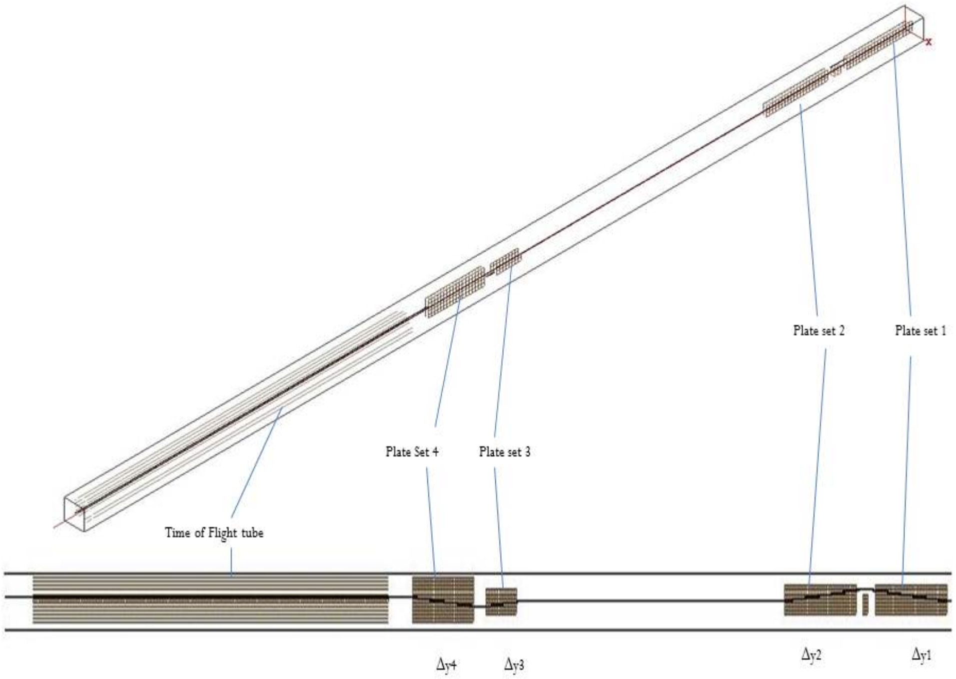

Figure D-3 Beam transport through EXB plates and TOF tube

The charge particle beam transport through various electric potential and magnetic field across EXB plates with respect to beam energy was studied with these simulations. The beam deflection was calculated and compared with the theoretical estimate. We further studied the beam distortion from each plates, and also measured time of flight for various electrons coming out from sample with various take off angles and reaching the detector.

The theoretical beam deflection, delta y, was calculated using,

$$\Delta y = \frac{E\ X\ B}{B^2} * \frac{L}{\sqrt{{V_i}^2 - \frac{2\,e\,v(x)}{m}}} , \qquad \text{(D.2)}$$

Here, E is the electric field, B is the magnetic field, L is the length of EXB plates, e and m are the charge and mass of the particles (electrons/positrons) respectively. Vi is the initial velocity-calculated using initial kinetic energy and v(X) is the potential between the plates of voltage V1 and V2 which is given by,

$$v(x) = \frac{(V1 - V2)x}{d} + \frac{\mathrm{V1+V2}}{2}, \tag{D.3}$$

The beam deflection was found out to be,

Table D-1 Beam deflection across first set of EXB plates

	Simion	**Calculated**
Δy_1	14.34 mm	10.39 mm
Δy_2	13.96 mm	8.01 mm
Δy_3	6.48 mm	6.9 mm
Δy_4	12.13 mm	11 mm

The time of flight measured for electrons to reach from sample surface to the detector. We measured TOF for various take off angles form 0-85°, few are shown in the figures below.

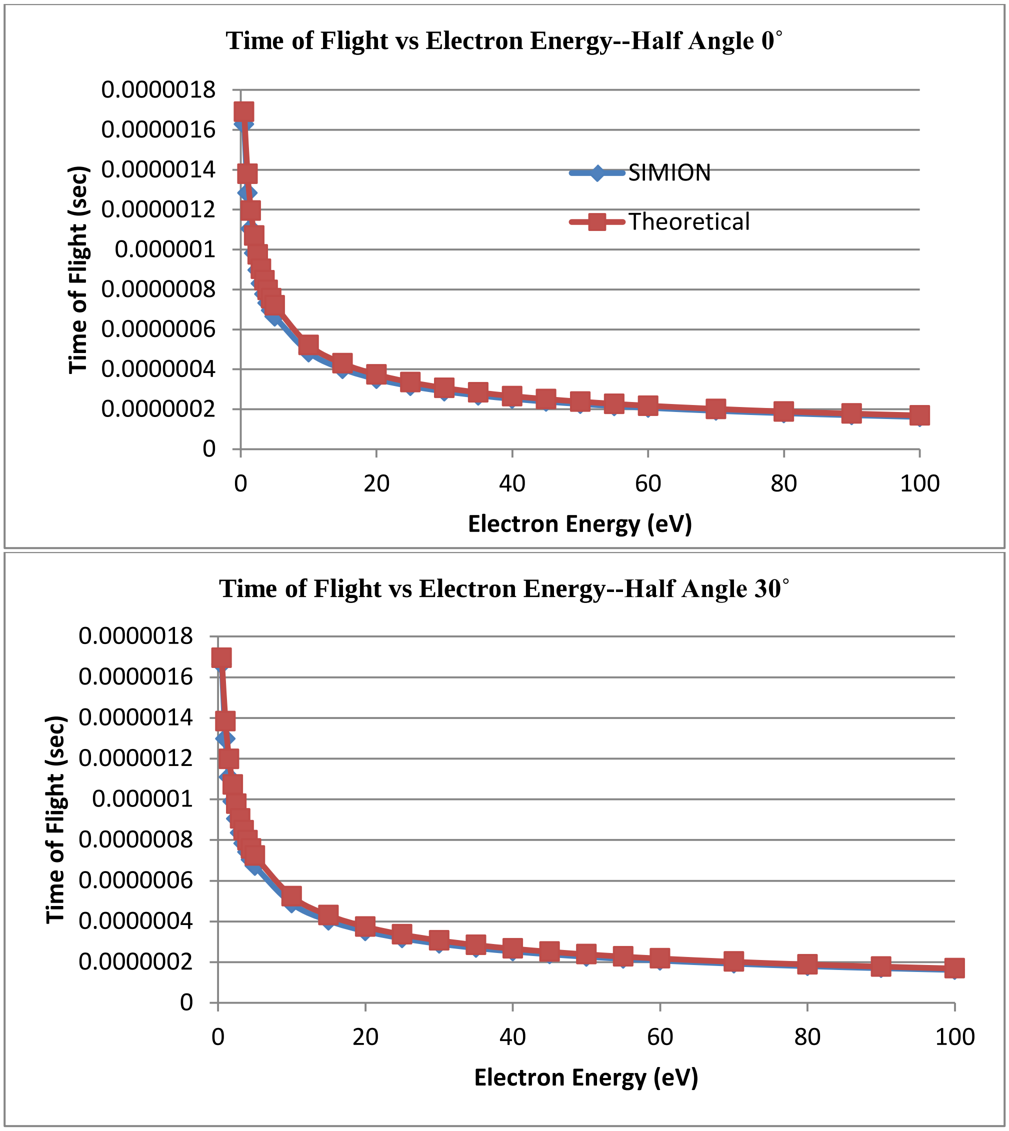

Figure D-4 TOF vs electron energies for various take off angles

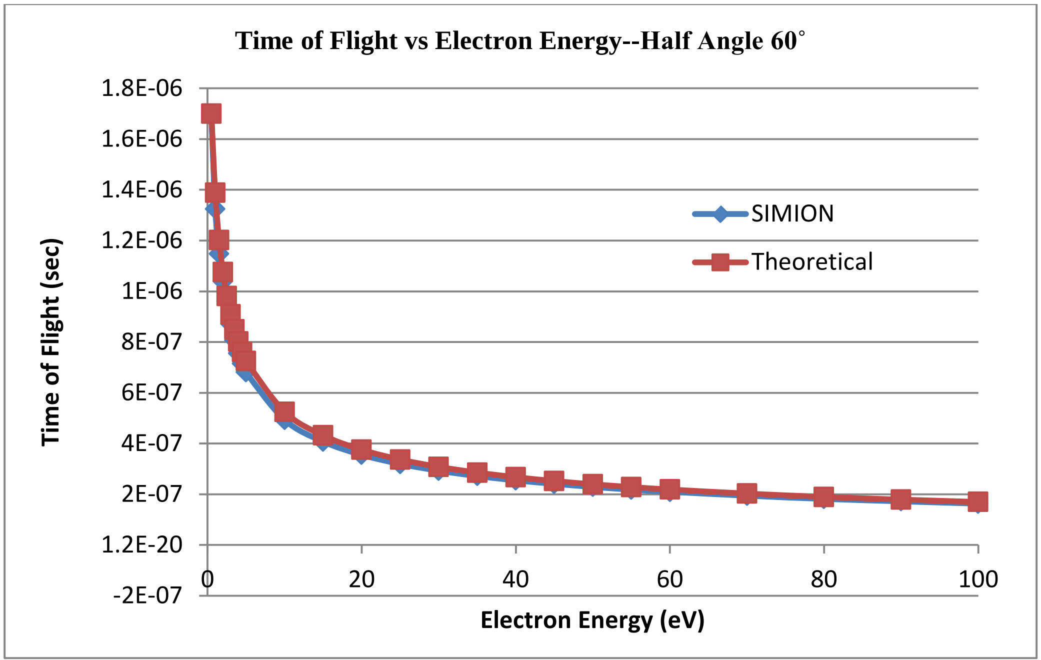

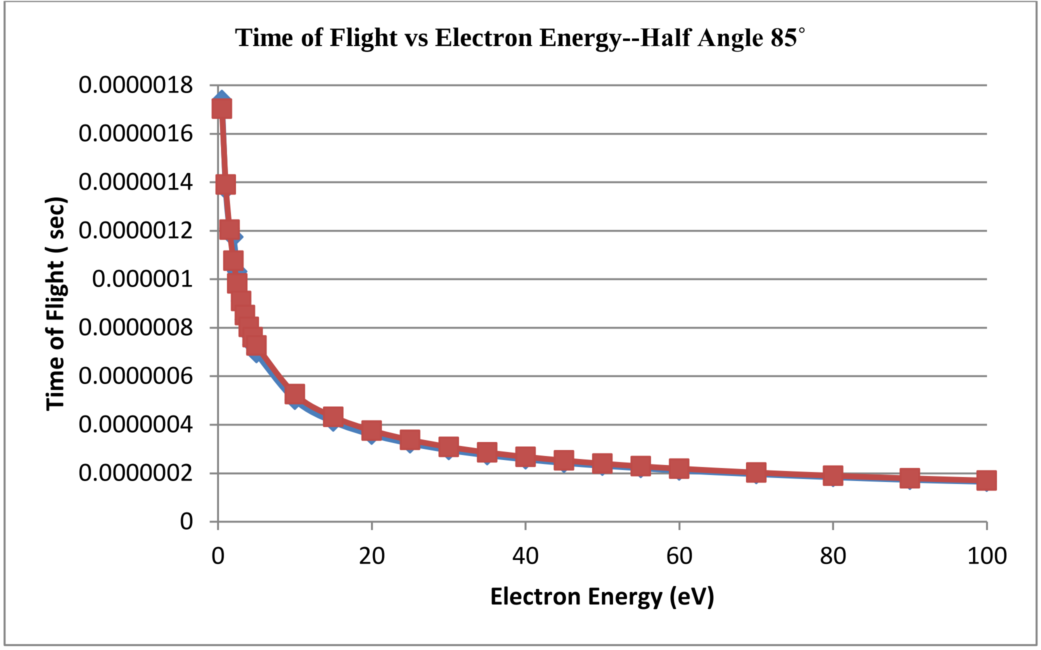

Figure D-5 TOF vs electron energies for various take off angles

Lua code used in SIMION for generating axial magnetic field of 40 Gauss

```
simion.workbench_program()
adjustable bx = 0 -- Gauss
adjustable by = 0 -- Gauss
adjustable bz = 40 -- Gauss
function segment.mfield_adjust()
  ion_bfieldx_gu = bx
  ion_bfieldy_gu = by
  ion_bfieldz_gu = bz
  ion_bfieldx_gu = -(((ion_px_abs_gu-50)/2)*((2.40808*10^-19)/4.96007) * (math.exp((ion_pz_gu - 298.28275) / 4.96007)))
  ion_bfieldy_gu = -(((ion_py_abs_gu-50)/2)*((2.40808*10^-19)/4.96007) * (math.exp((ion_pz_gu - 298.28275) / 4.96007)))
  ion_bfieldz_gu = (40 + ((2.40808*10^-19) * (math.exp((ion_pz_gu - 298.28275) / 4.96007))))
end
```

References

[1] E Jensen et al Physical Review B vol 45, Number 23, (1992)

[2] S Satyal, P Joglekar et al, Journal of Electron spectroscopy and related phenomenon, (May 2014)

[3] H.W. Haak, G.A. Sawatzky and T.D. Thomas, Physical Rev Letters 41,1825 (1978)

[4] R Bartynski et al, Progress in Surface Science, Vol 53, Nos 2-4, pp 155-162 (1996)

[5] R Bartynski et al., Physica Scripta Vol. T41, 168-174 (1992)

[6] S. M. Thurgate, C.P. Lund, J. Elec. Spec. Relat. Phenom. 72, 289-297 (1995)

[7] M T Butterfield et. al, Physical Review B 66, 1151115 (2002)

[8] D. A. Arena et al, Physical Review B, volume 63, 155102 (2001)

[9] Sushant Kalaskar Master's Thesis, UTA (2010)

[10] S Satyal Master's Thesis, UTA (2011)

[11] R Nayak Master's Thesis, UTA (1999)

[12] M Davies et al, Physical Review B Volume 29, Number 10 (1984)

[13] Briggs and Seah, Practical Surface Analysis, 2nd edition, Volume 1 J Wiley and sons (1983,1990)

[14]. X Ray Dat Booklet, Center for X Ray optics and Advanced light source, LBNL, Oct (2009)

[15] Rajalakshmi Sundaramoorthy Phd dissertation (2007)

[16] W D Duncan and G Willams, Applied Optics, **22,** 2914, (1983)

[17] Herman Winick and S Doniach, Synchrotron radiation research (1980)

[18] Robert Bachrach, Synchrotron radiation research (1992)

[19] C Kunz, Synchrotron radiation (1979)

[20] H.W. Haak and G.A. Sawatzky et. al., Rev.Sci.Instrum.55, 696,(1984)

[21] S Thurgate et.al., Rev.Sci. Instrum.61 (12), (1990)

[22] C. J .Powell, Phys Rev. Lett. 38,1429 (1977)

[23] http://www.nsls.bnl.gov/facility/accelerator/vuv/-VUV RING

[24] http://www.nsls.bnl.gov/facility/accelerator/vuv/vuv_parameters.pdf NSLS VUV ring parameters.

[25] http://www.nsls.bnl.gov/facility/accelerator/xray/-X-ray ring

[26] S L Hulbert et. al. Nuclear Instrum. 1 208, 43 (1983)

[27] E Jensen et al, Review of Scientific Instruments 63, 3013-26 (1992)

[28] P Martin , Handbook of Deposition Technologies for films and coatings. Science, Application and Technologies, Elsevier 3rd edition (2005)

[29] Bevington , Data Reduction and Error Analysis for the Physical Science, McGraw Hill, 3rd Edition

[30] C.P. Lund et.al., Physical Review B 49,11352 (1994)

[31] D.E Ramaker, Journel of Vacuum Science Technology A Vacuum, Surface and films 7, 1614 (1989)

[32] D.E. Ramaker et al, Journal of Electrons spectroscopy and related phenomenon, 17, 45-65, (1979)

[33] D.E. Ramaker, The Past, Present and Future of Auger Lineshape Analysis, Critical Review in Solid State and Material Science, Technical Report 55, Office of Naval Research.

[34] H Enrenreich and H Philipp, Optical Properties of Ag and Cu, Physical Review volume 128, Number 4, (1962)

[35] Werner et.al, Applied Physics Letters 99, 184102 (2011)

[36] Peter Feibelman, Surface Science 282 129-136 (1993)

[37] Werner et. al, Surface Science 601 L109-L113, (2007)

[38] Werner et.al., Physical Review B 78, 233403 (2008)

[39] M S Chung and T E Everhart, Physical Rev B15, 4699 (1977)

[40] S Tougaard, Review Paper Surface and Interface Analysis., Vol 11, 453-472 (1988)

[41] S Tougaard and P Sigmund Physical Review B vol 25, Number 7 (1982)

[42] S Tougaard and C Jansson, Surface and Interface Analysis Vol 19, 171-174 (1992)

[43] Werner et.al., Surface Science Letters 518 L569-L576 (2002)

[44] W.S.M Werner, Journal of Surface Analysis, Vol 12 No2 (2005)

[45] Briggs and Grant, Surface Analysis by Auger and X Ray Photoelectron spectroscopy, Surface spectra, IM Publications

[46] QUASES- simple backgrounds, http://www.quases.com/products/quases-simple-backgrounds/

[47] QUASES User guide, http://www.quases.com/data/documents/QUASES Tougaard=20Ver5=20Manual.pdf

[48] S Tougaard and I Chorkendorff, Physical Review B Volume 35, Number 13 (1987)

[49] L Fieldman and J Mayer, Fundamental of Surface and This Film Analysis

[50] S. Tanuma, C. J. Powell, D. R. Penn: Surf. Interf. Anal.,Vol. 21, 165 (1993)

[51] Lin and Joy, Surface and Interface Analysis, 37, 895-900, (2005)

[52] E Sikafus, Physical Review B, vol 16, No.4 (1977)

[53] Bruining, Secondary electron emission, Wave series (1954)

[54] E Jung, PhD Dissertation, UTA (1996)

[55] H Zhou, PhD Dissertation, UTA (1996)

[56] S Xie PhD Dissertation, UTA (2003)

[57] Manori PhD Dissertation, UTA (2007)

[58] SIMION 8.0 Manual

[59] Chun Lei et. al., Review of Scientific Instrument 60(12), (1989)

[60] N Jiang, MS Thesis, UTA (1999)

Biographical Information

Prasad Joglekar did his undergraduate degree in Physics (B.Sc.) from the University of Mumbai in 2000. He continued his further studies at the same university and earned his Masters of Science (M.Sc.) in Physics degree in 2002 with specialization in electrons. After his master's degree he worked as a Technical Assistant at the Indian Institute of Technology Bombay, at Mumbai, India. His work at IITB developed his interest in condensed matter physics experimental work. At IITB he was involved in teaching Physics lab and worked in micro fabrication facility with hot wire chemical vapor deposition. At IITB, his work at Sophisticated Analytical Instrument Facility brought him toward the field of material characterization. He was extensively involved in sample preparation and analysis of materials using spectroscopy and electron microscopy (ICP AES, XRD, Raman, FTIR, UVVIS spectrometer, Scanning Electron microscopy and Transmission Electron microscopy. Prasad joined the Department of Physics at UTA in pursuit of higher (graduate) studies in 2008. He wishes to continue his work in the field of research and education. His research interest includes understanding different material characterization tool and techniques and development of novel materials, thin film for application in energy conversion along with its electronic and surface property studies.